# UNIVERSITY OF NAPLES FEDERICO II
# UNIVERSITY OF BERGAMO

Ph.D. Program in

**Technology, Innovation and Management (TIM)**

XXXV Cycle

*SSD: ING-IND/05 Aerospace Equipments and Systems*

# ***Innovative Systems and Solutions for Unmanned Traffic Management***

*Ph.D. Advisors*

Prof. Domenico Accardo

Prof. Giancarlo Rufino

*Ph.D. Candidate*

Eng. Claudia Conte

ID: 1067616

*Ph.D. Course Coordinator*

Prof. Renato Redondi

*Blank Page*

# Abstract

The rapid increase of the Unmanned Aerial System market needed the definition of a regulated airspace that guarantees high accuracy and integrity levels, also considering the economic and social impact of unmanned platforms in the civil airspace. This study presents the development of innovative systems and solutions to support the so-called Unmanned Traffic Management. A modular system configuration called BRAINS was defined for an innovative integration of on-board units thanks to the identification of a core section and a custom section in a multi-platform and multi-mission scenario. The defined core section includes the processing units to be installed on-board a generic platform. The custom section includes the units that are specific for platform and mission. The units that are involved by the Unmanned Traffic Management services were analyzed and innovative solutions were implemented and tested thanks to on-ground and in-flight tests. Specifically, a Deep Learning based method for Trajectory Prediction was developed to predict the Unmanned Aerial System time-of-flight and battery discharge during a generic path. A technique to estimate the battery capacity was reported to predict the battery State Of Charge. An innovative method for heading angle estimation based on a polarimetric camera was developed for airspace where the satellite-based navigation is challenging. Moreover, advanced techniques for payload data processing were implemented analyzing Unmanned Aerial System swarming capabilities also as support to emergency situations. The definition and development of tests by using both custom and commercial Unmanned Aerial Systems allowed to implement standard solutions and procedures that can be applied to support the Unmanned Traffic Management.

**Keywords**: Mission Management System, Unmanned Aerial Systems, Unmanned Traffic Management

# Contents

# List of Figures

# List of Tables

# List of Equations

# 1. Introduction

The latest years experienced a worldwide growth of air traffic that includes both manned and unmanned aircraft. New rules, procedures, and systems are required to support the challenging integration of Unmanned Aerial Systems (UASs) in the civil airspace. Beside the already assessed solutions developed for the Air Traffic Management (ATM), specific services must be identified and implemented to guarantee safe missions in the so-called Unmanned Aerial System Traffic Management (UTM) that includes low-altitude UAS operations.

The recent increase of UAS user demand is related to the wide diffusion of different types of mission that can be achieved reducing time and costs, as well as human risks. According to the European Drones Outlook Study [1] the sectors that will be mainly affected by the UAS introduction are agriculture, public security, transport, and energy. Fields and crops can be easily covered by using UASs with Electro Optical (EO) and Infrared (IR) payload systems to monitor the vegetation and terrain health state and act tempestive actions. Border patrolling and surveillance can be performed in less time and proving accurate data also in coordination with ground operations. Unmanned aerial taxi can provide rapid passenger transport links in the so-called Urban Air Mobility (UAM) scenario. Package delivery missions can support same-day distributions in the e-commerce development. Emergency deliveries, such as biological samples and medicines, can benefit from rapid transport. In the Industry 4.0 framework, UASs can provide critical services, such as predictive maintenance, photogrammetry, infrastructure inspections, to support more efficient industrial operations and reducing the risk level for workers.

The introduction of UAS technology must come with an equally rapid adaption of rules and procedures. The UAS regulation is undergoing several updates during the latest years in many countries. For example, the European Aviation Union Safety Agency (EASA) in Europe [2] and the Federal Aviation Administration (FAA) in the United States [3] are adapting the UAS regulation to face the rapid market changing. The core of the new regulation scenario is related to the risk evaluation that currently is performed considering the mission operative conditions other than the UAS specifications.

The need to realize a safe and efficient UTM has led to the development of advanced solutions for on-board and on-ground systems that will enable the integration of UASs with different specifications for several mission types. Planning, Conflict Detection & Resolution, and Contingency Management are some of the main topics that the research field is investigating to provide innovative solutions for the UTM development.

This work presents the design of a modular task-oriented Mission Management System called BRAINS that allows an easy integration of on-board units. The main modules that interface with the UTM functions were identified. Innovative systems and solutions were developed to support UAS integration in civil airspace according to UTM requirements. Adequate test strategies were implemented to validate the achieved results thanks to on-ground and in-flight tests by using custom and commercial UASs. The development of the proposed methods was supported by the adoption of low-cost and high-performance embedded Micro-Electro-Mechanical-Systems (MEMS) that allow to implement compact and lightweight solutions in the UAS multi-platform and multi-mission scenario.

A schematic description of the presented work is shown in Fig. 1. Chapter 1 includes an introduction about the role of UASs in the current airspace scenario that is crowded by manned and unmanned vehicles with different specifications. The main features of unmanned traffic were analyzed as starting point to define accurate and efficient solutions in agreement with UTM requirements. Chapter 2 highlights the economic and social impact of UAS technology in the today market and the effect of the UTM services introduction. Chapter 3 introduces the modular Mission Management System called BRAINS that proposes a task-oriented approach of on-board system integrations to satisfy UTM requirements. Chapter 4 describes a Deep Learning (DL) based method for Trajectory Prediction (TP) that can be adopted in strategical phase for flight planning and in tactical phase for re-planning evaluations of many UASs. Specifically, the UAS time-of-flight and battery discharge were predicted thanks to a data-driven approach considering the nominal path and the wind vector as input values. Chapter 5 reports an innovative integration of a polarimetric camera that allows to accurate estimate the heading angle in environments where traditional navigation solutions are challenging. Chapter 6 analyzes UAS swarming capabilities that must be considered to develop adequate configurations. The identification of core enabling technologies for different swarms allows to analyze the configurations that the UTM must face. Two case-studies were evaluated: the first case-study involves a UAS swarm that can monitor wide areas in emergency conditions, such as during COVID-19 pandemic; the second case-study involves a UAS swarm that electromagnetically obscure a ground-based radar for military applications. Chapter 7 includes the conclusion of the presented work with a summary of the obtained results.

The proposed work aims at developing innovative systems and solutions to support the definition of standard procedures in the ongoing UTM requirements assessment for a safe integration of UAS in the civil airspace.

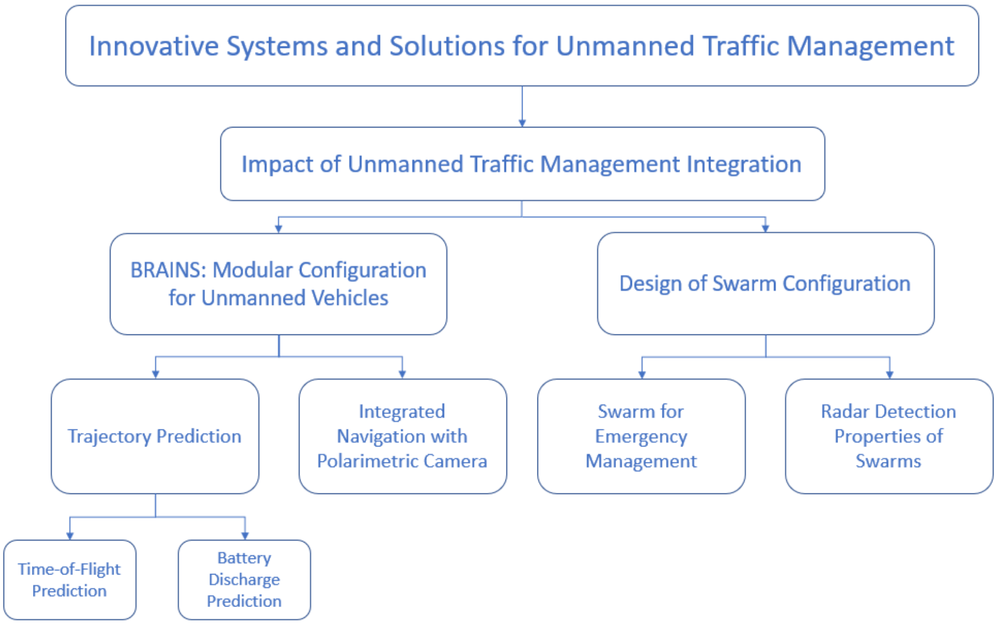

Fig. 1. Flow-chart of activities presented in this thesis work.

## 1.1. Unmanned Aerial Systems Overview

In the last few years, the UAS market has had a rapid growth and, nowadays, it includes several systems with different size, weight and payload systems that are developed according to the planned mission. The period from 2001 until today has been defined as the “UAS Golden Era” [4], thanks to the system technological improvement, such as satellite communications, navigation systems, advanced payload systems. The widespread development of UAS market is related to the design and development of versatile platforms that can achieve high performance for navigation and mission purposes in different environments.

According to the International Civil Aviation Organization (ICAO), the term Unmanned Aircraft System [5] is referred to a macro-set of vehicles that does not have a human on-board operator, so it includes both autonomous and remotely piloted vehicles. The advantages related to the adoption of UASs include the time and cost reduction of mission development and the possibility to cover large areas. Also, the use of UASs is strongly related to the reduction of the effort and/or risk of the human operator for the so-called Dull, Dirty, and Dangerous operations [4]:

- Dull operations involve repetitive activities, such as surveillance, communication relay, and terrain mapping.
- Dirty operations involve activities in contaminated areas with high levels of radiations and chemical agents.
- Dangerous operations involve activities in high-risk areas that are affected by environmental disasters or military missions.

Usually, the UAS concept includes the aerial segment, the ground segment, and the communication link [5]. The aerial segment involves the Unmanned Aerial Vehicle (UAV) and the on-board sensors, the ground segment involves the ground station to control the vehicle and monitor the flight parameters, and the communication link allows to exchange the downlink data related to the vehicle status and the uplink data related to the operator commands. Most of current applications involve the use of autonomous or automatic UASs. Autonomous UASs does not need human actions against flight plan perturbations, instead automatic UASs follow a planned flight plan, but the pilot must intervene if unexpected events occur. The design of the flight control system is a critical element because it must guarantee the management of planned flight plans and a proper payload control. Moreover, innovative sensor data processing can be exploited to improve both primary tasks, such as navigation, collision avoidance, contingency management, and payload operations. Exchangeable payload configurations and lightweight frames can be used to achieve compact platforms and improve the mission results.

## 1.2. Unmanned Aerial Systems Regulation

The growth of UAS market determined the need to develop a safe regulated environment where different types of platforms must be integrated with the traditional manned aviation. The EASA developed common rules to realize a harmonized set of regulations in all member countries. Each member country has a transition period in which it must be complied with the issued rules in terms of certification procedures, designing, manufacturing, licenses.

During the year 2019, the European regulation for UASs experienced a turning point with the introduction of Regulation (EU) 2019/945 [6] and Regulation (EU) 2019/947 [7]. The new documentation considers the whole UAS operation as classification criteria. So, the UAS operations can be classified in three categories:

1) *Open category*. An authorization by the proper authority is not needed before the UAS operation.
2) *Specific category*. An authorization by the proper authority is needed before the UAS operation.
3) *Certified category*. A proper certification is requested for UAS, remote pilot, and operator to conduct the operation.

The *open category* [8] provides guidelines for operations that includes UASs with a Maximum Take of Mass (MTOM) lower than 25kg and no flights over uninvolved people. According to MTOM, systems, and specifications, UASs in the *open category* are classified by using identification labels from C0 to C4. This category includes three sub-categories:

1) A1 sub-category. The sub-category includes operations with UASs characterized by a MTOM lower than 250g with lighter requirements for the pilot, and UASs characterized by a MTOM larger than 250g and lower than 500g with training requirements for the pilot. The UAS registration is mandatory if the UAS MTOM is larger than 250g and lower than 500g or if the UAS MTOM is lower than 250g, it is equipped with a camera and it is not considered a toy.
2) A2 sub-category. The sub-category includes operations with UASs characterized by a MTOM lower than 2kg with specific training for the pilot. The limit is 4kg

for UASs that belong to C2 class. The operation must be conducted at a distance larger than 50m from uninvolved people.

3) A3 sub-category. The sub-category includes operations with UASs characterized by a MTOM lower than 25kg with specific training for the pilot. The operation must be conducted at a distance larger than 150m from commercial and residential places.

The limitation of MTOM at 500g is a temporary issue that will be increase to 900g.

The *specific category* [9] provides guidelines for operations that must be approved before the mission start. An exception to the authorization is for UASs that are defined by the identification label C5 or C6 and operations that can be included in the so-called *standard scenarios* ST1 and ST2. For this type of operations, the UAS operator must send a declaration -not an authorization request- to the proper authority before the mission start. Otherwise, the UAS operator must conduct:

1) A risk assessment. This procedure must be provided performing a risk analysis for the involved operations according to specific guidelines, such as the Specific Operations Risk Assessment (SORA) approach.
2) A predefined risk assessment. Mitigations and particularities allow to simplify the authorization request according to specific characteristics.

Moreover, organizations that are in compliant with specific requirements can obtain the Light UAS operator certificate (LUC). Thanks to this certificate the organization can self-authorize operations in the *specific category*.

The *certified category* [10] involves operation with the highest risk. The UAS must be certified, as it happens for manned aviation with airworthiness and type certificates. Moreover, certificates are also needed by the UAS remote pilot and operator to conduct the mission according to high-standard safety levels. The first operations that will be investigated in this category are:

1) Type 1. Cargo UAS operations in A-C class airspace conducted in Instrumental Flight Rule (IFR).
2) Type 2. UAM or package delivery operations.
3) Type 3. UAS operations with a human on-board pilot.

### 1.3. Unmanned Traffic Management Overview

The increase of UAS demand is also driving the development of a regulated airspace volume to integrate UASs in the Very-Low-Level (VLL) airspace. The concept of UTM aims at managing the traffic of unmanned aircraft in the civil airspace guaranteeing a high safety level for people and building on-ground and manned aircraft in the surrounding airspace volume. Tasks such as identification, tracking, monitoring, emergency management, conflict resolution must be implemented providing proper services [11]. The realization of harmonized solutions for UAS integration involves a great worldwide effort by aviation authority. Examples of UTM implementation are shortly reported for Europe and United States cases.

The EASA supported several proposals aimed at developing a single airspace with common rules. The Single European Sky ATM Research (SESAR) Joint Undertaking [12] is an organization among private and public entities to support the development of a harmonized airspace among the member countries. It was born thanks to the cooperation between the European Union and Eurocontrol that is the European organization for supporting Air Traffic Management and Control. The effort to develop common rules does not include only manned aircraft. The rapid growth of the unmanned systems market introduced platforms with different specifications in the civil airspace.

To face up the recent needs of UTM, the European solution called U-space [13] was developed to implement the airspace services of UASs. Several projects were funded to support the identification and implementation of U-space services. Each project was focused on specific tasks and systems that the UTM should develop to properly manage a high number of platforms in different conditions supporting the introduction of new features, such as Beyond Visual Line Of Sight (BVLOS) operations and the swarming capabilities. An overview of some European projects is reported in Table 1 underling the main goals of each work.

Table 1. Main projects about U-space implementation.

| **Project** | **Starting Date** | **Goals** |
|---|---|---|
| CORUS [14] | 01/09/2017 | Development of initial Concept of Operations for U-space. Definition of four incremental steps (U1-U4) for U-space services implementation. |
| AIRPASS [15] | 01/11/2017 | Identification of UAS on-board systems according to UAS performance and U-space services. |
| GEOSAFE [16] | 24/07/2018 | Definition of geofencing solutions to protect sensible areas. |
| EuroDRONE [17] | 01/10/2018 | Development of a cloud-based solution and innovative communications for UTM. |
| DACUS [18] | 01/07/2020 | Demand and capacity balancing guaranteeing adequate safety level and separation. |
| Metropolis 2 [19] | 01/11/2020 | Solutions for strategic and tactical deconfliction and dynamic capacity management. |
| CORUS XUAM [20] | 01/12/2020 | Development of services for UAM operations. |
| AMU-LED [21] | 01/01/2021 | Development of Concept of Operations for UAM operations. |
| USEPE [22] | 01/01/2021 | Solutions for separation and deconfliction in high-demand scenarios. |

The European Commission issued the Regulation (EU) 2021/664 [23] about “A regulatory framework for the U-space”. This set of rules is applicable to all UASs, UAS operators, and service providers except for operations that involve UAS with a MTOM lower than 250g or UASs that belong to C0 class. In the document the mandatory U-space services are reported, such as identification, geo-awareness, flight authorization, traffic and weather information, conformance monitoring, as summarized in Fig. 2.

- Network identification. Critical data must be shared during the mission. The UAS operator must be identified by a unique registration number, as well as the UAS vehicle. Data about UAS position, course angle, remote pilot position must also be available.
- Geo-awareness. Airspace constrains, specific limitations and constrictions must be identified and communicated.
- Flight authorization. The UAS flight plans must be managed and authorized checking for collisions. A first-come first-served policy is applied. The UAS operator must receive a notification about the authorization response.
- Traffic information. Data about nearby traffic must be shared. It includes both manned and unmanned operations.
- Weather information. Data about wind, visibility, ceiling, temperature, and pressure must be collected to manage UAS operations.
- Conformance monitoring. If an authorized flight is not compliant with the planned mission, the UAS operator must receive a notification, as well as the UAS operators that are in the same area.

The airspace risk assessment must be evaluated in all conditions based on UAS performance and available services. UAS operators must know in each airspace sector which are the available services that are provided. The forecast of U-space services development involves a four-step-based implementation from U1 to U4 [24] that will support a full deployment starting from 2030.

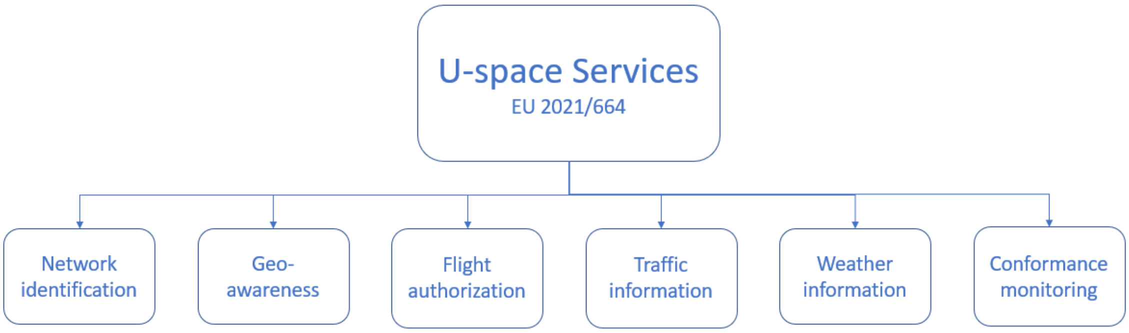

Fig. 2. Mandatory U-space services according to Regulation (EU) 2021/664.

FAA planned the Next Generation Air Transportation System (NextGen) program [25] to develop innovative improvements to the United States airspace system. The introduction of UASs in national airspace drove the development of the UTM Research Transition Team (RTT) with NASA and industrial partners in 2016. The UTM Pilot Program [26] was defined to manage the small UASs operations and detect the services needed to support the unmanned traffic. Initially, some tasks were identified, such as sharing data about the mission intent among the UAS operators, remote identification, situational awareness. So, the program developed a proof of concept for UTM system also aimed at improving the Flight Information Management System.

The Integration Pilot Program [27] was developed to face up the challenge related to the UAS integration in national airspace promoting a harmonization strategy with local entities and authorities. The BEYOND program [28] was planned to continue the effort performed during the Integration Pilot Program focusing on Beyond Visual Line Of Sight (BVLOS) operations and designing standard procedure to allow a safe UAS integration.

The UTM Concept of Operations v2 [29] was developed in order to provide the main guidelines for UAS operations in different airspace classes. The main services that must be provided to UASs are reported and a layered approach related to safety, security, and equity concepts was developed to manage the access to the airspace. Some operational scenarios are described considering different airspace classes and the interaction between manned and unmanned traffic.

# 2. Impact of Unmanned Traffic Integration

The development of advanced core enabling technologies for unmanned vehicles allowed an increase of market demand involving different platforms and missions. The large use of UASs in civil sectors allows to reduce the operating mission time and the use of low-cost MEMS supports a competitive cost strategy. So, the introduction of UAS is experiencing a strong impact on everyday life.

According to [1], considering a time horizon up to the year 2050, the European interest related to the UAS operations will be mainly focused on the following fields: agriculture, public safety, energy, delivery, transport. In the scenario of Industry 4.0, the adoption of innovative UAS technologies allows to support critical tasks, such as predictive maintenance, infrastructure inspection, and 3D reconstruction.

The condition of a more and more crowded airspace and the ongoing development of UTM systems and solutions are carrying a strong impact on both economic and social context.

In the United States according to the FAA Aerospace Forecast Fiscal Years 2021-2041 [30] the UAS market will include about 1.55 million units for recreation/Model fleet and about 0.83 million units for commercial/non-model fleet in 2025. In Europe according to [1] the UAS market will include about 7.00 million units for recreation operations and 0.20 million units for commercial purposes in 2025. So, the introduction of UTM in civil airspace will improve economic growth, connectivity, creation of jobs, development of safer procedures. However, it requires a huge effort to adapt already available systems to the new UTM concept.

Social acceptance is also a critical element that must be taken into account during the definition of UTM guidelines. For example, UAS swarms can be used to support monitoring operations or police patrol operations in urban environment. Future applications, such as UAM or package delivery operations will involve UAS with a MTOM larger than 25kg as intra-city or extra-city transport vehicles. Several studies are focusing on the determination of the main factors that affect the public opinion about UAS operations. According to [31] the main factors of social acceptance for UAM operations are:

- Noise
- Safety
- Privacy

Requirements related to the mentioned factors must be analyzed during the design phase of UAS and UAS missions. Then, in tactical phase, the UAS operator must reduce the impact of these factors on uninvolved people, i.e. people that have not been informed about the UAS operation.

The modular configuration that is described in Chapter 3 was designed to achieve interoperability capability in multi-platform and multi-mission operations exploiting already available systems that can be re-arranged according to the operation type to match the UTM requirements. Low-cost MEMS are preferred to develop compact systems with reduced cost. Moreover, the mass-production of standard systems allows to achieve more reliable devices.

# 3. BRAINS: Modular Configuration for Unmanned Vehicles

The design and test of vehicle onboard systems must be performed according to the user demand and current regulation in order to guarantee a proper safety level. However, the context of unmanned vehicles is characterized by a multi-platform and multi-mission scenario, in which each platform can execute several missions with different operative conditions. This context increases the number of custom on-board systems. The aim of the proposed work is the development of an innovative task-oriented Mission Management System called BRAINS that includes a modular configuration to better face the new requirements of UTM scenario.

## 3.1. Overview

According to the traditional integration of on-board systems, each element of the system configuration should perform a specific function. This element must be customized for a specific vehicle including both the processing units and the sensing units. However, the traditional approach has a difficult system integration for the multi-platform and multi-mission context because if a new platform is designed or if the same platform must perform a different mission, the whole system must be changed. So, if the onboard system configuration is based on applicative functions, the development of standard modules for different unmanned vehicles is still a challenge.

The lack of standard modular systems involves the lack of standard procedures for systems development. So, the standardization of core enabling Guidance, Navigation and Control (GN&C) technologies is becoming a critical requirement that has not yet been fully realized. The development of modular systems involves the use and the integration of assessed technologies [32] [33] [34]. Moreover, there is a great interest in the use of embedded systems for modular configurations and open systems for aerial, terrestrial, and maritime applications [35] [36] [37].

A modular configuration can be defined thanks to standard processing modules that interface with sensing elements, such as sensors and actuators. The communication can be realized thanks to a specific data bus protocol. The proposed modular system is called BRAINS because this task-oriented Mission Management System is a bio-inspired modular configuration similar to human brain. It was designed to be installed onboard a generic autonomous vehicle including processing units in the *core section* and custom units in the *custom section*. The units must be identified avoiding unused or duplicate systems.

The proposed task-oriented Mission Management System aims at developing an advanced on-board system integration for unmanned platform as it happened in traditional aviation considering the Lockheed Martin F-35® and Northrop Grumman B-21® experience. As a result, the human intervention can be destinated to high level operations, such as manned-unmanned interaction and swarm coordination. The use of the proposed configuration can reduce the manufacturing cost because the core section can be mass-produced at a more competitive cost. Moreover, the adoption of MEMS must support the identification of compact and high-performance hardware devices. The so-called Commercial off-the-shelf (COTS) devices can be acquired to realize an easier system integration. This approach aims at increasing the reliability level and the development of standard procedure for safer missions.

### 3.2. BRAINS System Configuration

The presented modular configuration proposes a different approach with respect to the traditional configuration that involves a fully customized system. For example, the traditional configuration develops the Guidance, Navigation and Control (GN&C) functions with different custom systems.

This modular system is presented in [38] and it proposes a *core section* that involves the processing modules, and a *custom section* that includes the specific devices of the vehicle. The traditional functions, such as GN&C, can be reconstructed thanks to a proper combination of the units included in *core section* and *custom section*. The outputs of the defined units combination are called synthetic functions.

The units included in the *core section* must be selected considering the technologies that can be supported by a generic platform. At the beginning the systems that are in common among different autonomous systems must be identified. Then, a preliminary design analysis must be carried out to assess the feasibility of the integration in the main part of the onboard configuration. The units of the *core section* are selected based on the processing type. Instead, the *custom section* includes the peripheral units, such as sensors, actuators, and antennas that are custom elements for each transport system and/or mission type. The communication among the units is guaranteed by a standard data bus. Standard interface must be preferred to provide the link with the units of the *custom section*. Systems can be easily interchanged supporting maintenance and improvement operations.

BRAINS system configuration is showed in Fig. 3, where the processing units are at the center of the figure and the custom units are outside. Three data buses are reported, the first and second data buses are designed for Real-Time (RT) data at respectively low and high Data-Rate (DR), and they can provide communication links for primary tasks. The third data bus supports high DR considering a non-deterministic control and it is used to handle data from payload.

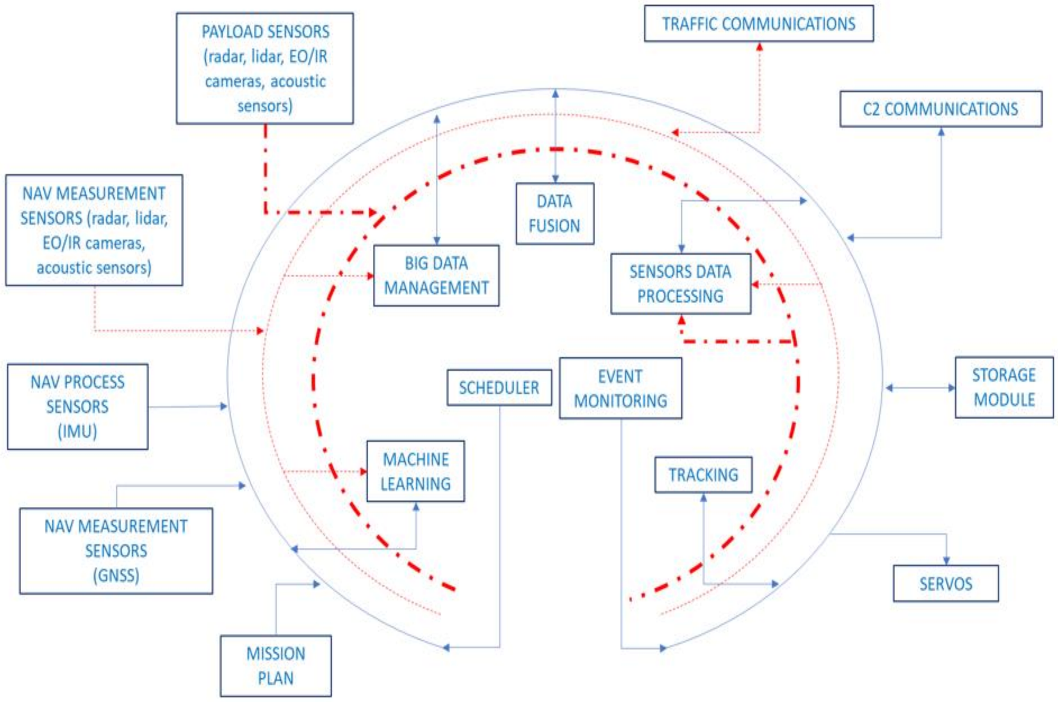

Fig. 3. BRAINS system configuration. Blu line indicates real-time low Data-Rate, red line indicates real-time high Data-Rate, bold red line indicates non real time high Data-Rate.

The units that are included in the *core section* are described below.

- The *Scheduler* unit is the most critical unit because it coordinates all the units that are included in the *core section*. In nominal condition, the Scheduler activates the other units. Thanks to the data-bus interface, it can also access the partially processed raw data coming from the *Sensors Data Processing* unit to properly implement decision-making algorithms for module activation. Considering the important task, the Scheduler functioning must be guaranteed in all conditions, so redundant configuration can be developed in case of a failure of the main unit, or a multiple layer configuration can be designed to isolate the effect of failures.
- The *Event Monitoring* unit detects failures in the system health status, and it is activated by the *Scheduler* in emergency conditions. This unit saves the system health status by using specific flags that are properly stored.
- The *Machine Learning* unit can be used for classification and prediction tasks. This module receives data about the external environment thanks to the *custom section* modules and allows to run learning algorithms that can be used for both primary and payload operations, such as detection of sensor failures, vehicle trajectory prediction, positioning, obstacle detection. The choice of the hardware component must be driven by the computational cost required for the selected learning algorithms.
- The *Big Data Management* unit can be used to improve the route scheduling task. This module elaborates data coming from traffic information sources and maps and allows to run algorithms to proper interpret and model the partially processed data from the *Sensors Data Processing* unit. It supports proper changes to the flight plan to select safe routes.
- The *Sensors Data Processing* unit receives data from custom units, such as payload and navigation sensors and outputs data for navigation purpose. All the incoming data must be properly elaborated by custom units in a standard format.
- The *Data Fusion* unit supports the integrated navigation task. An optimized solution must be developed considering specific filters, such as Kalman filter, extended Kalman filter, Particle filter to update the navigation state.
- The *Tracking* unit receives data coming from the own vehicle or vehicles in the surrounding area. For example, considering the collision avoidance task, this unit provides information related to fixed and moving obstacles.

The units that are included in the *custom section* are specific for each vehicle model. However, some categories are described below.

- The *Navigation Process Sensors* unit elaborates data coming from navigation sensors that require the information about the previous state, such as the Inertial Measurement Unit (IMU).
- The *Navigation Measurement Sensors* unit elaborates data coming from navigation sensor measurements that are related only to the current state. Some sensors require low data rate bus, such as Global Navigation Satellite System (GNSS) sensors. Other sensors require high data rate, such as radars, lidars, cameras, and acoustic sensors.
- The *Payload Sensors* unit involves all the sensors that are needed by the mission but not for the vehicle operations. Cameras, radars, lidars can be used and they require high data rate bus.
- The *Mission Plan* unit elaborates the planned waypoints to define the mission profile. Data related to traffic and maps information can be integrated to update the flight plan.
- The *Command-and-Control Communication Link* unit must be designed and selected according to the operational environment. Radio systems are used for air communications, as it happens for aerial and ground vehicles and maritime vehicles above the sea surface. Different solutions must be designed for underwater vehicles, such as sound waves or optical communications. For example, sonars can cover long distances, but they need high power, instead, LEDs and photodetectors can be used for short-range operations by using low power consumption.
- The *Traffic Communication* unit handles data collected by the vehicles in the surrounding environment. This unit allows to map the other vehicles avoiding moving obstacles.
- The *Servos* unit includes the low-level actuator control. Proper analysis must be performed to select the servo drives based on vehicle specifications.
- The *Storage* unit collects the data that are processed by the other units. Data are exchanged at low data rate because the stored outputs have been already synthetized.

Considering the described system configuration, the GN&C functions can be developed as synthetic functions, as reported in the next examples.

### 3.3. Example 1: Guidance Function

The traditional Guidance function defines the nominal path that the vehicle should execute. The route can be defined as a series of waypoints that include information about position and velocity. The system units that are used to develop this function have a white background and the system units that are not used have a light grey background in Fig. 4.

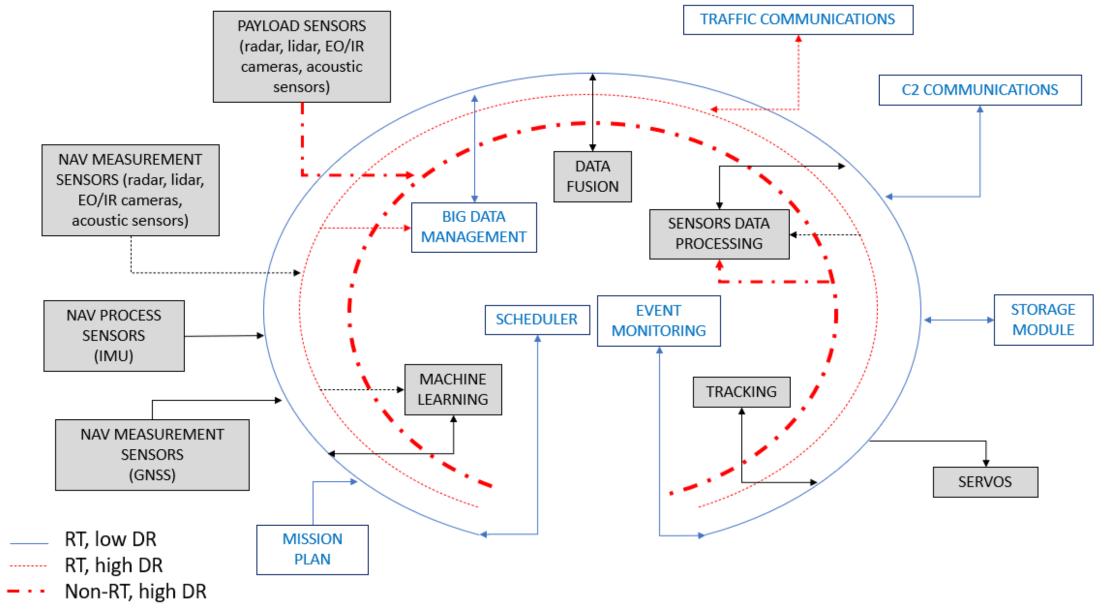

Fig. 4. System units involved in the Guidance function. The system units that are that are used to develop this function have a white background and the system units that are not used have a light grey background.

The development of the traditional Guidance function as synthetic function is reported in Fig. 5.

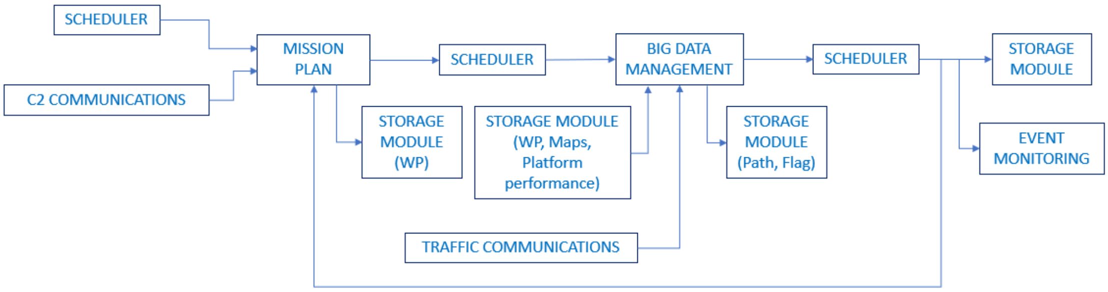

Fig. 5. Guidance function developed as synthetic function.

Before the mission start, the remote pilot of the unmanned vehicle activates the *Mission Plan* unit thanks to the *Command-and-Control Communication Link* unit. In this way, the flight plan is generated and uploaded. The remote pilot can also activate the *Mission Plan* unit during the tactical phase of the mission to update the nominal path. The *Mission Plan* unit can also be activated by the *Scheduler* unit if a system failure is detected.

The remote pilot usually assigns the initial and final waypoints or a number of intermediate 3D/4D waypoints. The *Mission Plan* unit receives the information about the planned pilot intentions and develops a sequence of waypoints that are collected by the *Storage* unit. Then, the *Big Data Management* unit is activated by the *Scheduler* unit to manage all the feasible paths that can be developed. Moreover, this unit compares the planned waypoints with external data to select the nominal route that best fit the requirements. The external data can be defined by maps, airspace regulation, vehicle specifications and routes of other vehicles.

The *Storage* unit save a flag related to the successful operation of path definition. The *Scheduler* unit updates the *Even Monitoring* unit about the path selection and the *Storage* unit saves the nominal path. Otherwise, the *Scheduler* iterates the path generation process changing the input parameters, such as allowing the remote pilot to modify the initial and final waypoint or delaying the mission start. The iterative process must be stopped if an assigned number of tentative is reached.

Applications related to Guidance function will be discussed in Chapter 4 about Trajectory Prediction.

### 3.4. Example 2: Navigation Function

The traditional Navigation function provides the real-time state of the vehicle and the deviations between the current path and the planned one. The system units that are used to develop this function have a white background and the system units that are not used have a light grey background in Fig. 6.

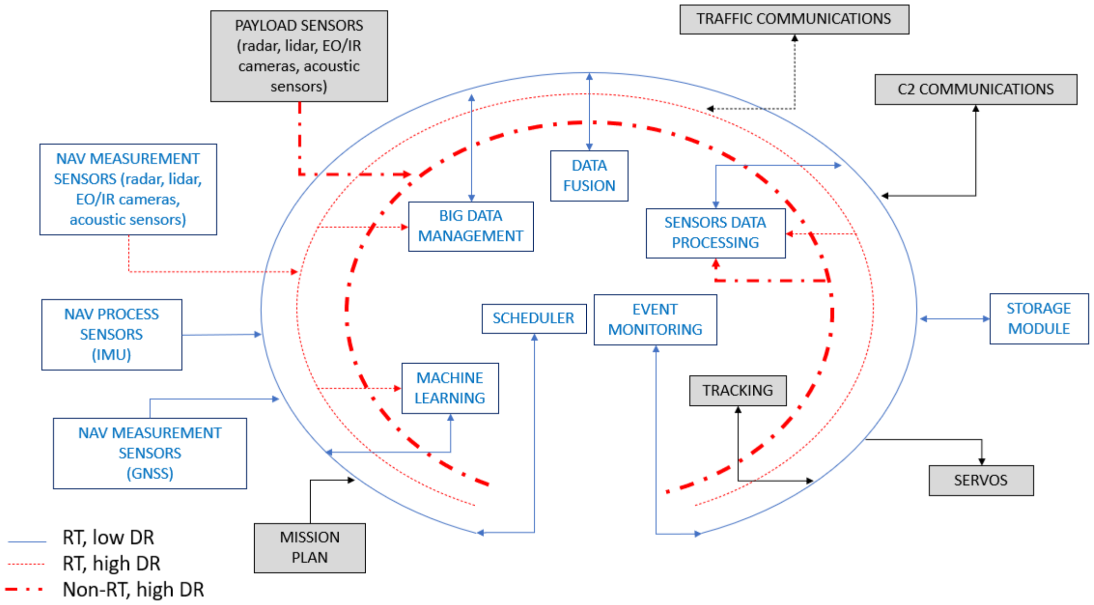

Fig. 6. System units involved in the Navigation function. The system units that are that are used to develop this function have a white background and the system units that are not used have a light grey background.

The development of the traditional Navigation function as synthetic function is reported in Fig. 7.

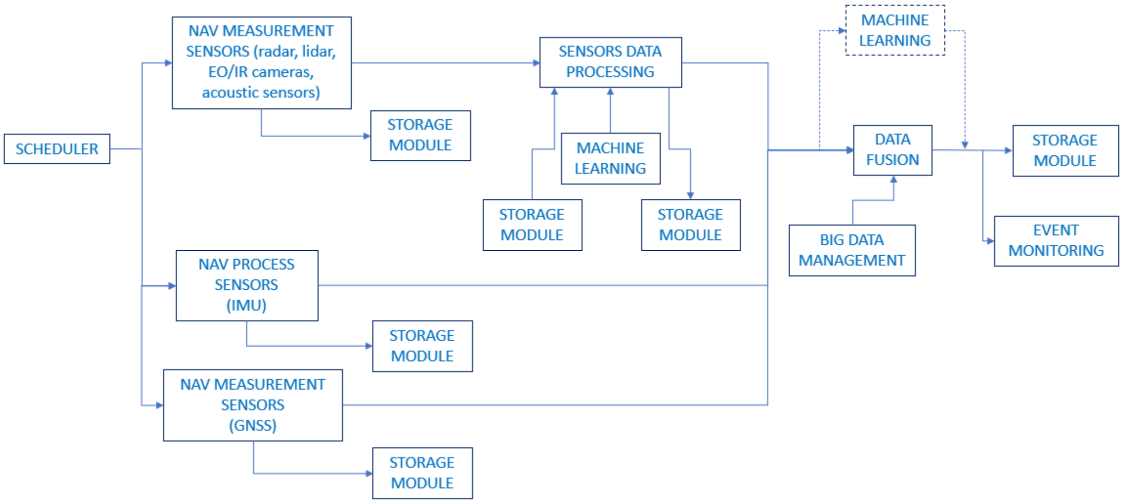

Fig. 7. Navigation function developed as synthetic function.

The *Scheduler* unit activates the *Navigation Sensors* to acquire data that are needed for navigation purpose. The measurements of cameras, radars, lidars, and acoustic sensors are synthetized by the *Sensor Data Processing* unit and then integrated with other data. The *Machine Learning* unit can be used to calibrate sensors. All synthetic data are stored in the *Storage* unit.

The *Data Fusion* unit processes data from the navigation sensors. This unit also integrates the output data of the *Big Data Management* unit to estimate the vehicle position and orientation. The *Machine Learning* unit can be eventually used for trajectory prediction solutions in order to better estimate the future vehicle trajectory.

The *Storage* unit saves the current vehicle state. The *Event Monitoring* unit evaluates the development of the navigation state estimation, and it activates the *Scheduler* unit if a system failure is detected.

Advanced applications related to Navigation function will be discussed in Paragraph 3.6 about some examples of hardware implementation and Chapter 5 about integration of a polarimetric camera.

### 3.5. Example 3: Control Function

The traditional Control function defines the actions to limit the estimated trajectory deviations with respect to the planned path. The control function also activates the servo drivers to send proper commands to the actuators. The system units that are used to develop this function have a white background and the system units that are not used have a light grey background in Fig. 8.

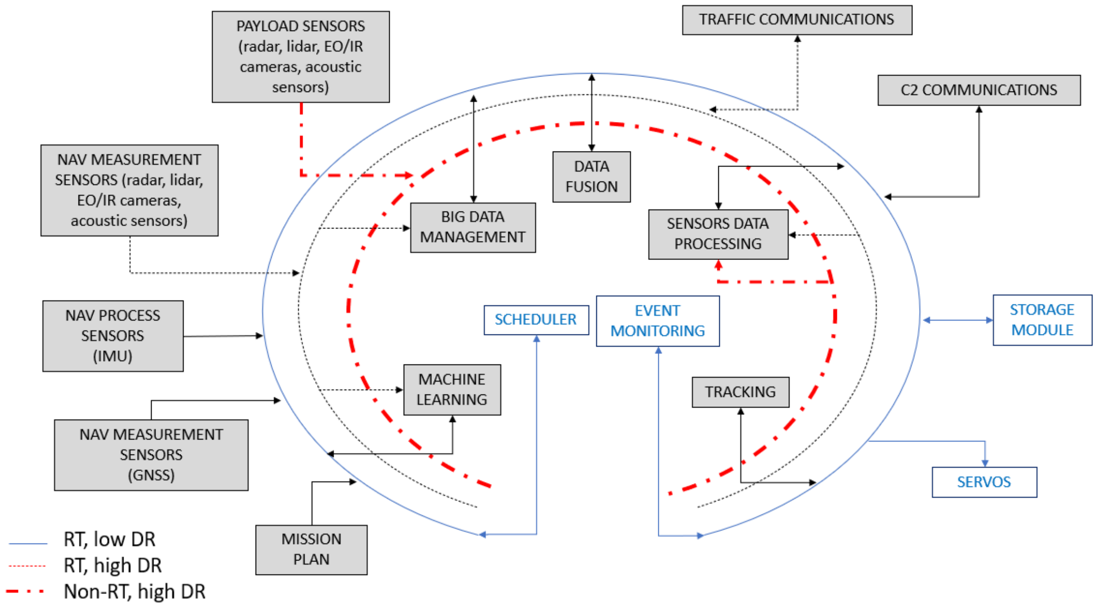

Fig. 8. System units involved in the Control function. The system units that are that are used to develop this function have a white background and the system units that are not used have a light grey background.

The development of the traditional Control function as synthetic function is reported in Fig. 9.

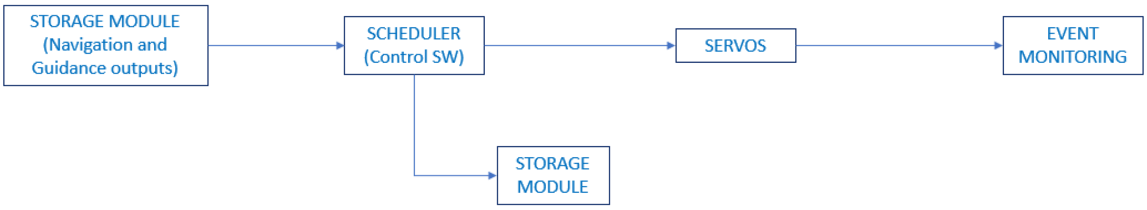

Fig. 9. Control function developed as synthetic function.

The output of the Guidance and Navigation synthetic functions are stored in the *Storage* unit. The *Scheduler* unit runs the control software that generates proper actions for the

*Servos* unit. The servos drivers generate feedback that is evaluated by the *Event Monitoring* unit that creates a flag about the system state.

Applications of Control function will be discussed in Chapter 6 about UAS swarming capabilities.

### 3.6. Hardware Test Examples

To develop a competitive cost strategy, high-performance boards can be exploited as processing units in the *core section*, such as BeagleBone® Blue, Raspberry Pi®, STM Nucleo® boards [39] [40] [41], limiting the cost to few hundreds of Euros. An example of processing units for UAS modular configuration that were analyzed is reported in Fig. 11 and a detailed view of the used boards is shown in Fig. 11. The integration of high-performance units allows to easily integrate a so-called *companion computer* that can be used to communicate with the main board, that performs the *Scheduler* unit functions, developing advanced tasks of other processing units, such as *Data Fusion*, *Sensor Data Processing*, *Machine Learning*, *Big Data Management*, and *Tracking*.

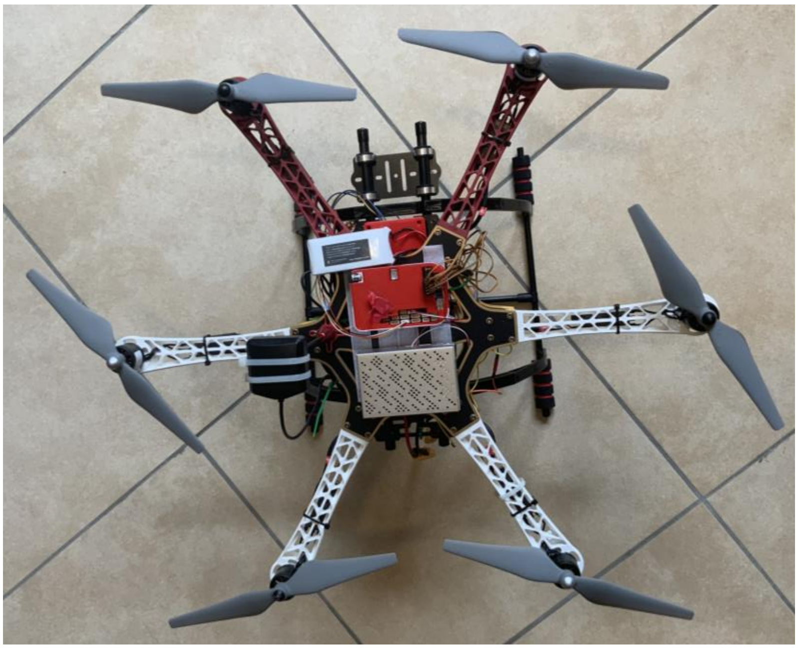

Fig. 10. Example of on-board processing units integration.

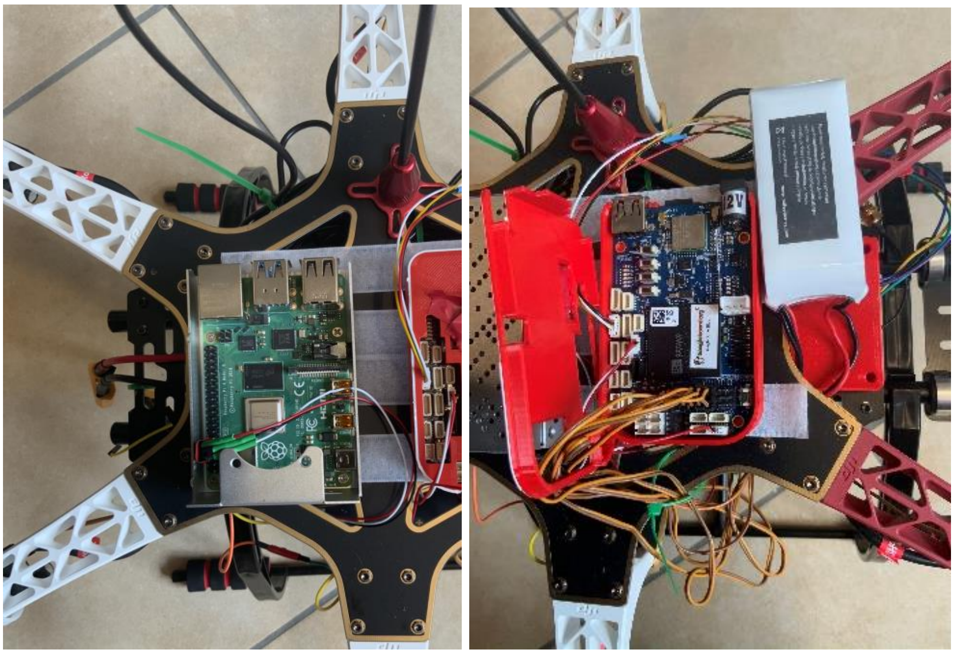
a) b)

Fig. 11. Details of used processing boards. a) Zoom on Raspberry Pi® 4 board. b) Zoom on BeagleBone® Blue board.

During the design and development of critical BRAINS units, hardware implementations were provided to develop compact and high-performance systems that can be used on-board the UAS *core section* for navigation purposes. A redundant configuration of low-cost inertial units was implemented to reduce the IMU bias, comparing the results with a high-performance tactical-grade sensor, as presented in [42]. The method proposed in [43] achieved a bias instability and random walk reduction of about 25% by using redundant geometry of MEMS inertial sensors. A procedure to estimate the initial heading of a vehicle by using a tactical-grade inertial sensor, a low-cost MEMS magnetometer, and a certified inertial unit as reference is reported in [44]. A Machine-Learning based method to detect failures in the air data system thanks to the integration with MEMS inertial units is reported in [45]. An embedded system is described in [46] that allows to manage the release of decoys from the UAS payload for veterinarian applications. At the end, to exploit the integration of MEMS inertial sensors and Real Time Kinematic GPS for position monitoring of large infrastructures, the study described in [47] was developed.

The proposed examples show the high configurability of BRAINS solution that can be used by different unmanned systems also in maritime and ground environments, such as Autonomous Underwater Systems, Autonomous Surface Vessels, and Unmanned Ground Systems.

## 3.7. BRAINS Business Assessment

### 3.7.1. Market Analysis

The technological improvement in the field of unmanned systems and the development of new UAS applications are driving the increase of UAS user demand. The first UASs were involved in military operations [48]. Then, according to [49], the industry emergence determined the increase of new applications such as the use of UASs for leisure purpose while the technology emergence determined the shift from leisure applications to commercial applications thanks to the adoption of advanced navigation and payload systems. The actual scenario of UAS market is strongly segmented based on the intended use [50], and three categories can be defined according to the user goal: leisure, commercial, and military. Each category involves specific requirements for UAS design and cost strategy. According to [1] the European market will involve 200 million Euros investments in UAS research and development field, and the annual economic impact will be about 15 billion Euros in 2050, as reported in Fig. 12. The units increase will reach a constant growth in 2050:

- Leisure operations will be conducted by 7 million UASs.
- Commercial operations will be conducted by 415 thousand UASs.
- Military operations will be conducted by 3 thousand UASs.

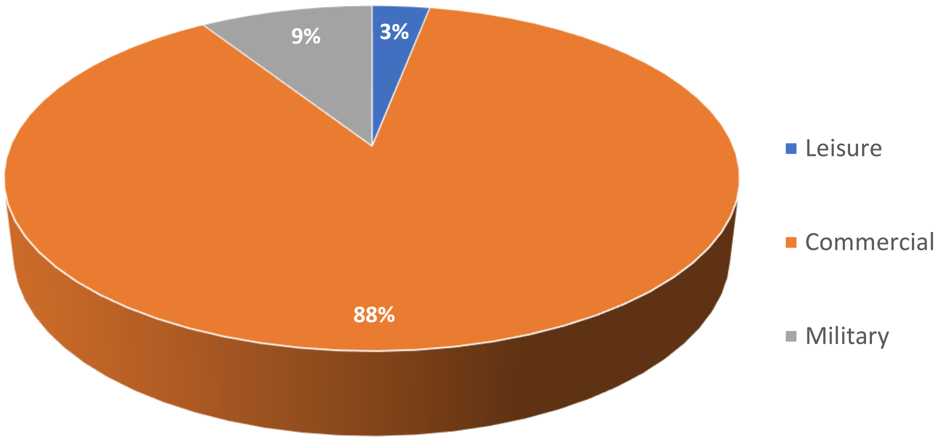

Fig. 12. Annual economic impact of UAS market of about 15 billion Euros in 2050.

The standardization of BRAINS *core section* can support the rapid increase and the segmentation of UAS market thanks to high configurability characteristics. The integration of low-cost embedded systems limits the cost of processing units adapting the proposed integrated system to different applications.

### 3.7.2. Product Added Value

BRAINS solution aims at exploiting a modular configuration to fit the rapid changes of UAS market and support the development of task-oriented integrated systems also in maritime and terrestrial environments. The mass-production of the *core section* for multiple platforms allows the reduction of the realization cost and an increase of the reliability level. A competitive cost strategy also exploits low-cost MEMS that are already available on the market. The certification procedure of the whole platform is supported by the certification of each module in different operative conditions. A task-oriented configuration allows an easier onboard system integration and unit exchange. The adoption of BRAINS solution can speed up maintenance operations, reducing the monitoring time and supporting planned predicted actions. Moreover, damaged units can be substituted without the need to replace the whole system. Shortcomings are related to the need of new validation tests to assess the integrated configuration, but an adequate test strategy can be planned and validated involving one-off costs.

### 3.7.3. Customers

Target customers for the proposed task-oriented solution are government and professional entities that operate in multi-mission scenarios. High resolution cameras, compact radars, advanced communication links can be included in BRAINS *custom section* to achieve specific missions exploiting the same *core section* with dedicated units. Also, military operations can be supported by BRAINS configuration thanks to the introduction of tactical grade sensors and advanced data processing to improve the navigation performance.

### 3.7.4. Competitors

Conventional UASs involve fully customized systems and represent a wide sector in all UAS market segments. Conventional UASs are "turnkey" solutions that can access the market to achieve specific mission profiles after the test and certification procedures of the whole system. Modular system configurations, on the other hand, must be compliant with high system integration requirements, but the certification procedure of each component can support the certification procedure of the whole system.

BRAINS solution exploits the advantages of modular configurations aiming at the development of a common *core section* to be installed on-board different types of platforms. The realization of a *custom section* represents an addiction to the whole effort of system implementation.

### 3.7.5. Providers

BRAINS configuration allows to optimize execution and achievement of several missions by exploiting the interoperability of different advanced methods and processing modules. High performance and low-cost processing units are widely available to limit costs [39] [40] [51]. However, for critical operations and/or military missions tactical grade sensors, for example [52], and advanced payload systems, such as [53], can be adopted.

### 3.7.6. Risk Analysis

Among the applications of UAS technology, the support to search and rescue operations, disaster monitoring, pandemic emergency represents an important element that characterizes the UAS market also in difficult conditions. However, the semiconductor shortage can have critical consequences. Many studies are investigating the problem developing solutions to optimizing the supply chain and developing shortage processes [54] [55] [56]. System robustness against external factors can be improved thanks to redundant configurations of main modules still avoiding unused peripheral units. The main elements evaluated during the risk analysis are shortly discussed in the Strengths, Weaknesses, Opportunities, and Threats (SWOT) diagram in Fig. 13.

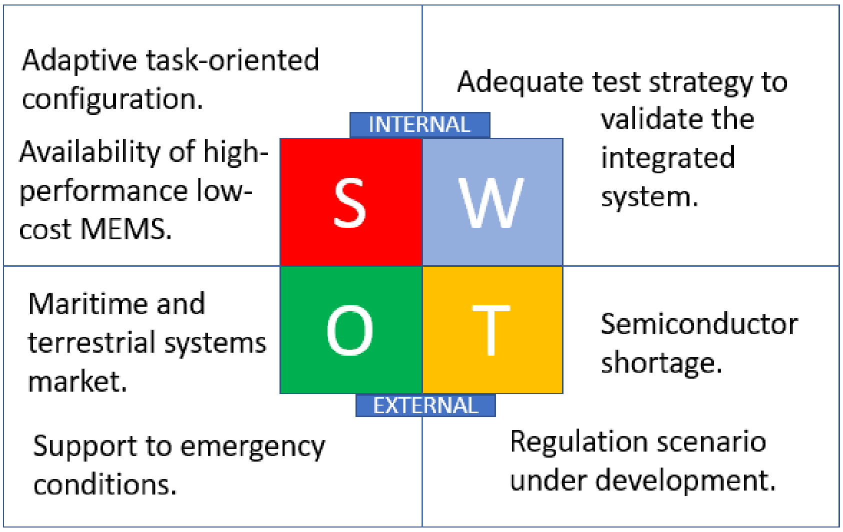

Fig. 13. SWOT analysis for BRAINS business assessment.

# 4. Trajectory Prediction of Unmanned Aerial Systems

The need to handle safe and reliable mission profiles drives the development of methods to predict the main mission parameters. TP methods can be exploited to support the pre-tactical phase of flight during the plan scheduling, or the tactical phase of flight during the operative trajectory. The method proposed in this study aims at predicting two critical parameters, i.e. the UAS time-of-flight and the UAS battery consumption. This approach can be adopted in the controller consoles, and it must be interfaced with the on-board *Traffic Communication* unit that handles other traffic data in the surrounding environment.

## 4.1. Overview

The prediction of future trajectories is a critical element in ATM development because it allows to act prompt actions to manage the traffic challenges. ATM requirements include a low computational cost and the analysis of non-linear data. Currently, Air Traffic Control (ATC) flight data processors adopt algorithms that are based on a straightforward model of aircraft dynamics, such as the Total Energy Model (TEM). The model of aircraft performance is included in a database named Base of Aircraft Data (BADA) [57] that collects data from aircraft manufacturers, ATC radar recordings, and ADS-B. However, TEM based methods does not take into account non-linear behavior and random uncertainties of the involves parameters.

Tools and procedures designed for ATM purposes aims at providing real-time predictions of several aircraft that are flying in the same airspace volume. Similarly, the recent introduction of unmanned vehicles in the civil airspace allowed to develop advanced TP methods for aeronautical applications, so that both ATM and UTM can benefit from this research topic [58] [59].

Several TP methods are based on physics parameters of the involved vehicle, such as model-based, probabilistic and Bayesian approaches [60] [61] [62] [63]. The development of accurate TP methods is related to the forecast of main vehicle parameters, such as position, autonomy, time-of-flight that must be assessed within a proper time interval thanks to advanced Flight Data Processors.

Data-driven approaches are used if simulated or real data are available, and they allow to standardize innovative approaches for traffic management [64] [65].

The use of ML will be helpful to support model-based method challenging. Indeed, thanks to data-driven approaches, learning algorithms can perform an optimal management of systems also considering uncertainties and non-linearities [66] [67] [68] [69] [70] [71] [72]. They can map transfer functions among many inputs that are not considered in model-based methods.

Specifically, TP methods based on learning algorithms for both unmanned and manned vehicles can be used to implement modular configurations, which have several advantages with respect to other methods. Proper planning strategies must be actuated according to the number and type of unmanned vehicles that populate the airspace. Learning based solutions allow to improve the prediction accuracy by adding new samples to the training database; Machine Learning (ML) and DL algorithms involve the possibility to add new features without the need to develop again the whole algorithm by changing the training dataset. The deterministic time needed to compute the output is important because the run-time is not related to the inputs. So, this type of algorithms can be used for real-time applications. Several databases are currently available to replicate the aircraft performance, such as BADA [57] for aircraft. Otherwise, a custom database can be collected. An advanced approach can involve a transfer learning based algorithms [73], [74] to reduce the computational time cost needed to generalize the investigated problem for a different platform starting from model-based simulations or a previously trained model. Moreover, several open-source libraries are available for training, validation and test learning algorithms, comparing different solutions, and training strategies to select the most performant approach.

Pre-processing phase is crucial for a proper algorithm configuration. A series of data sources shall be identified. Knowledge-based and stochastic evaluation of data must be performed to estimate the distribution of data and the amount of data required to train a network that gives adequate accuracy. A test strategy must be developed to evaluate the method performance thanks to non-learning-based benchmarks. Adaptive capabilities that are non-achievable for model-based approaches can be obtained by using learning-based algorithms because they do not need a fixed dynamical model.

TP procedures can be useful for additional applications [75] [76], such as prediction of Estimated Time of Arrival ETA, integration with Collaborative Decision Making (CDM) tools, and trajectory propagation for radar tracking. Moreover, this type of algorithms can also be tuned to support the needed integration of ATM and UTM.

## 4.2. Methodology

The proposed methodology is presented in [77]. A generic path includes segments between consecutive waypoints. During the performed tests the UAS reaches a planned waypoint, stops, and performs a heading change according to the next waypoint direction. This method adopts the waypoint approach to implement a safe procedure that can be standardized for UTM consoles. The pilot can monitor the surrounding airspace during the “stop” phase and, if an incoming vehicle is detected, proper evasive maneuvers can be performed. A corner is defined by two legs of assigned length, i.e. the segment before the turn and the segment after the turn. The time-of-flight along a generic path can be computed summing the corner time-of-flight and the remaining segments that are not included in a corner. Fig. 14 shows an example of generic path in which corners are delimited by red circles. Path planning applications often use strategies related to path segmentation.

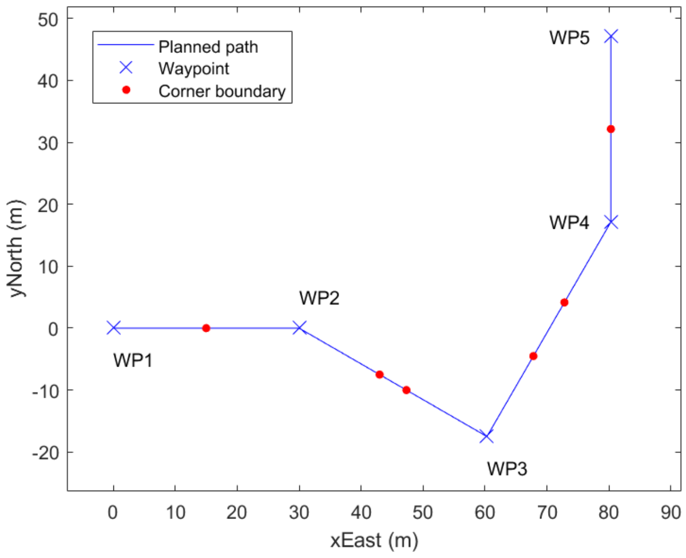

Fig. 14. Generic path with corner segmentation.

A zoom over a generic corner is reported in Fig. 15, where $S_i$ is the corner initial point and $F_i$ is the corner final point. The nominal length of each corner leg is $l$.

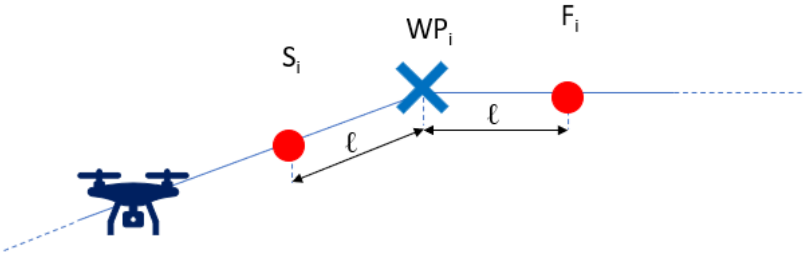

Fig. 15. Details of a standard corner.

Several commercial UASs were evaluated in order to select a model that can be used for typical missions, such as photogrammetry, inspections, and leisure. The DJI Mavic 2 Enterprise® [78] that is showed in Fig. 16 was selected.

Fig. 16. UAS model used for flight tests.

The Ground Station Software UgCS® [79] was used to upload the flight plan and monitor the mission execution. Each flight plan includes the assigned 3D waypoints with Latitude, Longitude and Above Ground Level Height coordinates. The missions were executed in automatic mode.

The tests were performed with a ground speed limit of 5m/s that is a common speed limit for several applications according to the Regulation (EU) 2020/639 [80] for the standard scenario STS-01 about "VLOS over a controlled area in an urban populated environment”. The application of a standard methodology that can be developed in accordance with standard scenarios and used for different UASs and missions, such as package delivery, surveillance, mapping, can support the introduction of the proposed approach in UTM consoles. The seven standard paths were flown at a constant height of 20m AGL because this value allows to obtain a controlled ground area that is feasible for most of operations. The height can be changed, and the controlled ground area can be computed according to the regulation.

Different path geometries were designed to compute the UAS time-of-flight over corners with specific characteristics. S*tandard paths* involve corners with an assigned angle multiple of the 30deg angle between the two legs. Each segment between two consecutive waypoints is 30m long and each corner leg is 15m long. The segment length was selected according to the analysis reported in Paragraph 4.3. To identify each *standard path*, the symbol “TX” was used, where X is the characteristic relative angle in degrees. The design of seven *standard paths*, i.e. seven path geometries, allowed to collect samples of corners with a 0deg relative angle to corners with a 180deg relative angle, considering a step of 30deg. During the tests, each path was executed clockwise several times. The corner performed counterclockwise were not considered because symmetrical properties are assumed. The impact of wind condition as source of asymmetric properties was accounted separately during the definition of Neural Network (NN) inputs. Each *standard path* was designed as closed path and the measurements were computed in the East North Up (ENU) reference frame. The seven standard path that were designed to collect the data are described below:

- T0. The characteristics of the path are reported in Table 2 and the geometry of the path is showed in Fig. 17. The path includes 5 outer waypoints and 1 inner waypoint. The UAS performs each segment in both directions. To fly from one segment to another one, the UAS performs a 72deg corner. However, this type of corner was not considered in the training dataset.

Table 2. Characteristics of the path T0.

| **Parameter** | **Value** |
|---|---|
| Characteristic angle | 0degrees |
| Number of waypoints | 6 |
| Number of segments | 5 |
| Shape | Star shape geometry |
| Geometry | Fig. 17 |

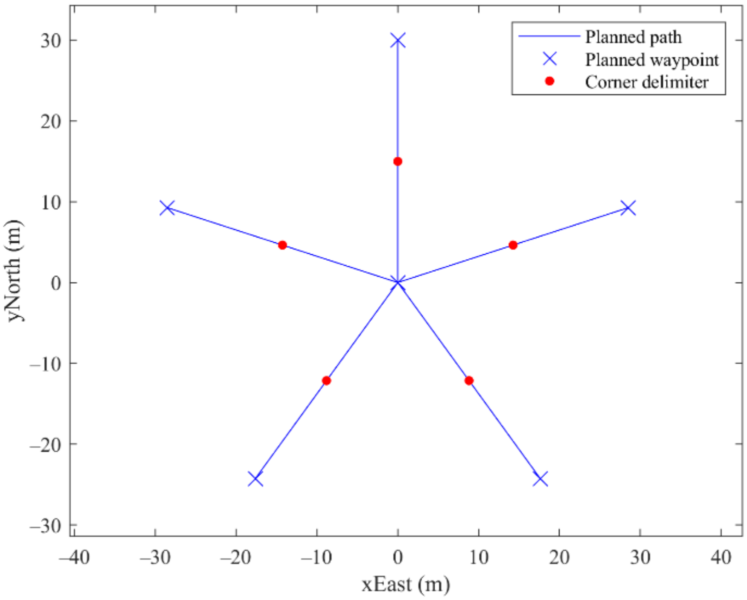

Fig. 17. Path T0 geometry. ENU reference frame centered at WP1.

- T30. The characteristics of the path are reported in Table 3 and the geometry of the path is showed in Fig. 18. The path includes 5 segments: the first 4 segments are arranged in 30deg corners, and they are 30m long. Instead, the fifth segment allows to execute a closed path and it is 31m long. The corners that have the fourth-fifth and fifth-first segments as legs do not include a 30 deg relative angle. So, type of corner was not considered in the training dataset.

Table 3. Characteristics of the path T30.

| **Parameter** | **Value** |
|---|---|
| Characteristic angle | 30degrees |
| Number of waypoints | 5 |
| Number of segments | 5 |
| Shape | sawtooth shape geometry |
| Geometry | Fig. 18 |

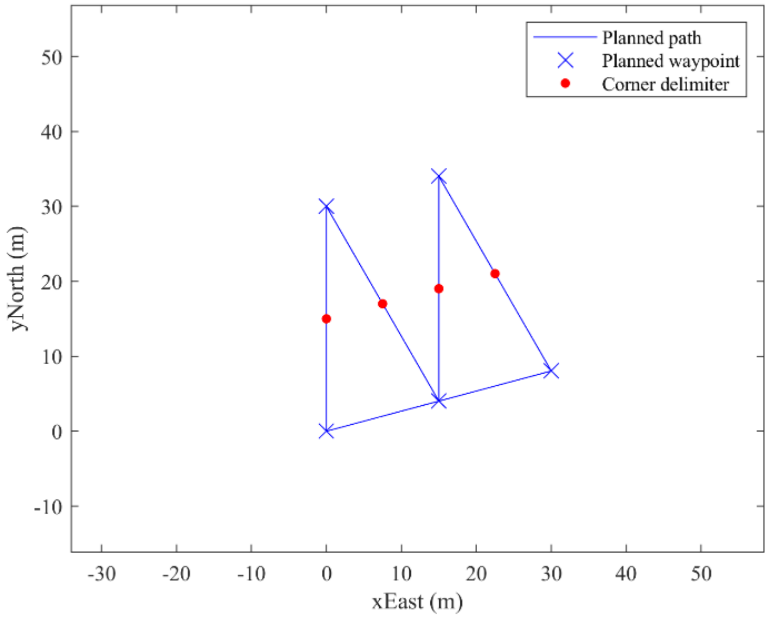

Fig. 18. Path T30 geometry. ENU reference frame centered at WP1.

T60. The characteristics of the path are reported in Table 4 and the geometry of the path is showed in Fig. 19. The path was designed based on the equilateral triangle shape.

Table 4. Characteristics of the path T60.

| **Parameter** | **Value** |
|---|---|
| Characteristic angle | 60degrees |
| Number of waypoints | 3 |
| Number of segments | 3 |
| Shape | triangle shape geometry |
| Geometry | Fig. 19 |

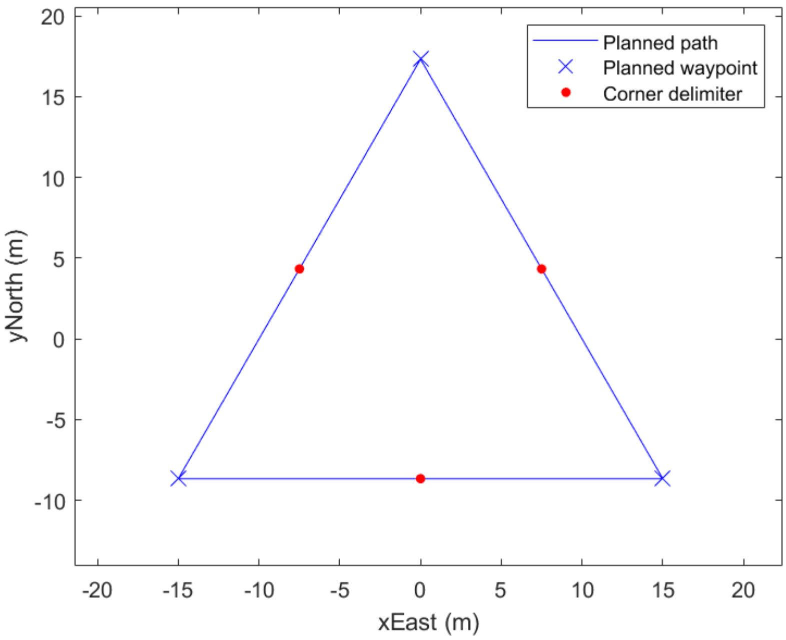

Fig. 19. Path T60 geometry. ENU reference frame centered at WP1.

- T90. The characteristics of the path are reported in Table 5 and the geometry of the path is showed in Fig. 20. The path was designed based on the square shape.

Table 5. Characteristics of the path T90.

| **Parameter** | **Value** |
|---|---|
| Characteristic angle | 90degrees |
| Number of waypoints | 4 |
| Number of segments | 4 |
| Shape | square shape geometry |
| Geometry | Fig. 20 |

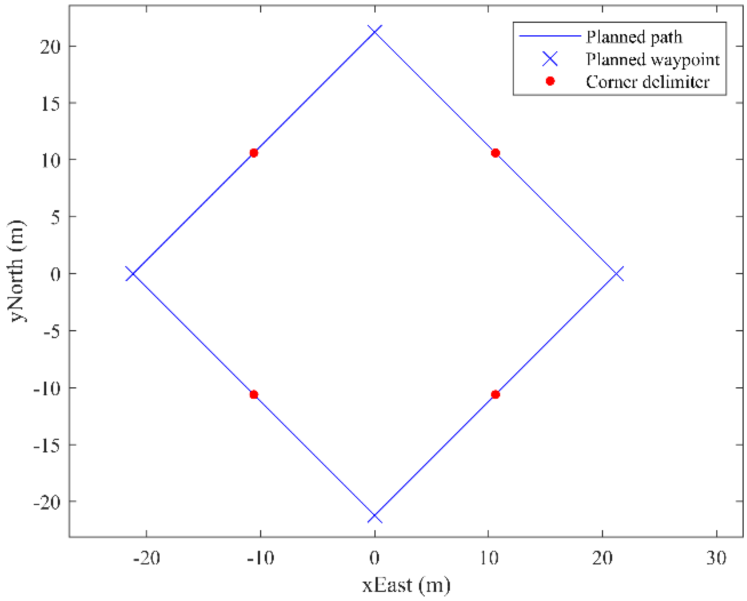

Fig. 20. Path T90 geometry. ENU reference frame centered at WP1.

T120. The characteristics of the path are reported in

- Table 6 and the geometry of the path is showed in Fig. 21. The path was designed based on the hexagon shape.

Table 6. Characteristics of the path T120.

| **Parameter** | **Value** |
|---|---|
| Characteristic angle | 120degrees |
| Number of waypoints | 6 |
| Number of segments | 6 |
| Shape | hexagon shape geometry |
| Geometry | Fig. 21 |

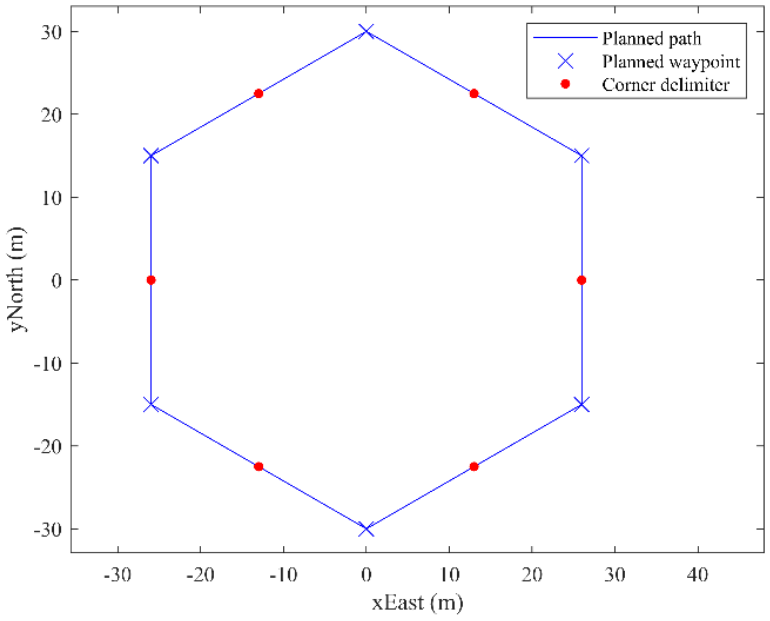

Fig. 21. Path T120 geometry. ENU reference frame centered at WP1.

- T150. The characteristics of the path are reported in Table 7 and the geometry of the path is showed in Fig. 22. The path was designed based on the dodecagon shape.

Table 7. Characteristics of the path T150.

| **Parameter** | **Value** |
|---|---|
| Characteristic angle | 150degrees |
| Number of waypoints | 12 |
| Number of segments | 12 |
| Shape | dodecagon shape geometry |
| Geometry | Fig. 22 |

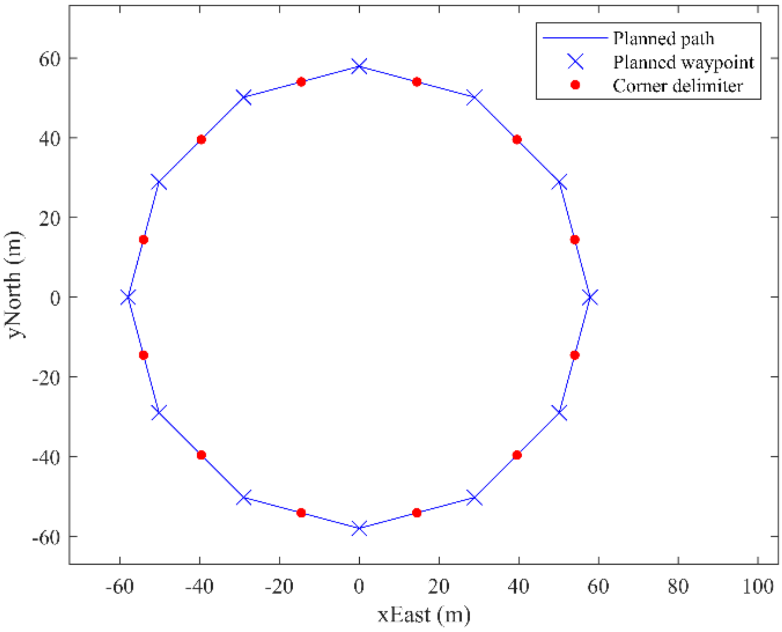

Fig. 22. Path T150 geometry. ENU reference frame centered at WP1.

- T180. The characteristics of the path are reported in Table 8 and the geometry of the path is showed in Fig. 23. The path was designed based on the straight line shape.

Table 8. Characteristics of the path T180.

| **Parameter** | **Value** |
|---|---|
| Characteristic angle | 180degrees |
| Number of waypoints | 2 |
| Number of segments | 3 |
| Shape | straight line shape geometry |
| Geometry | Fig. 23 |

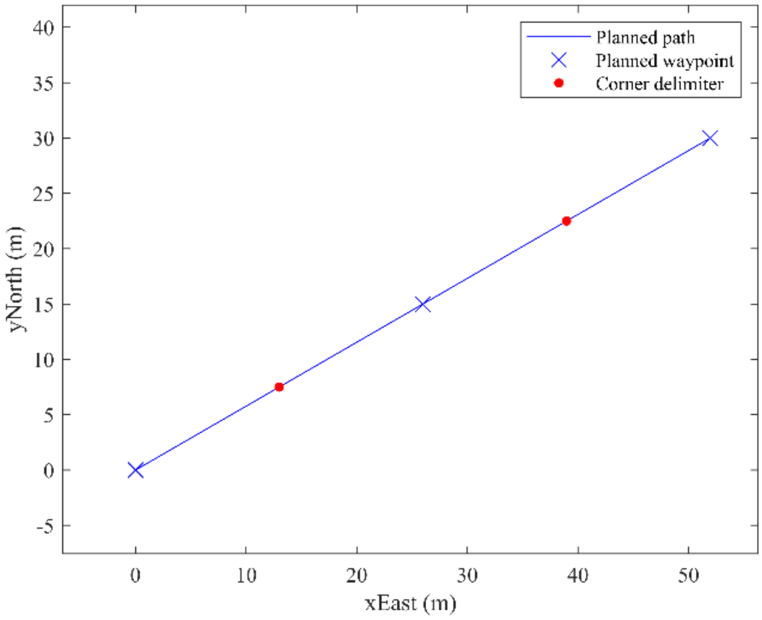

Fig. 23. Path T180 geometry. ENU reference frame centered at WP1.

The corner angle is a critical parameter for UAS time-of-flight estimation because if the relative angle is small, the UAS needs less time to execute the corner. However, this behavior is not linear. Thanks to the ground station software, the *stop and turn* setting was activated. This mode allows the remote pilot to monitor the surrounding area by using the on-board camera and act proper actions if needed.

Considering the *stop and turn* mode along the path, the UAS accelerates at the beginning of each segment, reaches a constant speed according to the assigned ground speed limit, i.e. 5m/s,  and decelerates. The central part of each segment between two waypoints is defined as constant-speed part. This method aims at predicting the UAS flight-time over the corner, i.e. the time-of-flight over the deceleration section before the turn, the stop, and the acceleration section after the turn. In this way, the remaining time-of-flight to be estimated is over the constant-speed part that can be easily computed.

A preliminary analysis is needed to choose the length of segments and corner legs that allows to have a non-zero constant-speed segment length. So, preliminary flight tests were executed to fix the mentioned length values.

## 4.3. Preliminary Flight Tests

T60 and T180 paths were selected to develop preliminary test. The tests were executed at 5m/s speed in same wind conditions.

The segment length for the selected path is 30m and 40m. The aim of the tests is finding the smaller segment length that allows a non-zero constant-speed section length, i.e. a constant-speed section outside the corner, and the UAS must have the almost same speed at the initial and final corner points. The UAS performed T60 and T180 paths three times.

The UAS telemetry was analyzed to find the initial and final points in which the ground speed is lower that one standard deviation with respect to the nominal one. Then, the length of the constant-speed section and the time-of-flight that the UAS needed to fly the constant-speed section were computed for each segment of T60 and T180 paths.

The results of T60 and T180 paths with 30m and 40m segment length were compared and reported in Table 9 where the data were averaged for all laps of T60 and T180 paths.

Table 9. Preliminary flight test results. Data were computed for each constant-speed section and then averaged for all laps of T60 and T180 paths.

| | **T60** | | **T180** | |
|---|---|---|---|---|
| | **40m** | **30m** | **40m** | **30m** |
| Ground Speed Mean Value (m/s) | 5.0 | 5.0 | 5.0 | 5.0 |
| Ground Speed Std deviation (m/s) | 0.2 | 0.2 | 0.2 | 0.2 |
| Distance Corner side length Mean Value (m) | 32 | 22 | 33 | 22 |
| Distance Corner side length Std deviation (m) | 0.6 | 0.5 | 0.4 | 0.4 |
| Flight-Time Mean Value (s) | 6.5 | 4.5 | 6.6 | 4.5 |
| Flight-Time Std deviation (s) | 0.13 | 0.07 | 0.16 | 0.12 |

The results about the constant-speed section T180 paths with 40m and 30m are reported in Fig. 24. The boundaries of the constant-speed section along each lap of T180 path with 40m segments are showed in Fig. 24 (a) and Fig. 24 (c). The ground speed amplitude along each lap of T180 path with 30m segments are showed in Fig. 24 (b) and Fig. 24 (d). For paths with 40 m segments the corner length is 40m, for paths with 30m segments the corner length is 30m. The analysis shows that the ground speed is well controlled because the mean value is equal to the nominal value and the standard deviation is within 5% of the nominal value. Moreover, the length of the acceleration and deceleration parts is constant and equals to 4m. The paths with 30m segments can be selected in order to reduce the path size and the time of test execution. So, the reference corner has a length of 15m that is compatible with the typical size of most building and common UTM operations.

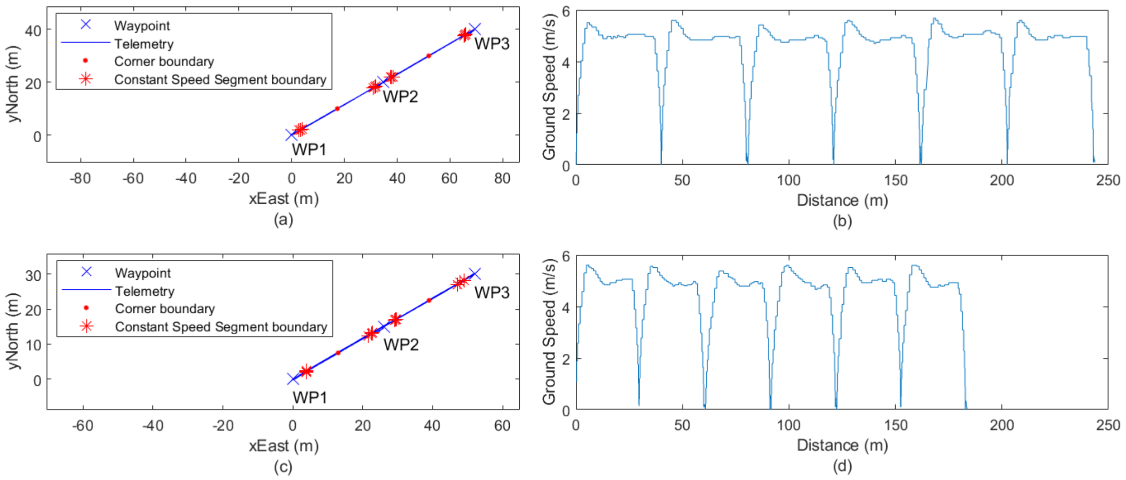

Fig. 24. Analysis of T180 path ground speed. (a) T180 path with 40m segments, ENU reference frame centered at WP1; (b) Amplitude of ground speed along the T180 path with 40 m segments; (c) T180 path with 30m segments, ENU reference frame centered at WP1; (d) Amplitude of ground speed along the T180 path with 30m segments.

DL based methods need a dataset to be trained. A proper analysis is required to estimate the minimum number of samples that are needed to train the algorithm. The Chi-square approach was used by exploiting the upper threshold of Eq. 1 [81] to compute $n$, i.e. the minimum number of required samples to obtain the desired standard deviation. The 95% confidence level was considered, where the values of the Chi-Squared variables are $\chi_1^2$=74.2219 and $\chi_2^2$=129.561. In Eq. 1 $\sigma_s$ is the desired standard deviation that is equals to 1s in the presented applications. Instead, σ is the standard deviation that was experimentally evaluated thanks to several previous test experiences [82].

$$\frac{(n-1)\sigma_s^2}{\chi_2^2} < \sigma^2 < \frac{(n-1)\sigma_s^2}{\chi_1^2} \qquad \text{Eq. 1}$$

The computed value of $n$ is about 60 by using the worst-case value of experimental $\sigma$. So, the data that were collected for the new flight tests include 60 samples for each *standard path*. The value of $\sigma$ that was computed considering the new flight tests is σ=0.87s. So, $n$ is equals to 57 by using Eq. 1. However, $n$=57 is the worst-case minimum number of samples, because considering the specific value of $\sigma$ for each *standard path*, the minimum number of required samples can be reduced for the standard paths that have a lower $\sigma$. The value of $n$ for each *standard path* is reported in Table 10.

Table 10. Minimum number of samples required for each *standard path*.

| **Path ID** | **N samples** | **Std (m)** |
|---|---|---|
| T0 | 17 | 0.5 |
| T30 | 7 | 0.3 |
| T60 | 8 | 0.3 |
| T90 | 18 | 0.5 |
| T120 | 57 | 0.9 |
| T150 | 26 | 0.6 |
| T180 | 5 | 0.2 |

To carry out the prediction method of the time-of-flight, it must be assured that there are reasonable spatial deviations between the performed trajectory and the planned path. So, two main types of deviation were computed.

- Vertical deviations, i.e. deviations with respect to the assigned AGL height of 20m.
- Horizontal deviations, i.e. deviations with respect to the assigned corner length of 30m.

Considering the vertical deviations, the hypothesis of constant AGL height can be verified thanks to the results reported in Table 11, where the main values and deviations of the UAS height are reported for each *standard path* thanks to the telemetry analysis.

Table 11. Analysis of vertical deviations for each *standard path*.

| **Path ID** | **Height Mean Value (m)** | **Height Std (m)** |
|---|---|---|
| T0 | 19.9 | 0.2 |
| T30 | 20.0 | 0.2 |
| T60 | 20.0 | 0.2 |
| T90 | 19.9 | 0.2 |
| T120 | 20.0 | 0.2 |
| T150 | 20.0 | 0.2 |
| T180 | 19.9 | 0.2 |

Considering the horizontal deviations, the nominal boundaries of the corner were computed considering a nominal distance of 15m from the assigned waypoint. The telemetry data associated to each corner were computed considering the telemetry points that are closer to the nominal corner boundaries, i.e. $S_i$ and $F_i$ in Fig. 15, according to the minimum Euclidean distance. The main values and deviations of the UAS horizontal position are reported for each *standard path* in Table 12 thanks to the telemetry analysis.

Table 12. Analysis of horizontal deviations for each *standard path*.

| **Path ID** | **Corner Length Mean Value (m)** | **Corner Length Std (m)** |
|---|---|---|
| T0 | 30.0 | 0.4 |
| T30 | 30.0 | 0.6 |
| T60 | 30.0 | 0.4 |
| T90 | 30.0 | 0.5 |
| T120 | 30.0 | 0.4 |
| T150 | 30.0 | 0.4 |
| T180 | 30.0 | 0.4 |

## 4.4. Time-of-Flight Prediction

The Trajectory Based Operations (TBO) [83] concept allows to develop reliable and high-performance strategies to manage several vehicles that populate the same air sector. The use of 4D trajectories increases the safety level of flight management and development of standard procedures. This work proposes a DL based time-of-flight predictor that can be used to predict the time to collision in a multiple UASs scenario.

### 4.4.1. Overview

TP techniques are useful to develop advanced ATM tools for TBO following specific requirements, such as [84]. The main challenge related to the integration of UASs in civil airspace involves the evaluation of the total risk level with respect to the traditional traffic. The time of flight needed by a UAS to fly a generic path is a critical parameter to be predicted and it is crucial at strategical and tactical phases in the UTM context. Conflict detection allows to identify if a collision happens among platforms in a proper time interval.

The adoption of TBO must be supported by the integration of flights data systems to manage the flights before the departure and acts proper route changes during the trajectory execution. The Trajectory Management and the Conflict Detection and Resolution tasks are critical features of UTM, and TP methods can support a harmonized integration of these tasks in UTM context.

### 4.4.2. Method Implementation

The time-of-flight was computed by the UAS telemetry files. Specifically, the time-of-flight needed by the UAS to fly over each corner of the planned *standard paths* was computed. Then, the mean value and the standard deviation value were computed considering each *standard path*. A threshold of $3\sigma$ was set to neglect the data with high variability. The corners with a time-of-flight that exceeds the threshold were discarded. The final dataset includes 442 sample, as reported in Table 13. The mean value and the standard deviation value were computed for the new dataset to check that the time-of-flight does not exceeds the threshold. The final dataset was used to train and test the developed NN.

Table 13. Number of samples for each *standard path*.

| **Path ID** | **Number of valid samples** |
|---|---|
| T0 | 75 |
| T30 | 55 |
| T60 | 58 |
| T90 | 69 |
| T120 | 59 |
| T150 | 68 |
| T180 | 58 |

The proposed method was developed as a classifier, the NN predicts the UAS time-of-flight over the 15m corner receiving inputs collected in categories, where each category has a specific path geometry and wind condition.

The NN was developed thanks to the MATLAB® Deep Learning Toolbox™. The NN was developed as a classifier processing the input parameters to obtain a limited number of categories. The NN characteristics were selected according to the investigated problem and compared with other approaches, as reported in Paragraph 4.5. Specifically, a feedforward NN with the Bayesian Regularization Backpropagation algorithm as training function [85] was developed because this training function allows to better manage high variability data with good generalization properties [86] [87] [88]. The NN architecture was selected comparing the performance obtained with different structures. The NN inputs are:

- The clockwise angle between the corner legs that is computed from the second leg to the first leg.
- The clockwise angle between the first corner leg and the wind direction.
- The clockwise angle between the second corner leg and the wind direction.
- The wind intensity category based on the Beaufort scale [89].

Official weather forecast was used to estimate the wind intensity and direction. The use of the Beaufort scale for the wind intensity and the standard paths allowed to obtain a limited number of input categories that can be used by the NN. The flight tests were performed at a wind intensity of 5kts and a wind direction of 60deg from the North direction. A wind intensity from 0kts to 10kts is a typical allowable value for most UAS operations and it corresponds to the first four Beaufort categories. According to regulation guidelines [7], the wind condition must be carefully monitored during the flight and the mission must be stopped if critical conditions happen. Analyzing the weather archives of the flight test area, a wind intensity of 5kts is the most common wind intensity condition over one year that corresponds to the second Beaufort category.

To develop the NN, the epoch number was limited to 1000. The dataset includes 442 samples: the training phase used the 85% of the samples and the test phase the remaining 15%. The Bayesian Regularization Backpropagation training function of the Deep Learning Toolbox$^{TM}$ does not need a validation dataset because it involves an internal validation process. The application of a 3σ threshold to reduce data variability and a random selection of data included in training and test datasets allows to reduce the dependency of method performance with respect to the acquired datasets. The main parameters of the developed method are reported in Table 14.

Table 14. Characteristics of the developed Neural Network.

| **NN Parameter** | **Value** |
|---|---|
| Training Function | Bayesian Regularization Backpropagation function |
| Network Type | Feedforward fully connected NN |
| Dataset: Training, Validation, and Test | 85%, 0%, 15% |
| Epochs number | 1000 |
| Number of input data | 4 |
| Number of output data | 1 |

The Normalized Root Mean Square Error (NRMSE) that is reported in Eq. 2 was used to assess the NN performance. The true and the predicted value of time-of-flight over a corner are respectively indicated as $x_t$ and $x_p$, the number of samples as $N$.

$$\text{NRMSE} = \sqrt{\frac{1}{N}\sum_{i=1}^{N}\left(\frac{x_t - x_p}{x_t}\right)^2} \qquad \text{Eq. 2}$$

The structure of the NN can be investigated considering the two-layer NN with different neurons in each layer. The NN performance of the test phase was used to compare different NN structures, as reported in Fig. 25 where the horizontal axis shows the sum of neurons in the two layers considering the neurons displacement with the best performance. The NN structure with 4 and 6 neurons achieved the best solution and its performance in training and test phases are reported in Table 15.

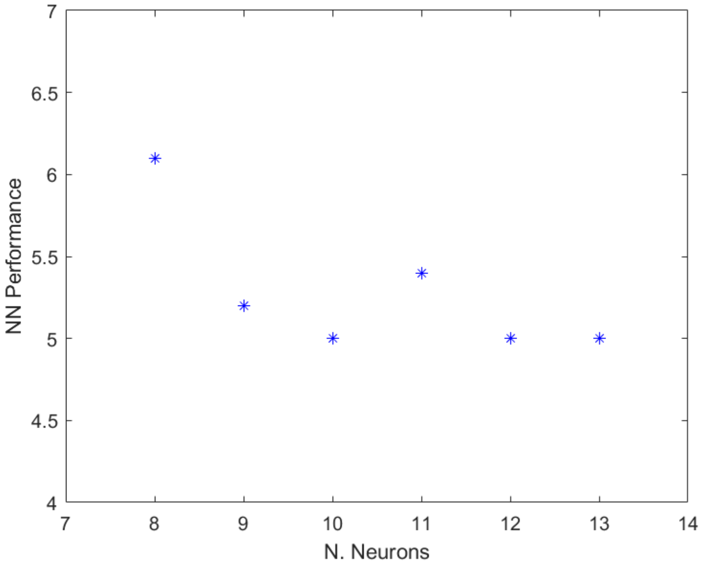

Fig. 25. NN performance of the test phase varying the total number of neurons in the two layers.

Table 15. Performance of the NN with 4 and 6 neurons in the two hidden layers in training and test phases.

| **NN Performance** | **Training Phase** | **Test Phase** |
|---|---|---|
| NRMSE (Eq. 2) | 4.5% | 5.0% |

### 4.4.3. Method Test and Results

After the NN assessment, *generic paths* were designed to test the generalization capability of the proposed method in the same wind conditions of the *standard paths*. The flights were performed in a proper test area, but the *generic paths* were designed to reproduce urban UAS applications.

The proposed method predicts the time-of-flight over a corner, so the prediction of the time-of-flight over a generic path can be performed summing the time-of-flight values over each corner if the path only includes segment with 30m length. This case is referred as Case 1. Otherwise, if the path involves segments longer than 30m, the time-of-flight over the path can be computed summing the time-of-flight over each corner and the time-of-flight over the remaining segment parts that are constant-speed sections according to the analysis reported in Paragraph 4.3. The time-of-flight over the constant-speed sections can be computed dividing the length of the constant-speed segment by the nominal ground speed, i.e. 5m/s. This case is referred as Case 2.

Four *generic paths* were designed, and they are called with incremental numbers from Test path 1 to Test path 4, as summarized in Table 16. Test path 1 and Test path 3 belong to Case 1. Test path 2 and Test path 4 belong to Case 2.

Table 16. Classification of designed *generic paths*.

| **Case ID** | **Time-of-flight contributions** | **Test path ID** |
|---|---|---|
| Case 1 | -Predicted time-of-flight over each corner | Test path 1 |
| | | Test path 3 |
| Case 2 | -Predicted time-of-flight over each corner<br>-Time-of-flight over constant-speed sections | Test path 2 |
| | | Test path 4 |

1) Case 1. Test path 1 and Test path 3 are included in Case 1.
   Test path 1 is showed in Fig. 26 (a) and Fig. 26 (b) and it reproduces a surveillance mission, for example over an urban crowded area. Our University main entrance

was considered as possible area. The path includes 10 segments with the same length of 30m. The UAS executes the path three times. The first section of the first segment and the last section of the last segment of the path are not included in a corner. However, this contribution is smaller than the flight-time values that are predicted by the NN.

Test path 3 includes 9 segments with the same length of 30m. The UAS executes the path three times. The path is the red path in Fig. 27.

2) Case 2. Test path 2 and Test path 4 are included in Case 2.

   Test path 2 is showed in Fig. 26 (c) and Fig. 26 (d) and it reproduces an urban canyon scenario with corridors and buildings. The path includes 9 segments with different length values longer than 30m. The UAS executes the path one time.

   Test path 4 includes 8 segments with different length values longer than 30m. The UAS executes the path three times. The path is the black path in Fig. 27.

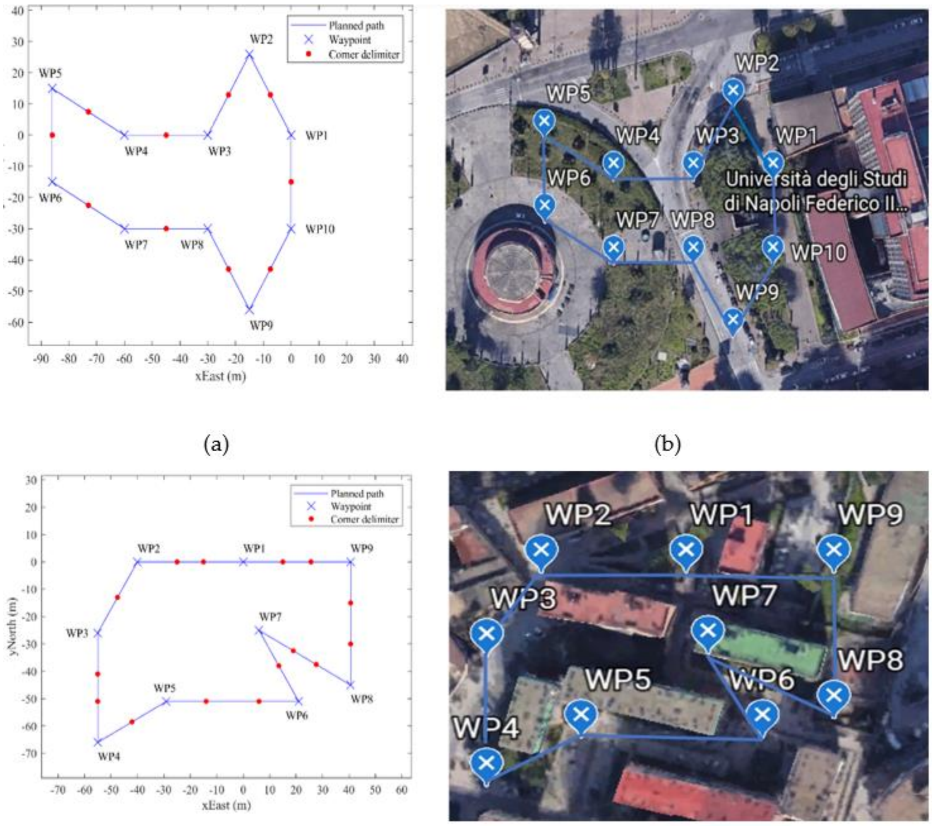

(a) (b)

(c) (d)

Fig. 26. *Generic paths*. (a) Test path 1, ENU reference frame centered at WP1. (b) Test path 1 in urban environment, Google Earth® view. (c) Test path 2, ENU reference frame centered at WP1. (d) Test path 2 in urban environment, Google Earth® view.

The true time-of-flight that was obtained by the telemetry files was compared with the time-of-flight that was computed according to Case 1 and Case 2 strategies and the percent error Eq. 2 was computed. Moreover, a benchmark was considered dividing the nominal distance by the nominal ground speed. The results are reported in Table 17. A percent error less than 1% was obtained for the shortest path. A percent error lower than 3.2% was obtained for the worst case. So, the proposed method can match the requirements for safe prediction, also considering the larger errors of the benchmark.

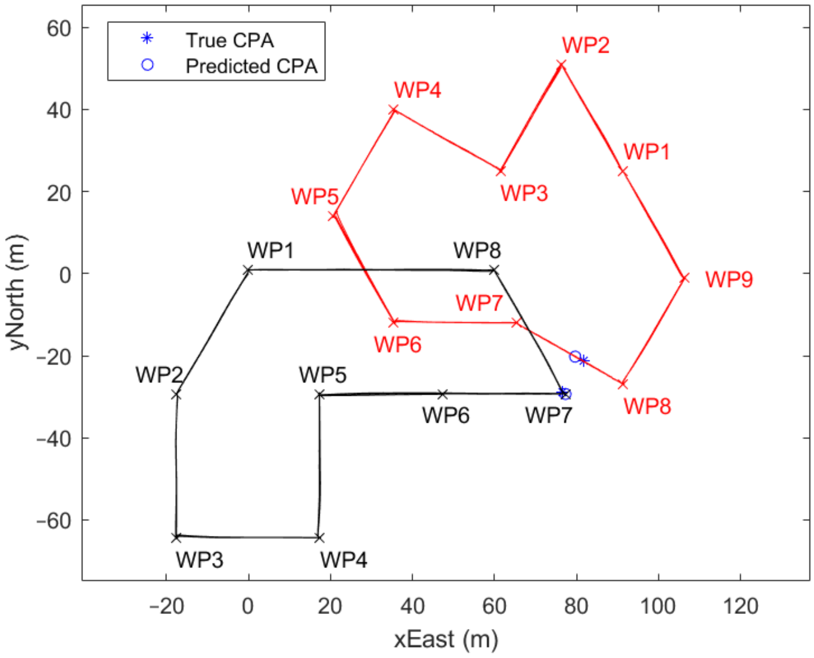

Fig. 27. Test path 3 in red and Test path 4 in black. ENU reference frame centered at WP1. The blue star indicates the true CPA during the first lap, the blue circle indicates the predicted CPA during the first lap.

Table 17. Comparison among the true, predicted, and benchmark time-of-flight for the four *generic paths*.

| **Method Performance** | **Test path 1**<br>**3 laps** | **Test path 2**<br>**1 lap** | **Test path 3**<br>**3 laps** | **Test path 4**<br>**3 laps** |
|---|---|---|---|---|
| True time-of-flight (s) | 272.3 | 97.1 | 239.6 | 245.3 |
| Predicted time-of-flight (s) | 263.6 | 96.9 | 240.1 | 250.2 |
| Percent error between true and predicted time-of-flight | 3.2 % | 0.2 % | -0.2 % | -2.0 % |
| Time-of-flight at nominal ground speed - benchmark (s) | 180.0 | 69.1 | 162.0 | 177.0 |
| Percent error between true and benchmark time-of-flight | 34 % | 29 % | 32 % | 28 % |

The proposed method was tested for a typical UTM task, such as collision detection. Test path 3 and the Test path 4 were used as crossing paths to predict the time to the Closest Point of Approach (CPA). The UAS performed the two paths at different time, but the telemetry data of Test path 3 were translated to obtain a path that intersects the Test path 4. In Fig. 27 the translated Test path 3 is shown in red and the Test path 4 in black. The time stamp of Test path 3 was aligned with the start time of Test path 3. The final configuration that was obtained involves two UASs flying simultaneously along crossing paths. The paths were executed three times. The CPA represents the point where there is the minimum distance between the UASs. The distance between the two UASs must be monitored to evaluate if it is larger than a safe threshold. Instead, the time-of-flight to the CPA must be computed to evaluate if the remaining time before collision allows proper corrective actions. The time-of-flight to the CPA was computed thanks to telemetry files and predicted thanks to the proposed learning method. The two procedures are described below.

1) True time-of-flight to the CPA. Thanks to the telemetry data, the distance between the two UASs can be computed for each time instant. The CPA was computed for each lap and the time-of-flight to reach the CPA can be computed from the start time. The sampling rate of telemetry file is less than 0.3s and it affects the computation of distance between the two UAS.
2) Predicted time-of-flight to the CPA. The proposed method allows to predict the time-of-flight to the CPA in strategical points of the path, when the UAS is at the waypoint, at the initial and final corner points, and along constant-speed sections. At the beginning Test path 3 was considered as reference path. The position of the UAS along Test path 4 was computed for each strategical point position of the UAS along Test path 3. If the position of the UAS along Test path 4 belongs to strategical points, the distance between the UASs can be directly computed. Otherwise, the position of the UAS along Test path 4 UAS was interpolated and then the distance between the UAS was computed. This procedure was repeated with the Test path 4 as reference path. At the end, the CPA is the point of each lap where there is the minimum distance between the two UASs and the time-of-flight to the CPA was computed from the start time.

The comparison between the true and the predicted time-of-flight to the CPA is reported in Fig. 28. The blue line data were computed by using the telemetry time-of-flight. In this case, the UAS positions can be computed at high data rate. The red points data were computed in the strategical points and in interpolated positions by using the predicted time-of-flight. The red points data were computed for both Test path 3 UAS and Test path 4 reference paths.

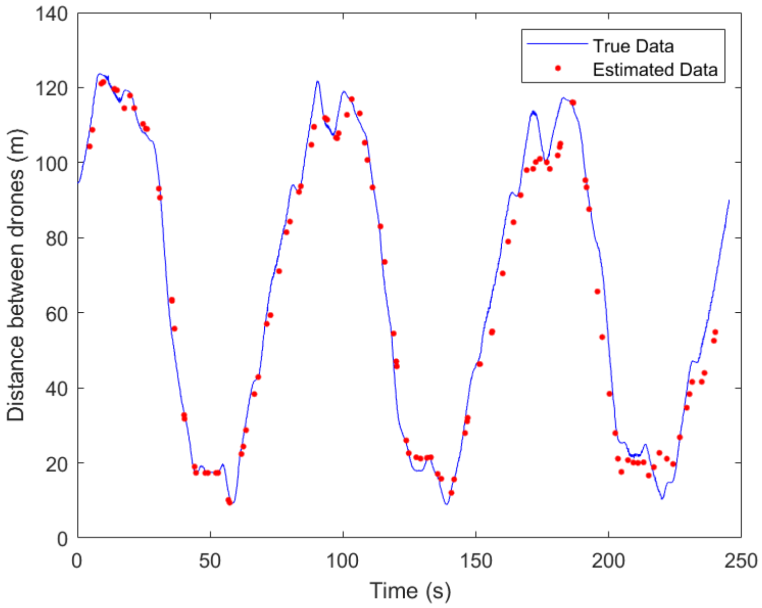

Fig. 28. Comparison of distance values between the two UASs. The blue line data were computed by using the telemetry time-of-flight, the red points data were computed by using the predicted time-of-flight.

The comparison between the true and the predicted time-of-flight to the CPA is reported in Table 18 for each of the three laps. During the first lap the difference between the true and the predicted value of the time-of-flight to the CPA is lower than 2s. During the third lap the difference is 5s. The percent error can be computed dividing the difference between the true and the predicted time-of-flight by the true value and it is about 2.3% during the third lap in the worst-case.

Considering the computational cost, if 100 UASs should be managed in the same airspace sector in 5min, about 1 million of elementary operations are needed by the proposed method to process the output. So, this method matches the requirements of UTM consoles.

The presented results shows that the collection of UAS historical data can support the development of high-performance learning solutions for conflict detection, helping the development of standard UTM tasks.

Table 18. Comparison between the true and the predicted time-of-flight to the CPA for the three laps.

| **Time-of-flight to CPA** | **Lap 1** | **Lap 2** | **Lap 3** |
|---|---|---|---|
| True time-of-flight to CPA (s) | 58.5 | 138.9 | 220.0 |
| Predicted time-of-flight to CPA (s) | 57.3 | 140.8 | 215.0 |

## 4.5. Comparison among different Machine Learning based methods

The proposed strategy was developed by using four different Machine Learning based methods to compare the obtained results for time-of-flight prediction. The used methods are analyzed in [90] and reported below.

1) Linear Regression (LR) algorithm.
2) Regression Trees (LT) algorithm.
3) Gaussian Process Regression (GPR) algorithm.
4) Support Vector Machine (SVM) algorithm.

The mentioned methods were developed by using the MATLAB® Regression Learner App. The algorithms were trained exploiting the same data collected for the proposed Deep Learning based method and proper datasets were built to compare the results. The percent error computed by using Eq. 2 for each of the four *generic paths* is reported in Table 19. As it results from the comparison between Table 15 and Table 19, the proposed DL based approach achieves better performance.

Table 19. Comparison of the percent error among the four Machine Learning based method for the four *generic paths*.

| **Method Performance** | **Test path 1**<br>**3 laps** | **Test path 2**<br>**1 lap** | **Test path 3**<br>**3 laps** | **Test path 4**<br>**3 laps** |
|---|---|---|---|---|
| **Linear Regression** | 9.9% | 9.0% | 8.9% | 13.3% |
| **Regression Tree** | 9.1% | 9.1% | 8.9% | 10.2% |
| **Gaussian Process Regression** | 7.7% | 6.0% | 6.0% | 8.1% |
| **Support Vector Machine** | 6.4% | 6.6% | 5.5% | 5.2% |

## 4.6. Battery Discharge Prediction

Most of commercial UASs are powered by batteries with limited autonomy performance. For example, multirotor UASs have about 20-30 minutes autonomy that is affected by the weather conditions. This work proposes a DL based battery discharge predictor that can be used to predict the absorbed current integral and the battery state of charge. A method to estimate the battery capacity is also presented.

### 4.6.1. Overview

The battery discharge of multi-rotor UASs is characterized by a strongly non-linear behavior. An accurate prediction of the battery level support safer operations in both strategical and tactical phases.

1) Strategical phase. Before the mission start, the UAS operator must plan the route as a series of waypoints considering the required battery level. The development of a battery consumption predictor allows to estimate the battery level required to complete the assigned route also considering different wind conditions. If more than one battery is needed to complete the mission, the predictor can also support an optimal battery management.
2) Tactical phase. During the mission execution, the UAS operator must monitor the remaining UAS battery level, changing the flight plan if external conditions occur

that increase the battery consumption. The predictor allows to evaluate if the mission should be safely terminated before its completion. An online re-planning can be supported by the proposed predictor to identify safe areas that can be reached by the UAS with the remaining battery level.

Considering battery-powered vehicles, several parameters can be analyzed to estimate the battery performance, such as State Of Charge (SOC), Remaining Useful Life (RUL), and State Of Health (SOH) [91] [92] [93] [94].

A method to predict the battery discharge of electric aircraft is presented in [95] thanks to the use of the Unscented Kalman Filter algorithm. The study defines the battery model, and the battery demand is predicted by using the battery state and loads. The battery RUL of electric vehicles can be predicted by using the approach study reported in [96] by estimating the battery SOH and using real data. A particle filter is presented in [97] and it is used with a sliding-window grey model for battery RUL prediction. In [98] four Machine-Learning-based methods are compared for battery RUL prediction of a UAS. The four methods are: Least Absolute Shrinkage and Selection, Least Squares Support Vector machines for Regression, Multi-Layer Perceptron, and Gradient Boosted Trees. A Long-Short-Term Memory (LSTM) algorithm is proposed in [99] for battery SOC prediction. Then, battery State Of Power (SOP) is estimated by using a multiple-constraints method, and a Kalman filter is adopted to estimate battery SOC and SOP. The study reported in [100] describes a LSTM approach that is used to predict the output of sensors. Then a Deep Belief Network is used to classify the faults and the battery RUL is estimated.

### 4.6.2. Method Implementation

The methodology that is described in Paragraph 4.2 can also be exploited to predict the battery consumption of an UAS over a *generic path* taking into account the wind condition, as presented in [101].

The UAS specifications report the nominal maximum time-of-flight that is often computed in different conditions, such as in hoovering for multirotor UASs or with an assigned value of wind speed. During the mission, the pilot must monitor the percent value of the battery level that is showed on the controller display or ground station. The remaining battery level, i.e. the SOC, is strongly related to the battery capacity and it is also saved in the telemetry file. The use of the battery SOC is also useful to set proper waring alarms when the battery charge level is too low.

The main aim of the work is to develop a method that allows the UAS operator to predict the battery consumption basing only on the planned route path and the weather condition. Specifically, the SOC estimation needs the knowledge of the battery capacity that is different for each battery and changes in different environmental conditions. So, the goals of the study are:

1) The prediction of the current that is absorbed onboard.
2) The prediction of the battery SOC.

The absorbed current can be computed integrating the discharge current over time. The proposed predictor that allows to estimate the future absorbed current can be applied for the methodology described in Paragraph 4.2 with any type of battery capacity.

The battery SOC estimation needs the knowledge of the absorbed current and the battery capacity. So, the prediction of the battery SOC was developed starting from the predictor of the absorbed current. However, the battery capacity estimation is challenging because it varies for different batteries -even if they belong to the same model- and for different operative conditions with non-linear performance. The battery life cycle has also a strong impact on the battery capacity.

To compute the battery SOC at a generic time instant t, $SOC_t$, the Coulomb Counting method can be used by knowing the battery SOC at the previous time instant $t_0$, the battery capacity, $Q$, and the discharge current value $c(\tau)$ according to Eq. 3.

$$SOC_t = SOC_{t_0} - \frac{1}{Q}\int_{t_0}^{t} c(\tau)d\tau \qquad \text{Eq. 3}$$

New flight tests were performed with the same UAS according to the trajectory segmentation approach described in Paragraph 4.2 and the telemetry data related to the battery discharge were saved and analyzed. The UAS battery belongs to the Mavic 2 series [78] with 3850 mAh nominal capacity.

The input parameters used to train the NN are the same that were used to develop the time-of-flight predictor:

- The clockwise angle between the corner legs that is computed from the second leg to the first leg.
- The clockwise angle between the first corner leg and the wind direction.
- The clockwise angle between the second corner leg and the wind direction.
- The wind intensity category based on the Beaufort scale.

The wind intensity and direction were computed by using the portable weather meter Kestrel 5500® [102]. The weather meter allowed to compute the wind data on a tripod with a vane mount. The data related to head and cross wind components were analyzed to estimate the wind direction with respect to the magnetic North.

The data that must be computed for each corner from the telemetry files are:

1) The time-of-flight.
2) The overall amount of absorbed current, i.e. the integral.

The time-of-flight was computed considering the telemetry points that are closer to the nominal corner boundaries, i.e. $S_i$ and $F_i$ in Fig. 15, as reported in Paragraph 4.3.

The absorbed current integral $curr_i$ of the generic $i^{th}$ corner was numerically computed by using the trapezoidal rule [103] Eq. 4 thanks to the knowledge of the current values $c_k$ and $c_{k-1}$ at the time instants $t_k$ and $t_{k-1}$.

$$curr_i = \sum_{k=1}^{K_i} \frac{c_{k-1} + c_k}{2} \left(t_k - t_{k-1}\right) \qquad \text{Eq. 4}$$

Then, the battery SOC needs to fly over a corner can be computed by using the absorbed current integral $curr_i$ in Eq. 3.

The cleaning process to remove the data with high variability was performed considering both standard deviations related to the time-of-flight and the integral of current for each corner that belongs to *standard paths*. A 3σ threshold was set and 726 samples was obtained to train the DL based method. The reduction of data variability and the random selection of data in training and test datasets reduce the dependency of method performance with respect to the acquired datasets.

A feedforward NN was developed to predict the absorbed current integral by using the MATLAB® Deep Learning Toolbox™. The same parameters used for the time-of-flight predictor were adopted, as reported in Table 14, specifically the Bayesian Regularization Backpropagation function.

The NRMSE in Eq. 2 was used to compute the performance of both NNs, where $x_t$ and $x_p$ represent the true and predicted value of the absorbed current integral over a corner. The samples were randomly assigned to training and test datasets. However, each NN training was repeated 10 times for different NN configurations in terms of layers and number of neurons and the average NRMSE value was considered to estimate the NN performance. NNs with one and two layers were investigated varying the number of neurons in each layer. The maximum number of neurons in each layer that was considered is 10 because in this range a constant value of NRMSE is reached.

The 2-layer NN shows better performance with respect to the 1-layer NN. To identify the minimum number of neurons in each layer that allows to achieve the required performance, the NRMSE in percentage and the relative number of effective parameters R in percentage were computed by using the MATLAB® routine [104]. The relative number of effective parameters is obtained dividing the number of effective parameters by the total number of parameters used by the NN.

The performance of 2-layer NNs are reported in Fig. 29. The NRMSE value in percentage is reported on the left axis, and the R value in percentage is reported on the right axis for different numbers of neurons. The number of neurons is the sum of neurons in both layers. If two or more NNs have the same number of neurons displaced in layers in different way, the NN with the lowest NRMSE value was reported.

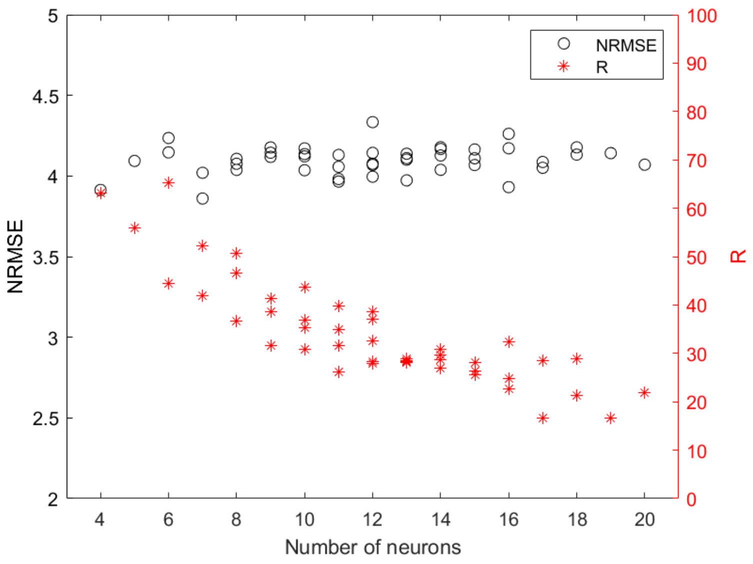

Fig. 29. Performance of 2-layer NNs in terms of percent NRMSE (left axis) and percent R (right axis) for different numbers of neurons.

The region with almost constant R values was identified in Fig. 29 and the NN with 5 and 6 neurons was selected because it showed the best performance in terms of NRMSE.

The performance of the absorbed current integral predictor is reported in Table 20 for training and test datasets.

Table 20. NRMSE and R percent values for training and test datasets. The absorbed current integral predictor has 5 and 6 neurons.

| | **NN for absorbed current integral prediction** |
|---|---|
| **NRMSE training** | 3.88% |
| **NRMSE test** | 3.98% |
| **R** | 39.7% |

### 4.6.3. Battery Capacity Estimation

*Standard paths* were also used to estimate the battery capacity. The results obtained in Paragraph 4.6.4 by using the battery discharge predictor exploited an experimental value of UAS battery capacity. Five LiPo batteries model DJI® Mavic 2 Intelligent Flight batteries were adopted to perform the *standard paths*. The identification numbers used to name the batteries are B01, B02, B03, B04, and B05.

The acquisition of the samples for the predictor training needed more than one flight over the same *standard path* because the average UAS autonomy is about 20 minutes. Considering the generic $j^{th}$ flight, the relation that links the battery SOC at the end and the beginning of the path, i.e. $SOC_{j,end}$ and $SOC_{j,start}$, and the integral of the current $c(\tau)$ thanks to the battery capacity is reported in Eq. 5 where $\tilde{Q}_j$ is the experimental battery capacity.

$$SOC_{j,end} = SOC_{j,start} - \frac{1}{\tilde{Q}_j}\int_{t_{j,start}}^{t_{j,end}} c(\tau)d\tau \qquad \text{Eq. 5}$$

In Eq. 5 the unknown parameter is the battery capacity $\tilde{Q}_j$, the values $SOC_{j,end}$ and $SOC_{j,start}$ can be computed by the telemetry files and the current integral can be numerically computed by using Eq. 6, where $c_{k-1}$ and $c_k$ are the values of current respectively at time instant $t_{k-1}$ and $t_k$ and $K_j$ is the number of samples in the telemetry files.

$$curr_j = \sum_{k=1}^{K_j} \frac{c_{k-1} + c_k}{2} (t_k - t_{k-1}) \qquad \text{Eq. 6}$$

The experimental battery capacity $\tilde{Q}_j$ can be estimated for the generic $j^{th}$ flight according to Eq. 7.

$$\tilde{Q}_j = -\frac{curr_j}{SOC_{fin,j} - SOC_{in,j}} \qquad \text{Eq. 7}$$

The experimental values battery capacity for each flight of *standard paths,* i.e. $\tilde{Q}_j$, and the average value of battery capacity for each type of *standard path,* i.e. $Q_{mean}$, were reported in Table 21 for the used batteries from B01 to B05.

Table 21. Experimental value of battery capacity $\tilde{Q}_j$ for each flight of *standard paths* and mean value of battery capacity $Q_{mean}$ for each type of *standard path*.

| **Battery** | ***Standard Path*** | $\tilde{Q}_j$ **(As)** | $Q_{mean}$ **(As)** |
|---|---|---|---|
| B01 | T30-1 | 12093 | 12234 |
| | T90-2 | 12370 | |
| | T120-1 | 12181 | |
| | T180-2 | 12291 | |
| B02 | T0-2 | 12236 | 12522 |
| | T30-2 | 12372 | |
| | T30-3 | 12667 | |
| | T60-1 | 12358 | |
| | T150-1 | 12583 | |
| | T180-3 | 12881 | |
| | T180-4 | 12556 | |
| B03 | T0-1 | 12111 | 12025 |
| | T0-4 | 11907 | |
| | T60-2 | 11986 | |
| | T90-1 | 12095 | |
| B04 | T0-3 | 12884 | 12699 |
| | T150-2 | 12514 | |
| B05 | T120-2 | 12810 | 12944 |
| | T180-1 | 13079 | |

Each flight of *standard path* in Table 21 is indicated with the standard nomenclature “TX”, where X is the characteristic angle, and an incremental number to identify the flights that belong to the same *standard path*.

The obtained values of battery capacity $Q_{mean}$ were used in the Paragraph 4.6.4 to predict the battery discharge.

### 4.6.4. Method Test and Results

To test the proposed method also for the prediction of the absorbed current integral, the four *generic paths* reported in Fig. 26 and Fig. 27 were used. The performance of the proposed absorbed current integral predictor over the four *generic paths* is reported in Table 22.

Table 22. Performance of the absorbed current integral predictor for the four *generic paths*.

| **Method Performance** | **Test path 1**<br>**3 laps** | **Test path 2**<br>**1 lap** | **Test path 3**<br>**3 laps** | **Test path 4**<br>**3 laps** |
|---|---|---|---|---|
| **NRMSE** | 13.79% | 16.28% | 13.94% | 16.66% |

Test path 1 and Test path 2 include same length segments, so all the values of the absorbed current integral over corners were summed to obtain the predicted battery discharge over the whole path. Instead, Test path 3 and Test path 4 involve different length segments, so all the values of the absorbed current integral over corners were summed adding proportional values for the constant-speed segments outside the corners. The added values were computed considering the average value of current integral that was estimated thanks to flight tests along T180 paths. The values of true and predicted absorbed current integral are reported in Table 23 for one lap of the four *generic paths*.

Table 23. Comparison between the true and the predicted values of the absorbed current integral for the four *generic paths*.

| | **Test path 1**<br>**1 lap** | **Test path 2**<br>**1 lap** | **Test path 3**<br>**1 lap** | **Test path 4**<br>**1 lap** |
|---|---|---|---|---|
| **True absorbed current integral (As)** | 962.4 | 884.6 | 853.2 | 984.6 |
| **Predicted absorbed current integral (As)** | 927.8 | 839.8 | 836.8 | 967.5 |

The variation of battery SOC generated by the flight over the $i^{th}$ corner, i.e. $\Delta SOC_i$, can be defined by Eq. 8 as the difference between the initial value $SOC_{i,in}$ and the final value $SOC_{i,fin}$ computed at the corner boundaries.

$$\Delta SOC_i = SOC_{i,in} - SOC_{i,fin} \qquad \text{Eq. 8}$$

The variation of battery SOC can be computed according to Eq. 9 by inverting Eq. 3. The corner boundaries identified in the telemetry files are respectively named $F_{ti}$ and $S_{ti}$. $\tilde{Q}$ is the estimated battery capacity. The accuracy of the predicted $\Delta SOC_i$ is strongly related to the battery estimation. A method to estimate the actual battery capacity is proposed in Paragraph 4.6.3, otherwise, the nominal battery capacity that is reported in the battery manual can be used.

$$\Delta SOC_i = \frac{1}{\tilde{Q}} \int_{S_{ti}}^{F_{ti}} c(\tau) d\tau \qquad \text{Eq. 9}$$

The proposed strategy was used to predict the battery SOC over *generic paths*. The flight tests were conducted by using the following batteries:

- B01 for Test path 1 and Test path 2;
- B02 for Test path 3;
- B03 for Test path 4.

The four *generic paths* were executed four times. The true ΔSOC was computed for each path as the difference between the battery SOC at the first waypoint of the first lap and the battery SOC at the last waypoint of the last lap. The predicted ΔSOC was computed by using the proposed predictor according to Eq. 9. The comparison between the true and the predicted battery ΔSOC and the absorbed current integral is shown in Table 24.

Table 24. Comparison between the true and predicted values of battery ΔSOC and absorbed current integral for four laps of *generic paths*.

| | **Test path 1 4 laps** | **Test path 2 4 laps** | **Test path 3 4 laps** | **Test path 4 4 laps** |
|---|---|---|---|---|
| **True Battery ΔSOC** | 32% | 30% | 27% | 32% |
| **Predicted Battery ΔSOC** | 29.7% | 26.7% | 25.6% | 31.2% |
| **True absorbed current integral (As)** | 3702.1 | 3482.8 | 3233.6 | 3823.5 |
| **Predicted absorbed current integral (As)** | 3630.3 | 3272.2 | 3212.1 | 3756.7 |

The variation of battery SOC shows an acceptable prediction with respect to the telemetry data that consider the integer approximation.

As developed for the time-of-flight predictor, also for the absorbed current integral predictor a UTM application is proposed. Specifically, the proposed method can support the Path Planner task to predict the battery SOC needed to fly over a generic path and the Contingency Management task to evaluate the remaining battery level that can be used if unexpected events occur.

A scaled package delivery mission was designed for urban or industrial areas. The battery SOC was predicted for the whole planned path. The maximum distance that the UAS can reach from strategical points that belong to the planned path can be predicted. So, the battery discharge predictor can be used to assess the area that the UAS can reach with the remaining battery level.

Considering the proposed application, the first mission waypoint is indicated as WP1 and the last mission waypoint as $WP_{end}$ as shown in Fig. 30. In the simulated environment the UAS carries small packages in an urban environment to drop off in the planned waypoints. The blue rectangle indicates the warehouse location where the UAS takes off and lands according to the nominal mission. The grey rectangles are fixed obstacles, i.e. houses, shops, buildings. The green circles are safe areas where the UAS could eventually land, such as the so-called vertiports, that are defined as Safe-Landing Areas (SLAs). Local weather forecasts or local weather stations can be used to evaluate the wind conditions, i.e. intensity and direction. The simulated wind vector is aligned in direction 240deg with intensity of 2.0m/s. The involved Beaufort category is 2.

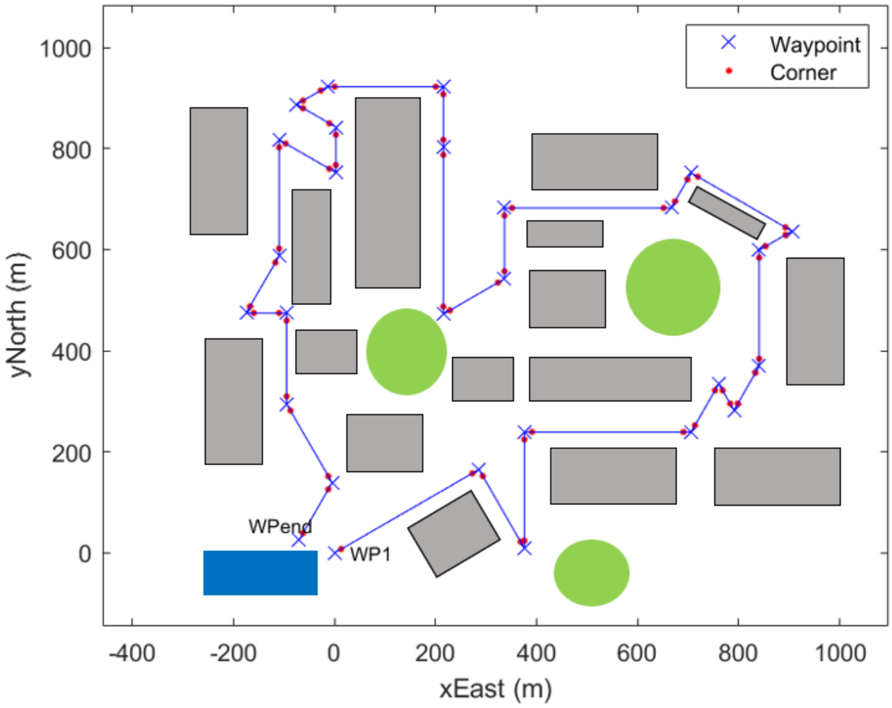

Fig. 30. Designed path for scaled package delivery mission in a simulated urban environment. The nominal path is indicated with blue line, the package delivery warehouse with blue rectangle, the fixed obstacles, i.e. buildings, with grey rectangles, SLAs with green circles.

Several SLA were located according to a random distribution in the path surrounding area, as reported in Fig. 31 with black circles. Random points that belong to the planned path were defined as Monitoring Points (MP) with red circles and it is possible to apply the proposed battery discharge predictor in these points. Only some SLA can be reached by the UAS from the defined 13 MP, so the aim of the proposed application is predicting the SLAs that can be safely reached.

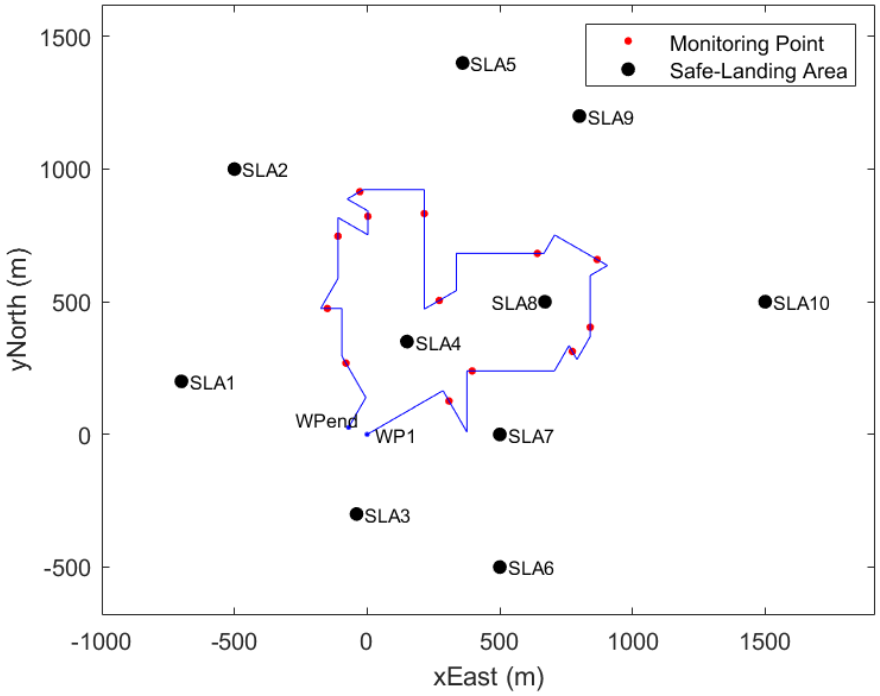

Fig. 31. Designed path for scaled package delivery mission. The nominal path is indicated with blue line, the monitoring points with red circles, the fixed obstacles, i.e. building, with grey rectangles, SLAs with black circles.

The predicted values of absorbed current integral, and battery ΔSOC at the MPs were reported in Table 25 starting the flight from the WP1 with battery SOC equals to 100%. This analysis helps to design the nominal path and the number of batteries that are needed to complete the mission.

Table 25. Predicted values of absorbed current integral and battery ΔSOC computed at the selected MPs of the scaled package delivery mission.

| | **Expected value of absorbed electric charge (As)** | **Predicted battery ΔSOC** |
|---|---|---|
| **MP1** | 609.6 | 95.0% |
| **MP2** | 1322.7 | 89.2% |
| **MP3** | 2114.3 | 82.7% |
| **MP4** | 2487.7 | 79.7% |
| **MP5** | 3084.3 | 74.8% |
| **MP6** | 3632.3 | 70.3% |
| **MP7** | 4553.5 | 62.8% |
| **MP8** | 5300.3 | 56.7% |
| **MP9** | 5935.2 | 51.5% |
| **MP10** | 6290.6 | 48.6% |
| **MP11** | 6808.5 | 44.4% |
| **MP12** | 7407.2 | 39.5% |
| **MP13** | 7906.1 | 35.4% |

Beside the proposed analysis that can be applied for Path Planning, a solution for Contingency Management is presented to support path re-planning when unexpected events occur. If the nominal path can not be completed, the UAS must land in a safe area, i.e. a SLA, that can be identified in the surrounding environment. Two conditions can be analyzed:

1) Case A - Straight Path. The UAS can execute a straight path from the current position to the closest SLA if it is flying above fixed obstacles at a safe height.
2) Case B - Path with corners. The UAS can execute a straight path from the current position to the closest SLA from the current position to the closest SLA if it must avoid low level obstacles.

The aim of the analysis is computing the predicted distance in both cases to evaluate the SLAs that can be reached by the UAS from a random MP. The battery ΔSOC predicted after reaching each MP was computed considering a safe threshold and it is named $\Delta SOC_{MP,th}$. This value is the battery ΔSOC needs to reach a battery level threshold of 30% flying from the current MP. The threshold of 30% is a typical value [105] [106] that must be saved to allow a safe landing.

Case A solution was developed exploiting the tests conducted for T180 *standard paths*. The average value of ΔSOC per unit flown distance was computed considering the tests over straight paths and it is named $\Delta SOC_{ul,straight}$. The remaining battery ΔSOC for each MP, i.e. $\Delta SOC_{MP,th}$, was divided by the battery ΔSOC per unit flown distance to obtain the maximum distance $L_{straight}$ that the UAS can reach from the considered MP over a straight path, according to Eq. 10.

$$L_{straight} = \frac{\Delta SOC_{MP,th}}{\Delta SOC_{ul,straight}} \qquad \text{Eq. 10}$$

Case B solution was developed exploiting the tests that were conducted for paths with corners. The distance to fly from WP1 to each MP according to the planned path was computed. The battery ΔSOC per unit flown distance was computed dividing the battery ΔSOC by the traveled distance. The 70% of the flown distance was used to compute $\Delta SOC_{ul,wc}$ that represents the battery ΔSOC per unit flown distance in the worst-case. The worst-case includes the conservative condition in which the path with corners that must be flown to reach the identified SLA is strongly different with respect to the travelled path. The remaining battery ΔSOC for each MP, i.e. $\Delta SOC_{MP,th}$, was divided by the battery ΔSOC per unit flown distance to obtain the maximum distance $L_{wc}$ that the UAS can reach from the considered MP over a path with corners, according to Eq. 11.

$$L_{wc} = \frac{\Delta SOC_{MP,th}}{\Delta SOC_{ul,wc}} \qquad \text{Eq. 11}$$

Considering the planned path and the MPs reported in Fig. 31, the comparison between the maximum distances $L_{straight}$ and $L_{wc}$ is analyzed in Fig. 32. The maximum reachable distance $L_{straight}$ is larger than $L_{wc}$ for each MP because the in latter case the UAS must execute turning maneuvers to avoid obstacles to reach the SLA.

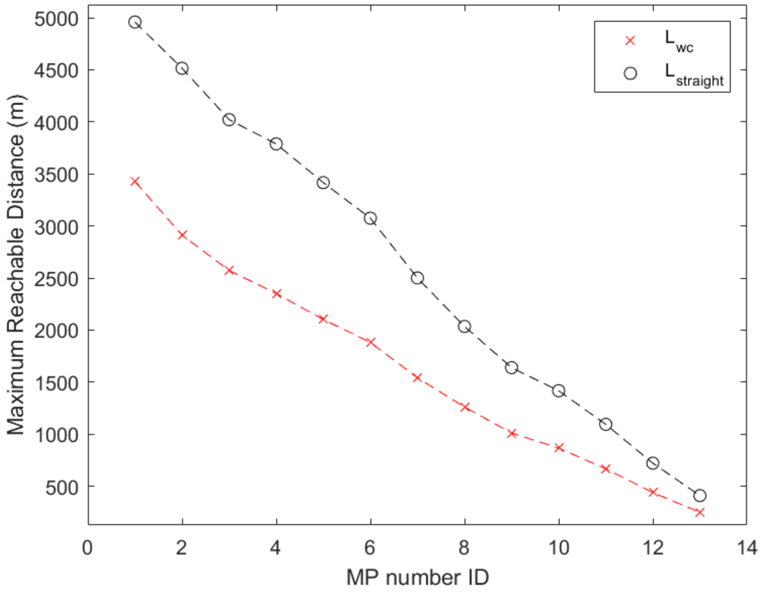

Fig. 32. Comparison between the maximum distance that can be reached by the UAS with the remaining ΔSOC by flying over a straight path $L_{straight}$ or a path with corners $L_{wc}$.

The available SLAs in the proximity of the planned path are identified during the strategic phase. If an unexpected event occurs when the UAS is flying over a generic MP, the maximum reachable distances, i.e. $L_{straight}$ and $L_{wc}$, can be used to evaluate if the UAS can reach a SLA with the remaining battery level considering a straight path, i.e. Case A, or a path with corners, i.e. Case B. In the proposed application, the distances $L_{straight}$ and $L_{wc}$ represent the radius of two circles centered at each MP. If a SLA is within one of the two circles, it means that the UAS can reach the SLA with the remaining battery level. This concept is similar to the concept of Point of No Return (PNR) for aircraft, in which the pilot knows that if an unexpected even occurs he can not land at the departure airport after the PNR, but he must head towards the alternate airport.

Table 26 reports the topology matrix for each selected MP. It shows the list of SLAs that can be reached by the UAS considering the computed distances $L_{straight}$ and $L_{wc}$.

Table 26. Topology matrix of SLAs that can be reached by the UAS in Case A and Case B scenarios according to Eq. 10 and Eq. 11. The symbol "Y" indicates the SLAs that can be reached from the MP. The bold symbol "N" indicates the SLAs that can not be reached from the MP.

| | Reachable SLAs from selected MPs (Case A / Case B) | | | | | | | | | |
|---|---|---|---|---|---|---|---|---|---|---|
| | **SLA1** | **SLA2** | **SLA3** | **SLA4** | **SLA5** | **SLA6** | **SLA7** | **SLA8** | **SLA9** | **SLA10** |
| **MP1** | Y / Y | Y / Y | Y / Y | Y / Y | Y / Y | Y / Y | Y / Y | Y / Y | Y / Y | Y / Y |
| **MP2** | Y / Y | Y / Y | Y / Y | Y / Y | Y / Y | Y / Y | Y / Y | Y / Y | Y / Y | Y / Y |
| **MP3** | Y / Y | Y / Y | Y / Y | Y / Y | Y / Y | Y / Y | Y / Y | Y / Y | Y / Y | Y / Y |
| **MP4** | Y / Y | Y / Y | Y / Y | Y / Y | Y / Y | Y / Y | Y / Y | Y / Y | Y / Y | Y / Y |
| **MP5** | Y / Y | Y / Y | Y / Y | Y / Y | Y / Y | Y / Y | Y / Y | Y / Y | Y / Y | Y / Y |
| **MP6** | Y / Y | Y / Y | Y / Y | Y / Y | Y / Y | Y / Y | Y / Y | Y / Y | Y / Y | Y / Y |
| **MP7** | Y / Y | Y / Y | Y / Y | Y / Y | Y / Y | Y / Y | Y / Y | Y / Y | Y / Y | Y / Y |
| **MP8** | Y / Y | Y / Y | Y / Y | Y / Y | Y / Y | Y / **N** | Y / Y | Y / Y | Y / Y | Y / **N** |
| **MP9** | Y / Y | Y / Y | Y / **N** | Y / Y | Y / Y | Y / **N** | Y / **N** | Y / Y | Y / Y | Y / **N** |
| **MP10** | Y / **N** | Y / Y | Y / **N** | Y / Y | Y / Y | Y / **N** | Y / **N** | Y / Y | Y / **N** | Y / **N** |
| **MP11** | Y / **N** | Y / Y | Y / **N** | Y / Y | Y / **N** | **N / N** | Y / **N** | Y / **N** | Y / **N** | **N / N** |
| **MP12** | Y / **N** | Y / **N** | Y / **N** | Y / Y | **N / N** | **N / N** | Y / **N** | Y / **N** | **N / N** | **N / N** |
| **MP13** | Y / **N** | **N / N** | Y / **N** | Y / Y | **N / N** | **N / N** | Y / **N** | **N / N** | **N / N** | **N / N** |

In Table 26, in each column the first symbol is referred to Case A in which the UAS executes a straight path, the second symbol is referred to Case B in which the UAS executes a path with corners. In some situations, such as for the couple MP8 - SLA6, the UAS can reach the SLA6 from the MP8 only by following a straight path.

An example of determination of the available SLAs is reported in Fig. 33 for the MP13.

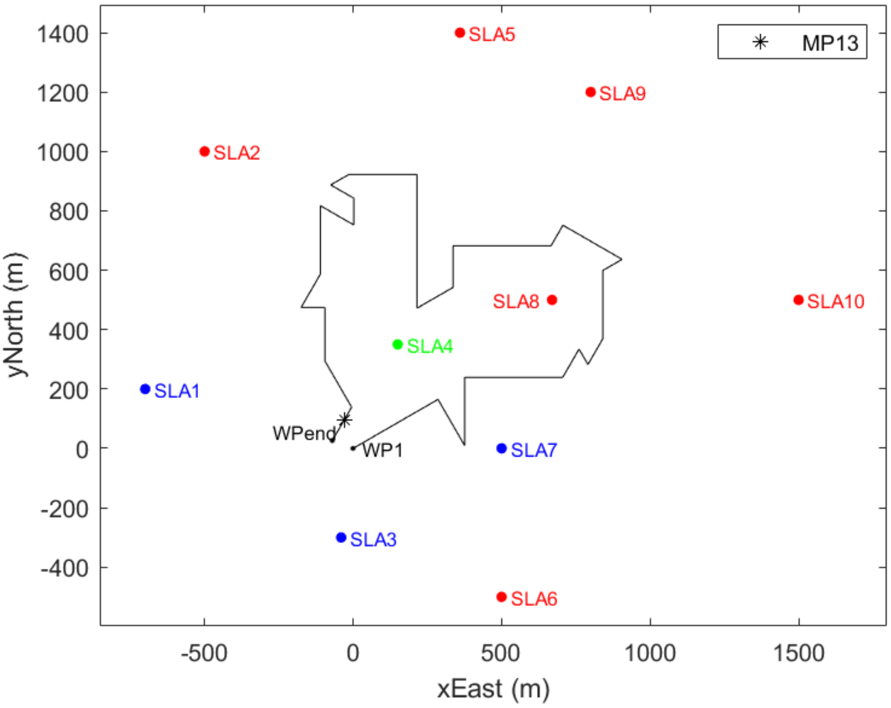

Fig. 33. Determination of the available SLAs from the MP13 that is represented by a black star. ENU reference frame centred at WP1. The SLAs indicated by red circles can not be reached, the SLA indicated by green circle can be reached in both Case A and Case B, the SLAs indicated by blue circles can only be reached in Case A, i.e. with a straight path.

If an unexpected event occurs when the UAS has reached the MP13, the UAS can not complete the planned path and a SLA must be identified. The maximum distances in Case A and Case B are respectively $L_{straight}$=410.0m and $L_{wc}$=248.9m for MP13. The SLAs indicated by red circles can not be reached, the SLA indicated by green circle can be reached in both Case A and Case B, the SLAs indicated by blue circles can only be reached in Case A, i.e. with a straight path.

# 5. Integrated Navigation with Polarimetric Camera

Accurate attitude estimation is a critical parameter that must be achieved for navigation purpose. Traditional sensors are affected by poor performance to measure the heading angle. This work proposes the adoption of a polarimetric camera, integrated in the attitude determination system, to measure the skylight polarization angle and improve the heading angle estimation. The described solution can be adopted in BRAINS configuration as *Navigation Measurements Sensor* unit to improve navigation capabilities in challenging environments.

## 5.1. Overview

The passage of Sun light through the atmosphere layers polarizes the light. The polarization pattern depends on the relative position of Sun and Observer, so specific directions of the Sun polarization pattern can be used as a reference to improve the estimation of vehicle heading angle. The proposed method is bio-inspired by the animal behavior of some species. Several animals follow the Sun light polarization for orientation aims, such as Monarch butterflies, desert ants and locusts, field crickets [107] [108] [109].

Several studies are interested in using this capability to improve navigation performance. An array of 128x128 pixels divided in three sectors was used in [110] to exploit the polarization data thanks to a metal grid micro-polarizer. The sectors measure the intensity and the polarized intensity according to different directions. If the light beam changes direction, the Degree Of Polarization (DOP) and the Fresnel Polarization Ratio (FPR) change values, as a compass. If the polarizer angle is 0°, the value of FPR reaches a maximum peak, if the polarizer angle is 90°, the value of FPR reaches a minimum.

A multi-sensor navigation system is described in [111] to compute the orientation of a vehicle in an urban environment. The integrated system includes a monocular camera, an inertial system, and a light polarization sensor. The Kalman filter integrates the data coming from all the sensors to estimate the vehicle position and orientation, achieving a Root Mean Square Error (RMSE) of 2.04m for position and 0.84deg for orientation.

A light polarization measurement system was developed in [112]. It includes 4 Charge-Coupled Device (CCD) cameras in order to acquire images with four polarization angles. Considering the Rayleigh model for skylight, the 80% of the Angle of Polarization (AOP) deviations are lower than 2deg.

The robustness of Angle Of Polarization (AOP) measure was assessed in different weather conditions in [113]. A polarimeter based on Liquid Crystal Variable Retarders (LCVR) was adopted and the polarization pattern in different cloudy conditions was evaluated. Then, a navigation method based on the solar meridian identification was described.

The polarization pattern was compared in [114] in different weather conditions and the solar meridian was computed by using a CCD camera with a fish-eye lens. The DOP was used to assess the accuracy of the AOP measures. The maximum error achieved by the method to estimate the solar meridian orientation is lower than 0.5deg even in cloudy conditions.

## 5.2. Methodology

A low-cost IMU can be integrated with a Sun light polarization camera to improve the heading angle measurements. Specifically, the poor performance of traditional magnetometers that are included in an Attitude and Heading Reference System (AHRS) can be improved by using a polarimetric camera. The methodology and test equipment that was used to integrate the polarimetric camera are presented in [115].

The reference frames that were used during the method development must be defined. The camera location is assumed to be at the observer position named $O$. The ENU reference frame is centered at the observer position $O$. A sphere with a unit-radius was considered with the origin in $O$ and it is represented in Fig. 34. The red line vector is aligned with the Sun direction, the black vector is aligned with the observation direction. Point S is the intersection between the Sun direction and the unit-radius sphere, point P is the intersection between the observing direction and the unit-radius sphere. The coordinates of each point that belongs to the unit-radius sphere can be expressed by the spherical coordinates:

- φ the clockwise angle from the North direction and the point projection on the horizontal plane;
- θ the clockwise angle from the Up direction of ENU reference frame and the vector that passes through the point.

According to the mentioned definitions, the points reported in Fig. 34 have coordinates $P(\varphi_P, \theta_P)$ and $S(\varphi_S, \theta_S)$. The angle γ is defined as the angle between the observation unit vector and the Sun unit vector.

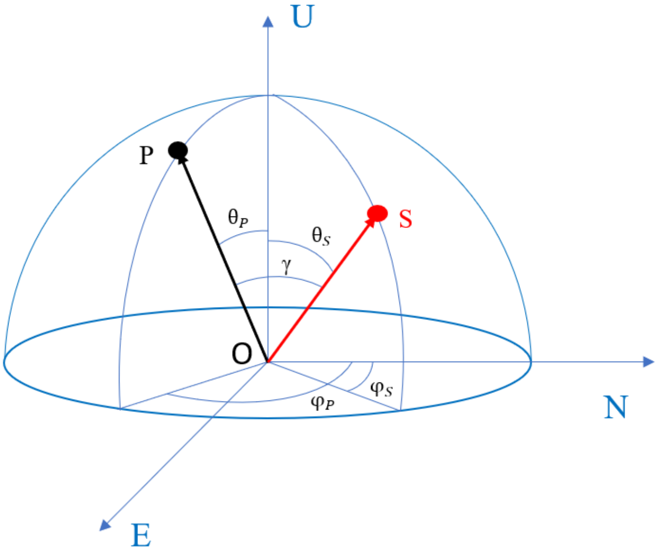

Fig. 34. ENU reference frame centered at position of the observer O. The red vector points towards the Sun direction and S is the intersection between the Sun direction and the unit-radius sphere. The black vector points towards the observing direction and P is the intersection between the observing direction and the unit-radius sphere.

The origin of the camera reference frame is positioned at the center of the device. The first axis towards the right side, the second axis towards the downside, and the third axis is aligned with the camera boresight. The observation unit vector of a generic point in the camera reference frame can be obtained thanks to the coordinates of that point in the image plane in pixels according to the Pinhole Camera model. The spherical coordinates in the ENU reference frame can be computed from the knowledge of the camera pointing.

The single-scattering Rayleigh model was exploited to compute the theoretical DOP according to Eq. 12. The symbol σ represents the maximum value of DOP in range [0, 1]. In the presented study, the ideal value $\sigma=1$ was considered.

$$DOP = \sigma \, \frac{(\sin(\gamma))^2}{1+(\cos(\gamma))^2} \qquad \text{Eq. 12}$$

The AOP was computed estimating the inverse tangent of the ratio between Eq. 13 and Eq. 14. The obtained AOP value is in range [-90°, 90°] [116].

$$\sin(AOP) = \frac{\sin(\theta_P)\cos(\theta_S) - \cos(\varphi_S - \varphi_P)\cos(\theta_P)\sin(\theta_S)}{\sin(\gamma)} \qquad \text{Eq. 13}$$

$$\cos(AOP) = \frac{\sin(\varphi_S - \varphi_P)}{\sin(\gamma)} \sin(\theta_S) \qquad \text{Eq. 14}$$

The reference object that can be used for navigation purpose is the position of the Sun meridian or anti-meridian because the identification of this reference is possible detecting the discontinuity in the AOP pattern [116]. If the Sun position and the observer position are known, the AOP discontinuity can be identified and compared with the AOP discontinuity identified in the acquired camera images. The comparison allows to estimate the heading angle of the observation direction.

The test equipment that was used to acquire the images is shown in Fig. 35. It includes:

1) The camera model FLIR® Blackfly S BFS-PGE-51S5P-C [53] was used to acquire row images that can be processed to extract light polarization data. This monochromatic camera involves a Polarization Image sensor IMX250MZR manufactured by Sony® with polarization filters. The filters are installed on the on-chip lens layer in a fixed 2x2 pixel pattern. Four polarization angles are considered: 0deg, 45deg, 90deg, and 135deg. The resolution of the detector is 2448x2048 pixels, but the polarimetric images have 1224x1024 pixels resolution because the four polarization states must be considered. A lens with a focal length of 8 mm was used.
2) The SensorTile™ [117] manufactured by STMicroelectronics was used to acquire data from gyroscope, magnetometer, and accelerometer. The small size of 13.5x13.5mm allows to develop compact on-board system.
3) The processing board STM32F401RE [41] with a microcontroller was used to acquire data through a Serial Peripherical Interface bus from used sensors.
4) The Graphical User Interface (GUI) SpinView® by FLIR® software Spinnaker SDK® was used to acquire raw images from the camera. The camera settings allow to save a raw image and a processed image according to the parameter that was

selected, such as Degree Of Linear Polarization (DOLP), Angle Of Linear Polarization (AOLP), Stokes parameters.

The camera and the inertial unit were installed on a rigid plate. The attitude of the plate can be changed thanks to the tripod hinges.

Fig. 35. Test equipment used for images acquisition.

A method to process the 8-bits raw image was developed to display the AOLP pattern in the 1224x1024 pixels image. Considering the full resolution raw image, filter patterns were identified with four pixels arranged in a square shape. Four images with resolution 1224x1024 pixels were obtained grouping the pixels that collect the light with the same polarization angle. The light intensity for the four images is respectively named I0, I45, I90, and I135 according to the polarization angle.

Considering the four obtained images, the linear Stokes parameters defined as S0, S1, and S2 were computed by using Eq. 15, Eq. 16, and Eq. 17. Thanks to the combination of the four images, three 1224x1024 pixels images were obtained according to the Stokes parameters pattern. At the end, DOLP and AOLP were obtained exploiting the linear Stokes parameters by using Eq. 18 and Eq. 19 [118] [119].

$$S0 = I0 + I90 \qquad \text{Eq. 15}$$

$$S1 = I0 - I90 \qquad \text{Eq. 16}$$

$$S2 = I45 - I135 \qquad \text{Eq. 17}$$

$$DOLP = \frac{\sqrt{S1^2 + S2^2}}{S0} \qquad \text{Eq. 18}$$

$$AOLP = \frac{1}{2}\arctan\left(\frac{S2}{S1}\right) \qquad \text{Eq. 19}$$

After the acquisition of raw images, the MATLAB® software was exploited to process each image obtaining a 1224x1024 pixels image that displays the AOLP patter. The position of the Sun meridian/anti-meridian was computed in the image reference frame and then reported in the camera reference frame.

The Sun ephemeris can be computed because the acquisition GPS time -in format day, month, year, hour, minutes, and seconds- is reported for each image and the GPS observation position was acquired. So, the nominal position of the Sun meridian/anti-meridian can be estimated and compared with the measured position. This comparison allows to compute the heading angle of the observation direction.

Several tests were performed to assess the method by acquiring both Sun meridian and anti-meridian. The indication about the observing object, i.e. if the camera is observing the meridian or the anti-meridian, must be considered during the procedure, otherwise an error of 180deg can occur.

The tests were conducted in the University campus courtyard in Naples city. The Sun azimuth $\varphi_S$ and elevation $\lambda_S$ that is the complementary of co-elevation $\theta_S$ were computed according to [120] by knowing the observation location and the acquisition time. The Sun direction can be computed in the ENU reference frame. The inertial unit was used to estimate the attitude angles that are named roll α, pitch β.

The heading angle that is measured by the proposed method is referred to the true North direction, so a magnetic deviation of 3.80deg must be considered for Naples location according to the International Geomagnetic Reference Field (IGRF-13) [121] [122].

The heading angle can be estimated comparing the Sun direction in the ENU reference frame and the unit vector towards the Sun meridian/anti-meridian in the camera reference frame.

Specific techniques, such as the use of Radon transform, can support the identification of the Sun meridian/anti-meridian in the image reference frame avoiding the confusion with other objects, such as trees, light poles.

## 5.3. Method Tests and Results

An example of the proposed method to compute the heading angle exploiting a Sun light polarization camera is discussed. The main parameters that were set during the described test are reported in Table 27. Date and time data were obtained by the image timestamp, the location by the GPS receiver, the roll and pitch angles related to the camera attitude by the inertial unit. Considering the small values of roll and pitch angles, the camera plane that includes the first and third axes was almost parallel to the local horizontal plane.

Table 27. Parameters used for local test.

| **Acquisition Parameter** | **Acquired value** |
|---|---|
| Date (dd/mm/yyyy) | 30/04/2021 |
| Local Time (h:min:s) | 09:32:06 |
| Latitude (deg) | 40.83694 |
| Longitude (deg) | 14.30667 |
| $\alpha$ (deg) | 1.3 |
| $\beta$ (deg) | 12.6 |

The Sun azimuth and elevation were computed for the reported position and date thanks to [120] and are reported in Table 28.

Table 28. Sun position for local test.

| **Sun position** | **Value (deg)** |
|---|---|
| $\varphi_S$ | 104.1 |
| $\lambda_S$ | 38.4 |

According to the Rayleigh model, the DOP and AOP distributions over a unit-radius sphere centered at the observer location were computed by using Eq. 12 - Eq. 14 varying azimuth and the co-elevation, as displayed in Fig. 36.

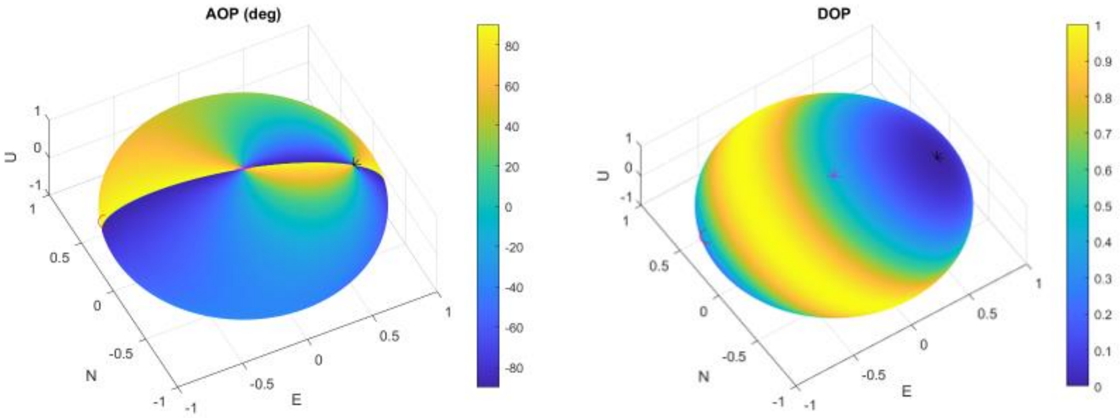

(a) (b)

Fig. 36. Rayleigh model computed for the assigned test parameters. ENU reference frame centered at observer location. The red circle is the intersection between the unit-radius sphere and the observation direction. The black star is the intersection between the unit-radius sphere and the Sun direction, the red star is the intersection between the unit-radius sphere and the nadir direction. a) Simulated AOP pattern over the unit-radius sphere. b) Simulated DOP pattern over the unit-radius sphere.

The simulated image of AOP distribution was obtained by knowing the Sun position, the observer position, and the camera specifications to compute the nominal position of the Sun anti-meridian.

The raw image acquired considering the parameters in Table 27 was processed to obtain the 1224x1024 pixels image about the AOLP distribution. The unit vector that points towards each pixel in the camera reference frame was referred to ENU reference frame with spherical coordinates. The resulting image is displayed in Fig. 37.

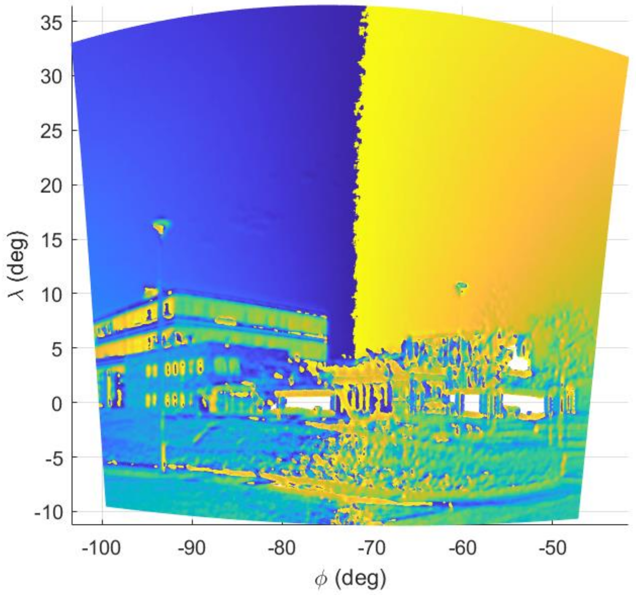

Fig. 37. AOLP distribution computed by the proposed image processing. φ (azimuth) and λ (elevation) are the spherical coordinates in the ENU reference frame centered at the observing location.

A generic pixel that belongs to the Sun anti-meridian was identified considering the AOLP value and the unit vector of that observing direction was computed in ENU reference frame and the heading angle was estimated.

The comparison between the heading angle computed by the inertial unit, i.e. $\gamma_{inertial}$, and the proposed image processing, i.e. $\gamma_{camera}$, is reported in Table 29.

Table 29. Comparison between the heading angle computed by the inertial unit and the proposed image processing.

| **Heading Angle** | **Value (deg)** |
|---|---|
| $\gamma_{inertial}$ | 283.1 |
| $\gamma_{camera}$ | 283.3 |

The results show that the difference between $\gamma_{inertial}$ and $\gamma_{camera}$ is acceptable. An integrated system can be developed to use the heading angle computed by the proposed method to reduce the heading error drift of the magnetometer or to support the navigation in GNSS challenging environments, such as in the so-called urban canyon. Moreover, this technique can also be exploited by Unmanned Underwater Systems to navigate at few meters below the sea level without the need to often re-emerge.

# 6. Design of Swarm Configurations

UAS swarm configurations allow to achieve high performance in terms of robustness, autonomy, reliability, self-reconfigurability. Swarming capabilities must be analyzed to develop proper case-studies that can be supported by the UTM services. Specifically, the development of two solutions that exploit swarm capabilities for different *Payload* unit operations is presented. The first application involves a UAS swarm equipped with cameras to monitor human biomedical parameters. The second application involves a UAS swarm equipped with corner reflectors to obscure radar detection for military applications.

## 6.1. Overview

The rapid improvement of UAS hardware and software technologies in terms of localization, communications, decision making, collision avoidance, allowed the development of efficient configurations that involves several UASs arranged in swarms.

In swarms, the workload of each involved UAS is distributed among all units, increasing the system robustness and the payload effectiveness. Thanks to the deployment of UAS swarms, the mission coverage area can be extended -for example- for surveillance and mapping operations, but also communications networks can benefit from the distributed communication relay [123] [124]. In military applications, UAS swarms are adopted to protect critical targets [125]. So, the development of UTM must include adequate rules and solutions to manage swarms of UASs. The definition of swarm configurations allows to define proper geometries that can be adopted for different types of mission, providing case-studies for UTM services that must assure proper safety levels.

## 6.2. Swarms for Emergency Management

An example of advanced processing of *Payload unit* data exploiting swarm capability is reported for an emergency management application, such as during the COVID-19 pandemic, that was developed in the project funded by Regione Campania CUP B24E19000250007 [126].

### 6.2.1. Overview

The COVID-19 pandemic had a strong impact of worldwide population. The use of advanced UASs can support ground operations of institutional authorities to reduce the virus spread. The use of UASs allow to map large regions, such as parks, urban environments reducing the time consumption and the risk of people involved in the pandemic fight [127] [128] [129]. Advanced processing of UAS payload data can support emergency situations where a rapid time response is needed, for example during the COVID-19 pandemic to limit the virus spread, such as the study developed to identify the services for equipment delivery [130].

### 6.2.2. Monitoring, Transport, and Spray Tasks

A distributed UAS swarm was designed to achieve specific tasks for UAS employment in emergency management: monitoring of biomedical parameters, transport of goods, and spray diffusion, as reported in Fig. 38.

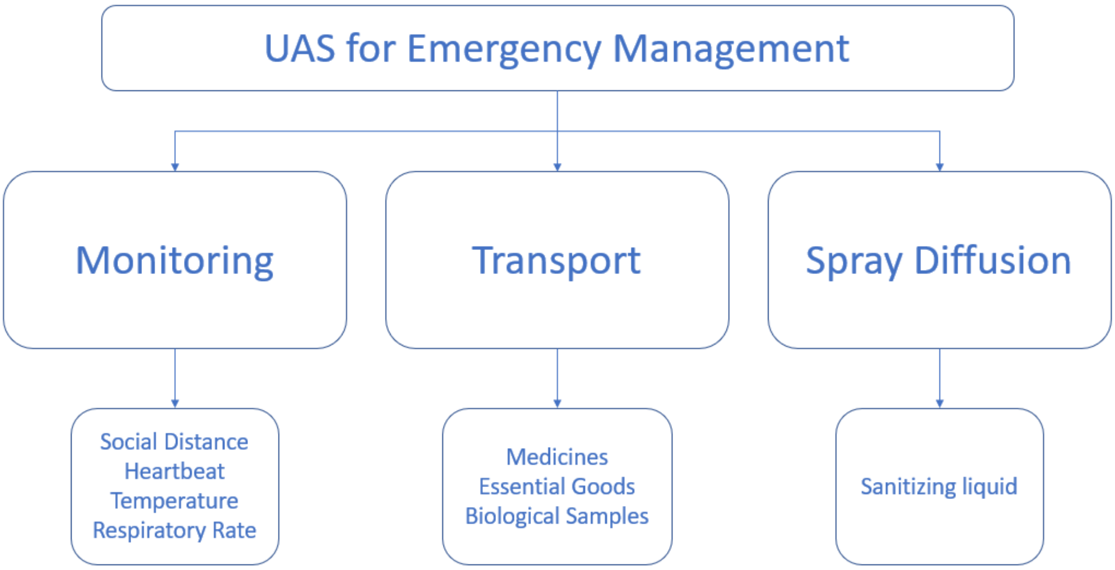

Fig. 38. Main tasks for emergency management by using UASs.

The UAS swarm was designed to identify number and type of swarm units that must be included to achieve the mentioned tasks with proper accuracy and integrity levels.

- Monitoring Task. It allows to identify crowded areas where the social distancing is violated, and people show altered biomedical parameters. Several images can be acquired by a swarm of UASs so that the relative distances between observed targets can be estimated, as well as biomedical parameters, such as skin temperature, heartbeat, and respiratory [131] [132] [133]. Advanced thermal camera, and high-resolution visible band cameras with zoom capabilities can be installed on-board UASs and the target data can be processed by using proper algorithms. An alert signal must be generated by the swarm if one or more of the mentioned parameters assume higher values with respect to a set threshold. When the alarm is generated, ground patrols can intervene.

- Transport Task. It can be developed by using a swarm of heavy-lift UASs that carry packages with medicines, essential goods, and biological samples and one or more UASs that monitor the surrounding area to identify possible risks or obstacles [134] [135] [136]. A thermal camera must be installed on-board the monitoring UASs to identify crowds of uninvolved people that must not be overflown by heavy-lift UASs. Small packages can be carried by heavy-lift UASs for long missions, such as biological samples for rapid laboratory analysis, or heavy packages for short high-risk missions, such as the transport of essential goods to people affected by the virus, reducing the exposure time of health workers.
- Spray Diffusion Task. It can be achieved by using one or more monitoring UASs and one heavy-lift UAS equipped with a liquid tank and a spraying system. The presence of uninvolved people is detected by the monitoring UASs that generate an alarm to drive away the crowds and stop the spraying mission. Then, the UAS with the liquid tank spreads the sanitizing liquid in the area of interest. An example of UAS that can be used for this type of mission is the UAS used in agricultural environment [137] [138], because it is equipped with tank and proper nozzles.

The characteristics of UAS swarms defined to achieve the proposed tasks, i.e. monitoring, transport and spray diffusion, are summarized in Table 30.

Table 30. Characteristics of UAS swarms defined for monitoring, transport, and spray diffusion tasks.

| **Task** | **UAS Swarm** |
|---|---|
| Monitoring | Two UASs equipped with visible band cameras and at least one UAS equipped with thermal camera to estimate critical human biomedical parameters. |
| Transport | At least one UAS equipped with thermal camera for monitoring purposes. One heavy-lift UAS for package delivery. |
| Spray Diffusion | At least one UAS equipped with thermal camera to monitor the presence of uninvolved people. One UAS equipped with large tank and nozzles for sanitizing liquid diffusion. |

### 6.2.3. Monitoring Task Overview

To monitor the human healthy state, biomedical parameters must be evaluated, such as heartbeat, temperature, respiratory rate, oxygen saturation. During the discussion, the word *target* is referred to a person that must be monitored to measure his biomedical parameters. The systems used to achieve the measures of biomedical parameters must provide accurate results in different conditions. Several studies were analyzed to identify the main technologies that can be used to measure human biomedical parameters:

- Stereoscopy techniques. Several images of two or more targets can be acquired by visible band cameras considering different points of view. The relative distance between targets can be estimated by using stereoscopy-based approach [139] [140] [141].
- Thermal cameras. Infrared thermometers are the medical equipment that is used to measure the target temperature. However, thermal data about the target skin temperature can be obtained by using data fusion techniques for images acquired

by cameras with different performance. Some works reported strategies to measure the heartbeat and the breathing waveform from thermal image processing [142] [143]. The measure of target skin temperature can be used as preliminary scanning, for example to manage the access to indoor areas. Then, targets that present high values of skin temperature must be monitored by using medical devices.

- Photoplethysmography (PPG) techniques. Cameras can acquire short videos to detect the radiation that is reflected by the target skin. So, some biomedical parameters can be estimated, such as respiration rate and heartbeat by measuring the blood volume. Cameras that exploit green, red, and near-infrared light bands are often used because the longer wavelength can penetrate the skin [144] [145]. In addition, specific human parts, such as nostrils and forehead, can be tracked by using proper ML algorithms thanks to the identification of a Region Of Interest (ROI).

  The traditional use of PPG techniques is related to wearable sensors. The device is placed on a finger. A beam is emitted from a LED, and it penetrates the skin. The variations of emitted light are measured by a photodiode that is on the opposite side of the finger. The amount of detected light is related to the pulse condition, because when the volume increases, more light is absorbed. However, some works reported the use of remote PPG [146] [147] [148] [149], also by using techniques to reduce the error related to the target motion [150].

  The evolution of PPG is related to Imaging Photoplethysmography (IPPG), where the light variations are detected by a camera. The study reported in [151] monitors the glucose level of blood. The works [152] [153] [154] [155] measure the heart rate. This technique can also be used to detect Atrial Fibrillation [156] and to obtain data about target stress state [157].
- Radar-based techniques. Respiration rate and heartbeat can be measured by exploiting radar-based systems, such as Continuous Wave, Frequency-Modulated Continuous Wave, Doppler radars, Forward Scatter, Ultra-Wideband Pulse-Based [158] [159] [160] [161] [162] [163]. The use of radar technology involves the proper selection of emitted power and frequency to protect people and devices in the surrounding areas according to local regulation.

- Acoustic Analysis. The detection of common symptoms can help the identification of human diseases, such as COVID-19. Identification techniques of human and animal cough and sneeze were developed in several works, such as [164] [165], also performing acoustic analysis [166]. A thermal camera can be used to identify the number of targets and a microphone to detect cough and sneeze symptoms. Filtering is the challenge task to avoid external sounds. ML techniques can also be used thanks to a database of sounds to identify cough and sneeze sounds [167].

The use of UASs can support the widespread measurement of biomedical parameters in emergency scenarios, such as during the COVID-19 pandemic. Monitoring biomedical parameters, such as respiratory rates and heartbeat, and social distancing by using UASs helps to reduce the virus spread covering large and crowded areas in shorter time. Compact and lightweight systems can be installed on-board UASs to provide skin temperature, heartbeat, and respiratory rate [168] according to the mentioned techniques on wide areas. A proper benchmark must be select to compare the remote measures obtained by using UAS payload systems with data obtained by using medical devices, such as Holter monitor, infrared thermometers, pulse oximeters, respiratory belt transducers.

Also, the UAS position must be estimated with high accuracy level to allow medical personnel and/or institutional authorities to reach the identified target with altered biomedical parameters, reducing time and cost. The payload systems must be identified considering proper performance in different light conditions and reducing the errors related to the target motion. Hardware selection is a critical parameter to identify the needed equipment according to size, weight, data-rate requirements. The remote measures can be used to perform accurate analysis at few meters distance with non-invasive techniques.

### 6.2.4. Test of Monitoring Swarm and Results

A swarm of UASs was deployed and used to acquire data about human targets. The results presented in [169] describe the use of cameras installed on-board a UAS to measure three parameters, as reported in Fig. 39:

- Social distancing. Two UASs were equipped with visible band cameras. Image processing techniques based on stereo vision paradigm with cameras that point towards same region, were applied to compute the distance between the two identified targets. Path planning was a critical phase to realize an efficient camera pointing during the flight tests.
- Skin temperature. A UAS was equipped with a thermal camera. The target skin temperature can be easily evaluated by the UAS camera. If the temperature is higher than a set threshold, an alarm is generated. A proper threshold can be selected performing several tests and camera tuning procedures, especially if the camera is non-radiometric.
- Photoplethysmography signal. Video processing algorithms can be exploited to estimate the PPG signal from a short video acquired by a visible band camera that was installed on-board the UAS. The identified frequency band is at 0.65-4 Hz that is related to 40-240 beats per minutes for human heartbeat. The ROI must be selected considering that the target could wear a protective face mask and it must be followed during the overall video duration. The forehead area was identified as ROI for the reported test.

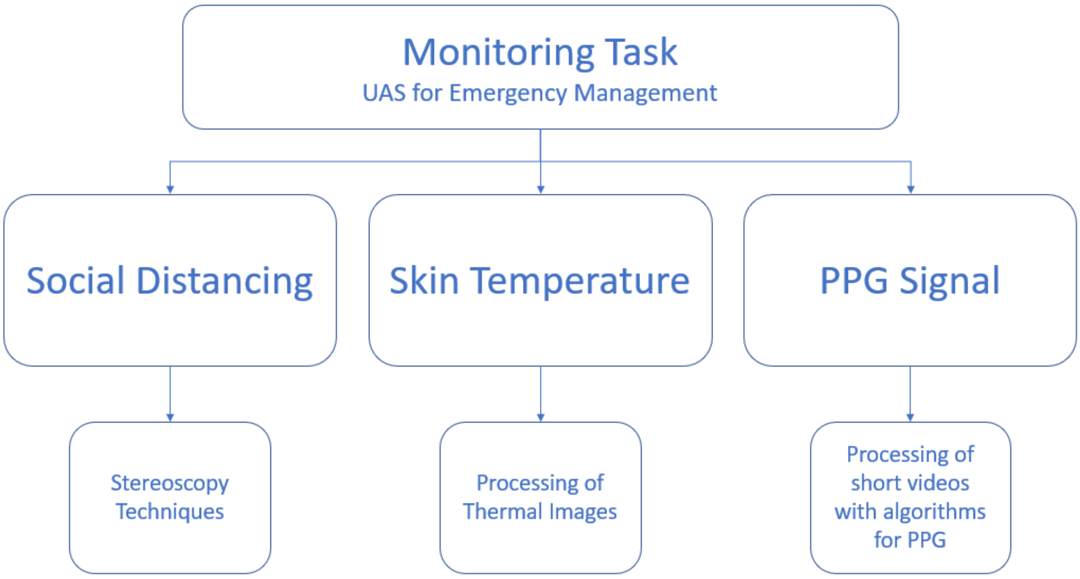

Fig. 39. Monitoring task for emergency management by using UASs.

Among the tasks, the social distancing task was developed as possible case-study that was tested to be included in BRAINS configuration. To compute the relative position between the targets, the position of the two targets was computed in the image reference frame, then, it is possible to compute the distance between the UAS and each target, and at the end the distance between targets can be computed in the local reference frame. Thanks to the proposed technique, crowded areas where the social distancing is not applied can be identified. In this method, the estimation of UAS attitude and position is the main challenge because the accuracy of these data affects the results.

The UAS swarm involves at least two UASs equipped with visible band cameras. For simplicity, to test the method two commercial UASs model Mavic 2 Enterprise® [78] were used. During the flight tests the UASs performed the planned paths in automatic mode considering the sequence of waypoints. Each waypoint was located along the radial direction with respect to the targets. The distance between each target and the UAS is the same. When the UAS reaches a waypoint, the camera acquires five images. Two human targets were located at fixed positions in the same region. A measuring tape was used to compute the relative distance between the targets and a colored label was applied on-ground to fix the positions. The face region of each target was identified as ROI.

After the flight tests, the post-processing phase exploited the MATLAB® Computer Vision Toolbox™ for calibration. The toolbox allows to calibrate both single and stereo cameras obtaining the intrinsic and extrinsic parameters.

The local reference frame North, East, Down (NED) reference frame centered at position of the first target, i.e. T1, was considered to compute the absolute involved distances. The UAS position was acquired from the telemetry data, and it is expressed in terms of latitude, longitude, and AGL height. The UAS position in NED reference frame was computed by exploiting the WGS84 World Geodetic Model.

The first UAS starts the mission flying over the marked target positions in hoovering to acquire and save in the telemetry file the GPS position. Then, both UASs start the planned mission along radial directions meanwhile the targets are fixed on the marked positions.

According to the UAS navigation specifications [78] about the position accuracy hoovering in GPS mode, the horizontal hovering accuracy is 1.5m and the vertical hovering accuracy is 0.5m. However, the error on attitude, i.e. the uncertainty on roll, pitch, and yaw angles.

An example of processed results after a flight test is reported in Fig. 40. The UAS positions are respectively named D1 and D2. The blue circles represent the UASs position in NED reference frame. The red stylized camera shows the camera pointing. The black circle identifies the true position of the first and the second target, i.e. T1 and T2, according to the telemetry data reported in NED reference frame. The red circles represent the estimated target positions, i.e. and the red stars represent the target positions, i.e. $\overline{\mathrm{T1}}$ and $\overline{\mathrm{T2}}$, computed by using the presented method.

The reported example involves a percent error of about 5% evaluating the difference between the true and the estimated distance. The whole error also involves the height error that is not visible in Fig. 40 but it must be considered in the 3D geometry.

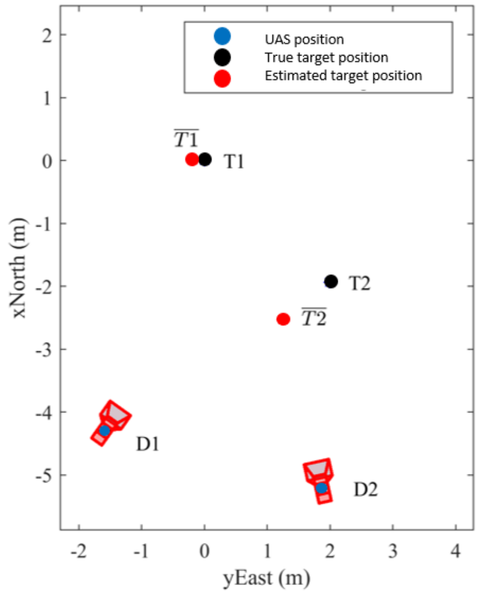

Fig. 40. Example of post-process results. The blue circle is referred to the UAS position. The red camera shows the camera pointing direction. The black circle identifies the true target position, and the red circle the estimated target position. NED reference frame centered at the true position of the first target.

The direction of the Line-Of-Sight (LOS) from the camera installed on-board the UAS to each target is strongly affected by the UAS attitude and position accuracy that increases the error on the relative distance between the targets. Advanced systems can be used to improve the position and attitude accuracy, such as the use of a Real-Time Kinematic positioning (RTK) station or advanced image processing techniques that can also be used to select the best UAS swarm configuration to reduce the relative distance error.

## 6.3. Radar Detection Properties of Swarms

The solution proposed in this work aims at identifying the geometry of UAS swarm equipped with Corner Reflectors (CR) that better electromagnetically covers a target blinding the radar. The study of UAS radiometric properties is interesting for military applications but also for civil applications about UTM procedures when swarming operations will be allowed.

### 6.3.1. Overview

Several projects were developed in different countries to use UAS swarms for manned aircraft self-protection. US Military Force developed the Perdix Program [170] to test several 3D printed micro-UASs that were released from F-16 fighter. The Defense Advanced Research Projects Agency (DARPA) carried out the Gremlins Program [171] for Close Air Support, and Intelligence, Surveillance, and Recognition operations. Leonardo s.p.a. designed and tested decoys with a Digital Radio Frequency Memory during the BriteCloud Project [172] to copy the radar pulses. Raytheon developed Miniature Air Launched decoys [173] that provide jamming capabilities. DefendTex deploys the miniaturized Drone40 systems [174] with encrypted data-link and about 1hr autonomy.

### 6.3.2. Methodology

A swarm of multi-rotor UASs was designed and tested to obscure a target by ground-based radar detection. The results are described in [175]. The UASs that are included in the swarm are called decoy-UASs, the target that must be protected is called target-UAS. The test equipment is showed in Fig. 41. The SiRad Easy$^{®}$ Evaluation Kit [176] was used and it includes a Frequency Modulated Continuous Wave (FMCW) radar with a 24GHz frontend. The Web Graphic User Interface (WebGUI) for SiRad Easy® allowed to estimate the distances where the peaks of targets are detected according to the radar echo. The magnitude of the radar echo in dB is called M.

To obtain a larger Radar Cross Section (RCS), a trihedral CR was installed as *Payload unit* on-board the decoy-UASs. The CRs were 3D printed in Polylactic Acid (PLA) material and covered by an aluminum layer. An example of decoy-UAS equipped with CRs is shown in Fig. 42.

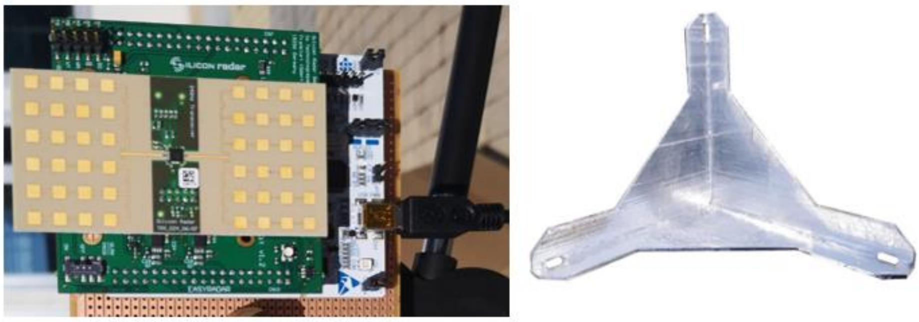

a) b)

Fig. 41. Test equipment. a) Radar manufactured by Silicon Radar®. b) Corner reflector installed on-board the decoy-UASs.

Fig. 42. Example of decoy-UAS during the corner reflector installation.

During the study, it was assumed that the target-UAS was protected thanks to the UAS swarm if the percent ratio between the magnitude of the peak with the target-UAS covered by the decoy-UASs and the magnitude of the peak with the stand-alone target-UAS is less than 50%.

### 6.3.3. Flight Tests and Results

Several ground and flight tests were performed to identify the best geometry of decoy-UASs that achieves the mission. The tests are summarized in Table 31.

Table 31. Short description of performed tests.

| **Test** | **Geometry** |
|---|---|
| Preliminary Tests | CRs on tripods with different radar settings.<br>Decoy-UAS with CR on tripods with different radar settings. |
| Ground Tests A | CR and target-UAS on tripods at different distances. |
| Ground Tests B | Two and three in-line CRs and target-UAS on tripods at different distances. |
| Ground Tests C | Three CRs in triangular geometries and target-UAS on tripods at different distances. |
| Flight Tests | Three decoy-UASs on tripods and flying target-UAS at different distances.<br>Two flying decoy-UAS and flying target-UAS. |

The tests were designed according to a step-procedure, increasing the number of decoy-UASs, and changing the swarm geometry:

- Preliminary Tests. Ground tests were executed with a CR and a decoy-UAS equipped with a CR on wooden tripods to properly set the radar parameters, such as the gain and the preset. Several distances between the tripods and the radar were tested to compute the magnitude of peak target.

- Ground Tests A. Ground tests were executed with a CR and a target-UAS on tripods to evaluate the protection effect changing the distance between the CR and the target-UAS.
- Ground Tests B. Ground tests were executed with two and three in-line CRs and a target-UAS on tripods to evaluate the minimum number of decoy-UASs that allows to obscure the target-UAS. Different distances were evaluated between the line of CRs and the target-UAS.
- Ground Test C. Ground Tests were executed displacing three decoy-UASs in an equilateral triangular geometry and varying the distance between the radar and the swarm, the distance between the swarm and the target-UAS, and the length of the triangular geometry side.
- Flight Tests. A first test was performed with decoy-UASs on tripods and a flying target-UAS. Then, flying decoy-UASs and target-UAS were tested to compute the distance at which the target-UAS was obscured.

After the radar parameters tuning during Preliminary Tests and UAS characterization during Ground Tests A, Ground Tests B and Ground Tests C allowed to define the maximum distance that can be set between the swarm and the target-UAS for the assessed number of decoy-UASs, according respectively to the geometries reported in Fig. 43.

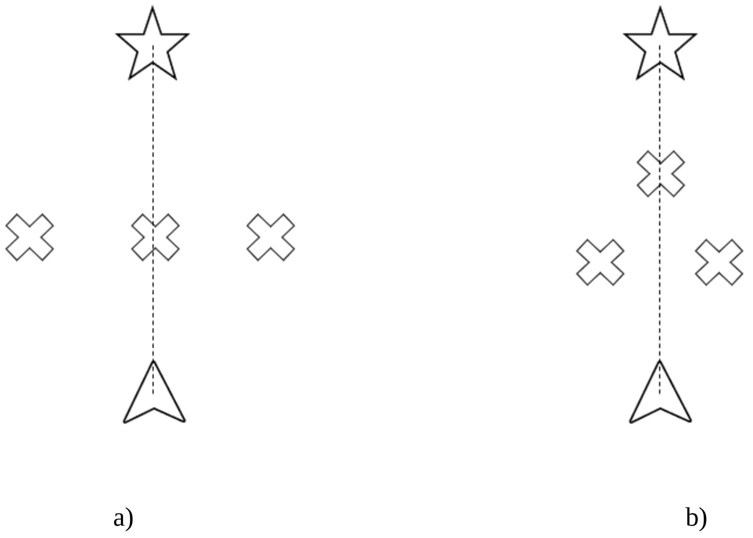

Fig. 43. Swarm geometries tested during Ground Tests B and Ground Tests C. The arrow represents the radar, the star the target-UAS, and the crosses the decoy-UASs. a) In-line geometry of decoy-UASs. b) Triangular geometry of decoy-UASs.

Specifically, fixing the distance between the radar and the swarm at 3.00m and considering three decoy-UASs, the maximum distance between the swarm and the target-UAS that allows to obscure the target-UAS is 4.00m for decoy-UASs in triangular geometry with side length equals to 0.70m. Instead, the distance of 4.00m did not allow to achieve the goal for in-line decoy-UASs, as summarized in Table 32.

Table 32. Comparison between the magnitude of target peak obtained according to the in-line and triangular geometry of decoy-UASs.

| **Geometry** | **Estimated peak distance (m)** | **Magnitude of radar echo (dB)** |
|---|---|---|
| Stand-alone target-UAS<br>Fig. 43 (a) | 6.98 | -41 |
| CRs without target-UAS<br>Fig. 43 (a) | 3.08 | 46 |
| Target-UAS and CRs<br>Fig. 43 (a) | 6.98 | -46 |
| Stand-alone target-UAS<br>Fig. 43 (b) | 7.14 | -27 |
| CRs without target-UAS<br>Fig. 43 (b) | 3.73 | 38 |
| Target-UAS and CRs<br>Fig. 43 (b) | 6.98 | -34 |

So, the triangular geometry showed a more performant behavior. Increasing the distance between the radar and the swarm to 7.00m and the length of the triangular geometry side to 2.50m, the maximum adequate distance between the swarm and the target-UAS is 7.30m. The results are reported in Table 33.

Table 33. Magnitude of target peak obtained increasing the distance values in the triangular geometry of decoy-UASs.

| **Geometry** | **Estimated peak distance (m)** | **M (dB)** |
|---|---|---|
| Stand-alone target-UAS<br>Fig. 43 (a) | 6.98 | -41 |
| CRs without target-UAS<br>Fig. 43 (a) | 3.08 | 46 |
| Target-UAS and CRs<br>Fig. 43 (a) | 6.98 | -46 |

At the end, flights tests allowed to evaluate the most appropriate strategy for flying UASs. Considering hoovering decoy-UASs and a target-UAS in manual flight mode, the estimated closest distance at which the target-UAS was not protected is 12.66 m.

# 7. Conclusion

This work describes innovative systems and solutions that were developed to support the integration of Unmanned Aerial Systems in civil airspace. The Unmanned Traffic Management services were analyzed to identify systems and procedures that can support adequate solutions. The work drivers are related to the achievement of the following objectives.

- Accurate and efficient solutions allow to develop on-board and on-ground systems that are characterized by high levels of reliability and integrity.
- The systems must support Unmanned Traffic Management services according to the regulation requirements defined by proper authorities.
- The realization of compact and lightweight systems can be obtained thanks to the use of already available high-performance Micro Electro-Mechanical Systems.
- A competitive cost reduction strategy can be developed by integrating low-cost Commercial Off The Shelf and the mass-producing modules that are in common with different vehicles.

The scientific rigor of the presented activities was supported by an adequate methodological approach according to the following steps:

- The objectives of the work were defined and the original contribution of the proposed solutions with respect to the current state of the art was underlined.
- The developed methodology was described for the method reproducibility.
- Proper test strategies were designed and implemented to validate the proposed solutions. The test equipment was described in detail.
- The results were analyzed and compared with proper benchmarks. Advantages and limitations of the proposed solutions were discussed.

The work started with a comprehensive analysis of the Unmanned Aerial System market and regulations as reported in Chapter 1. The economic and social impact of Unmanned Traffic Management integration described in Chapter 2 allowed to define the work drivers presenting innovative integration and processing of available technologies rather than the research of new paradigms.

To face the different and under development needs of Unmanned Traffic Management, a task-oriented Mission Management System called BRAINS was designed to support an easy on-board system integration according to the mission requirements. The modular configuration described in Chapter 3 includes a *core section* that can be mass-produced for different vehicles and a *custom section* that must be developed for specific applications. This approach allows to avoid on-board redundant modules that are used only for a few cases that need particular solutions to achieve the mission goal or match the Unmanned Traffic Management requirements and focus on common modules that can be adopted by different unmanned systems. Three examples of traditional functions, i.e. Guidance, Navigation, and Control functions, were developed by using synthetic functions thanks to an adequate integration of the identified modules. Some studies related to the use of low-cost Micro Electro-Mechanical Systems were proposed as case studies of on-board hardware integration.

Considering the need of sharing data about traffic in the surrounding airspace, Chapter 4 presents a Deep learning based method for Trajectory Prediction. Unmanned Aerial System time-of-flight and battery discharge can be predicted considering the nominal path and the wind vector as input parameters. The results show that the percent error between the true and the predicted parameter is about 5% for time-of-flight prediction and less than 4% for battery discharge prediction during the training and test phases. The proposed approach allows to support Unmanned Traffic Management operations during the strategic phase of flight plan approval and the tactical phase of re-planning. The standardization of the proposed methodology for different vehicles and the definition of proper alarm thresholds contribute to a safety-oriented scenario for advanced applications, such as package delivery, surveillance, mapping in a non-segregated airspace according to standard scenarios. Two applications were proposed: the use of time-of-flight prediction for Conflict Detection that allows to predict the time-of-flight to the Closest Point of Approach, and the use of absorbed current integral and battery State Of Charge for Contingency Management to evaluate if a Safe Landing Area can be reached with the remaining battery level. The proposed waypoint-based approach can be extended to the case in which a stop maneuver over the planned waypoint is not to be performed: a new training dataset shall be acquired without the stop and turn mode and adopting proper safety strategies to monitor the surrounding airspace. Synthetic data about the traffic flight parameters can be shared thanks to the BRAINS *Traffic Communication* unit.

An accurate solution to reduce the error drift of heading angle in environments that requires high navigation performance is presented in Chapter 5. A polarimetric camera can be integrated with inertial sensors to obtain an accurate estimation of heading angle exploiting the skylight polarization pattern. An innovative image processing allowed to detect the Sun meridian/anti-meridian in images collected by the polarimetric camera identifying the discontinuity of the Angle of Linear Polarization pattern. The obtained error is in the order of 1deg and it allows to exploit the proposed approach in environments where the integration of inertial sensors with other navigation systems, such as the satellite-based systems, is challenging. Urban canyon condition is a critical case study for Unmanned Traffic Management that can be analyzed to adopt this navigation method. Moreover, Unmanned Underwater Systems can also benefit from the use of the Sun light polarization pattern up to few meters under the sea level, reducing the need to re-emerge to acquire satellite-based navigation data. This solution can be involved in the BRAINS *Navigation Measurements Sensors* unit.

Swarming capabilities of Unmanned Aerial Systems represent an interesting case-study to be analyzed for adequate configurations. Proper Unmanned Traffic Management procedures must be developed to regulate the use and the systems of swarms. Chapter 6 includes the design and test of two configurations of Unmanned Aerial System swarm to support emergency conditions and military applications. A swarm of properly equipped Unmanned Aerial Systems was designed to contrast the pandemic diffusion for monitoring, transport, and liquid spread tasks. Specifically, the monitoring swarm test that includes two Unmanned Aerial Systems equipped with visible band cameras was reported to compute the social distancing in crowded areas. An error of about 5% was obtained for the relative distance between two targets thanks to the use of proper stereoscopy technique. The second application involves a swarm used for aircraft self-protection by ground-based radar detection. The main aim of the activity was the identification of the swarm configuration that better electromagnetically obscure a target thanks to the on-board installation of Corner Reflectors. The triangular configuration of three decoy-units was identified as the minimum configuration that allows to protect the target at a reasonable scaled distance of about 7m.

A schematic description of the work motivations, methodology and results is reported in Fig. 44.

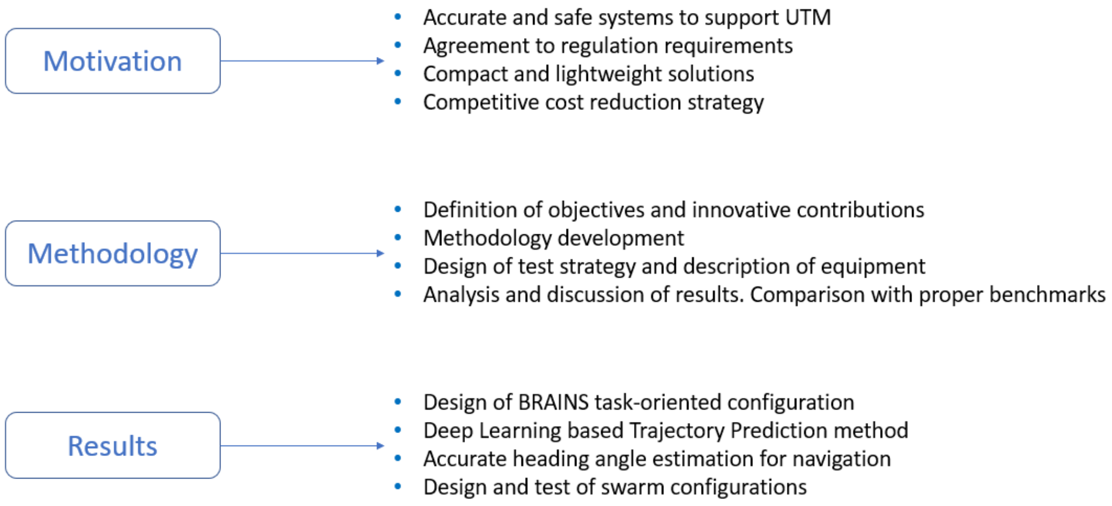

Fig. 44. Schematic description of the work conclusion.

# References

[1] "European drones outlook study - Publications Office of the EU." https://op.europa.eu/en/publication-detail/-/publication/93d90664-28b3-11e7-ab65-01aa75ed71a1/language-en (accessed Sep. 22, 2022).

[2] "Drones (UAS) | EASA." https://www.easa.europa.eu/en/the-agency/faqs/drones-uas (accessed Sep. 22, 2022).

[3] "Unmanned Aircraft Systems (UAS) | Federal Aviation Administration." https://www.faa.gov/uas (accessed Sep. 22, 2022).

[4] J. Gundlach, "Designing Unmanned Aircraft Systems: A Comprehensive Approach," *Designing Unmanned Aircraft Systems: A Comprehensive Approach*, Jul. 2012.

[5] "ICAO Model UAS Regulations." https://www.icao.int/safety/UA/Pages/ICAO-Model-UAS-Regulations.aspx (accessed Sep. 22, 2022).

[6] "EUR-Lex - 32019R0945 - EN - EUR-Lex." https://eur-lex.europa.eu/legal-content/EN/TXT/?uri=CELEX%3A32019R0945 (accessed Sep. 22, 2022).

[7] "EUR-Lex - 32019R0947 - EN - EUR-Lex." https://eur-lex.europa.eu/legal-content/EN/TXT/?uri=CELEX%3A32019R0947 (accessed Sep. 22, 2022).

[8] "Open Category - Civil Drones | EASA." https://www.easa.europa.eu/en/domains/civil-drones/drones-regulatory-framework-background/open-category-civil-drones (accessed Sep. 22, 2022).

[9] "Specific Category - Civil Drones | EASA." https://www.easa.europa.eu/en/domains/civil-drones/drones-regulatory-framework-background/specific-category-civil-drones (accessed Sep. 22, 2022).

[10] "Certified Category - Civil Drones | EASA." https://www.easa.europa.eu/en/domains/civil-drones/drones-regulatory-framework-background/certified-category-civil-drones (accessed Sep. 22, 2022).

[11] "UTM Guidance." https://www.icao.int/safety/UA/Pages/UTM-Guidance.aspx (accessed Sep. 22, 2022).

[12] “SESAR Joint Undertaking | Delivering the Digital European Sky.” https://www.sesarju.eu/ (accessed Sep. 22, 2022).

[13] “SESAR Joint Undertaking | U-space.” https://www.sesarju.eu/U-space (accessed Sep. 22, 2022).

[14] “SESAR Joint Undertaking | Concept of Operations for EuRopean UTM Systems - CORUS.” https://www.sesarju.eu/projects/corus (accessed Sep. 22, 2022).

[15] “SESAR Joint Undertaking | Advanced Integrated RPAS Avionics Safety Suite (AIRPASS).” https://www.sesarju.eu/node/3327 (accessed Sep. 22, 2022).

[16] “SESAR Joint Undertaking | Geofencing for safe and autonomous flight in Europe - GEOSAFE.” https://www.sesarju.eu/projects/geosafe (accessed Sep. 22, 2022).

[17] “SESAR Joint Undertaking | A European UTM testbed for U-space - EuroDRONE.” https://www.sesarju.eu/node/3202 (accessed Sep. 22, 2022).

[18] “SESAR Joint Undertaking | DACUS - Demand and Capacity Optimisation in U-space.” https://www.sesarju.eu/projects/dacus (accessed Sep. 22, 2022).

[19] “SESAR Joint Undertaking | Metropolis 2 - A unified approach to airspace design and separation management for U-space.” https://www.sesarju.eu/projects/Metropolis2 (accessed Sep. 22, 2022).

[20] “SESAR Joint Undertaking | CORUS-XUAM - Concept of Operations for European U-space Services - Extension for Urban Air Mobility.” https://www.sesarju.eu/projects/CORUSXUAM (accessed Sep. 22, 2022).

[21] “SESAR Joint Undertaking | AMU-LED - Air mobility urban - Large experimental demonstrations.” https://www.sesarju.eu/projects/AMU-LED (accessed Sep. 22, 2022).

[22] “SESAR Joint Undertaking | USEPE - U-space Separation in Europe.” https://www.sesarju.eu/projects/USEPE (accessed Sep. 22, 2022).

[23] “EUR-Lex - 32021R0664 - EN - EUR-Lex.” https://eur-lex.europa.eu/legal-content/EN/TXT/?uri=CELEX%3A32021R0664 (accessed Sep. 22, 2022).

[24] C. Capitán, H. Pérez-León, J. Capitán, Á. Castaño, and A. Ollero, “Unmanned Aerial Traffic Management System Architecture for U-Space In-Flight Services,” *Applied Sciences 2021, Vol. 11, Page 3995*, vol. 11, no. 9, p. 3995, Apr. 2021, doi: 10.3390/APP11093995.

[25] “Next Generation Air Transportation System (NextGen) | Federal Aviation Administration.” https://www.faa.gov/nextgen (accessed Sep. 22, 2022).

[26] “UTM Pilot Program (UPP) | Federal Aviation Administration.” https://www.faa.gov/uas/research_development/traffic_management/utm_pilot_program (accessed Sep. 22, 2022).

[27] “UAS Integration Pilot Program | Federal Aviation Administration.” https://www.faa.gov/uas/programs_partnerships/completed/integration_pilot_program (accessed Sep. 22, 2022).

[28] “BEYOND | Federal Aviation Administration.” https://www.faa.gov/uas/programs_partnerships/beyond (accessed Sep. 22, 2022).

[29] “UTM Concept of Operations Version 2.0 (UTM ConOps v2.0) | Federal Aviation Administration.” https://www.faa.gov/researchdevelopment/trafficmanagement/utm-concept-operations-version-20-utm-conops-v20 (accessed Sep. 22, 2022).

[30] “FAA Aerospace Forecasts.” https://www.faa.gov/data_research/aviation/aerospace_forecasts (accessed Sep. 22, 2022).

[31] “Full Report - Study on the societal acceptance of Urban Air Mobility in Europe | EASA.” https://www.easa.europa.eu/en/full-report-study-societal-acceptance-urban-air-mobility-europe (accessed Sep. 22, 2022).

[32] E. Pastor, C. Barrado, P. Royo, J. Lopez, and E. Santamari, “An Open Architecture for the Integration of UAV Civil Applications,” *Aerial Vehicles*, Jan. 2009, doi: 10.5772/6488.

[33] E. Baskaya, G. Manfredi, M. Bronz, and D. Delahaye, “Flexible open architecture for UASs integration into the airspace: Paparazzi autopilot system,” *AIAA/IEEE*

*Digital Avionics Systems Conference - Proceedings*, vol. 2016-December, Dec. 2016, doi: 10.1109/DASC.2016.7778016.

[34] M. Barbier, E. Bensana, and X. Pucel, "A generic and modular architecture for maritime autonomous vehicles," *AUV 2018 - 2018 IEEE/OES Autonomous Underwater Vehicle Workshop, Proceedings*, Nov. 2018, doi: 10.1109/AUV.2018.8729765.

[35] J. Muñoz-Castaner, R. Asorey-Cacheda, F. J. Gil-Castineira, F. J. González-Castaño, and P. S. Rodríguez-Hernández, "A review of aeronautical electronics and its parallelism with automotive electronics," *IEEE Transactions on Industrial Electronics*, vol. 58, no. 7, pp. 3090–3100, Jul. 2011, doi: 10.1109/TIE.2010.2077614.

[36] R. S. McEwen, S. P. Rock, and B. Hobson, "Iceberg Wall Following and Obstacle Avoidance by an AUV," in *2018 IEEE/OES Autonomous Underwater Vehicle Workshop (AUV)*, 2018, pp. 1–8. doi: 10.1109/AUV.2018.8729724.

[37] P. M. Laso, D. Brosset, and M.-A. Giraud, "Defining Role-Based Access Control for a Secure Platform of Unmanned Surface Vehicle fleets," in *OCEANS 2019 - Marseille*, 2019, pp. 1–4. doi: 10.1109/OCEANSE.2019.8867389.

[38] C. Conte, G. de Alteriis, G. Rufino, and D. Accardo, "An innovative process-based mission management system for unmanned vehicles," *2020 IEEE International Workshop on Metrology for AeroSpace, MetroAeroSpace 2020 - Proceedings*, pp. 377–381, Jun. 2020, doi: 10.1109/METROAEROSPACE48742.2020.9160121.

[39] "BeagleBoard.org - blue." https://beagleboard.org/blue (accessed Sep. 22, 2022).

[40] "Raspberry Pi 4 Model B – Raspberry Pi." https://www.raspberrypi.com/products/raspberry-pi-4-model-b/ (accessed Sep. 22, 2022).

[41] "NUCLEO-F401RE - STM32 Nucleo-64 development board with STM32F401RE MCU, supports Arduino and ST morpho connectivity - STMicroelectronics." https://www.st.com/content/st_com/en/products/evaluation-tools/product-

evaluation-tools/mcu-mpu-eval-tools/stm32-mcu-mpu-eval-tools/stm32-nucleo-boards/nucleo-f401re.html (accessed Sep. 22, 2022).

[42] G. de Alteriis, C. Conte, R. S. lo Moriello, and D. Accardo, "Use of consumer-grade MEMS inertial sensors for accurate attitude determination of drones," *2020 IEEE International Workshop on Metrology for AeroSpace, MetroAeroSpace 2020 - Proceedings*, pp. 534–538, Jun. 2020, doi: 10.1109/METROAEROSPACE48742.2020.9160134.

[43] G. de Alteriis, D. Accardo, C. Conte, and R. S. lo Moriello, "Performance Enhancement of Consumer-Grade MEMS Sensors through Geometrical Redundancy," *Sensors 2021, Vol. 21, Page 4851*, vol. 21, no. 14, p. 4851, Jul. 2021, doi: 10.3390/S21144851.

[44] G. de Alteriis, V. Bottino, C. Conte, G. Rufino, and R. S. lo Moriello, "Accurate attitude inizialization procedure based on MEMS IMU and magnetometer integration," *2021 IEEE International Workshop on Metrology for AeroSpace, MetroAeroSpace 2021 - Proceedings*, pp. 1–6, Jun. 2021, doi: 10.1109/METROAEROSPACE51421.2021.9511679.

[45] G. de Alteriis, C. Conte, D. Accardo, G. Rufino, R. S. lo Moriello, and O. H. Alvarez, "Advanced technique to support ADS system failure exploiting MEMS inertial sensors," *AIAA Science and Technology Forum and Exposition, AIAA SciTech Forum 2022*, 2022, doi: 10.2514/6.2022-0856.

[46] E. Caputo *et al.*, "Development of an Embedded System-Based Dropper Payload for Drones," in *Metrology for AeroSpace (MetroAeroSpace)*, Aug. 2022, pp. 639–643. doi: 10.1109/METROAEROSPACE54187.2022.9856205.

[47] G. de Alteriis *et al.*, "Low-Cost and High-Performance Solution for Positioning and Monitoring of Large Structures," *Sensors 2022, Vol. 22, Page 1788*, vol. 22, no. 5, p. 1788, Feb. 2022, doi: 10.3390/S22051788.

[48] B. Custers, "The Future of Drone Use Opportunities and Threats from Ethical and Legal Perspectives," *Information Technology and Law Series IT&LAW*, vol. 27, 2016.

[49] F. Giones and A. Brem, “From toys to tools: The co-evolution of technological and entrepreneurial developments in the drone industry,” *Bus Horiz*, vol. 60, no. 6, pp. 875–884, Nov. 2017, doi: 10.1016/J.BUSHOR.2017.08.001.

[50] V. Santamarina Campos, M. de Miguel Molina, and S. Kröner, “Ethics and Civil Drones,” *SpringerBriefs in Law* , 2018, doi: 10.1007/978-3-319-71087-7.

[51] “NUCLEO-F446RE - STM32 Nucleo-64 development board with STM32F446RE MCU, supports Arduino and ST morpho connectivity - STMicroelectronics.” https://www.st.com/en/evaluation-tools/nucleo-f446re.html (accessed Sep. 22, 2022).

[52] “Safran - STIM318.” https://www.sensonor.com/products/inertial-measurement-units/stim318/ (accessed Sep. 27, 2022).

[53] “Blackfly S GigE | Teledyne FLIR.” https://www.flir.it/products/blackfly-s-gige/?model=BFS-PGE-51S5P-C (accessed Sep. 22, 2022).

[54] “Digital sovereignty: Commission proposes Chips Act.” https://ec.europa.eu/commission/presscorner/detail/en/IP_22_729 (accessed Sep. 27, 2022).

[55] H. Casper, A. Rexford, D. Riegel, A. Robinson, E. Martin, and M. Awwad, “The Impact of the Computer Chip Supply Shortage”.

[56] J. Voas, N. Kshetri, and J. F. Defranco, “Scarcity and Global Insecurity: The Semiconductor Shortage,” *IT Prof*, vol. 23, no. 5, pp. 78–82, 2021, doi: 10.1109/MITP.2021.3105248.

[57] “BADA - an advanced aircraft performance model for present and future ATM systems | EUROCONTROL.” https://www.eurocontrol.int/publication/bada-advanced-aircraft-performance-model-present-and-future-atm-systems (accessed Sep. 22, 2022).

[58] H. Usach and J. A. Vila, “Reconfigurable Mission Plans for RPAS,” *Aerosp Sci Technol*, vol. 96, p. 105528, Jan. 2020, doi: 10.1016/J.AST.2019.105528.

[59] M. Huang, W. Y. Ochieng, J. J. Escribano Macias, and Y. Ding, “Accuracy evaluation of a new generic Trajectory Prediction model for Unmanned Aerial Vehicles,” *Aerosp Sci Technol*, vol. 119, p. 107160, Dec. 2021, doi: 10.1016/J.AST.2021.107160.

[60] M. Prandini, J. Hu, J. Lygeros, and S. Sastry, “A Probabilistic Approach to Aircraft Conflict Detection,” *IEEE Transactions on Intelligent Transportation Systems*, vol. 1, no. 4, pp. 199–219, Dec. 2000, doi: 10.1109/6979.898224.

[61] A. Bashllari, N. Kaciroti, D. Nace, and A. Fundo, “Conflict probability estimations based on geometrical and Bayesian approaches,” *IEEE Conference on Intelligent Transportation Systems, Proceedings, ITSC*, pp. 479–484, 2007, doi: 10.1109/ITSC.2007.4357787.

[62] Z. Zhou, J. Chen, B. Shen, Z. Xiong, H. Shen, and F. Guo, “A trajectory prediction method based on aircraft motion model and grey theory,” *Proceedings of 2016 IEEE Advanced Information Management, Communicates, Electronic and Automation Control Conference, IMCEC 2016*, pp. 1523–1527, Feb. 2017, doi: 10.1109/IMCEC.2016.7867472.

[63] W. Schuster, “Trajectory prediction for future air traffic management – complex manoeuvres and taxiing,” *The Aeronautical Journal*, vol. 119, no. 1212, pp. 121–143, Feb. 2015, doi: 10.1017/S0001924000010307.

[64] M. Uzun and E. Koyuncu, “Data-Driven Trajectory Uncertainty Quantification For Climbing Aircraft To Improve Ground-Based Trajectory Prediction,” *Anadolu University Journal Of Science And Technology A - Applied Sciences and Engineering*, pp. 1–1, Jun. 2017, doi: 10.18038/AUBTDA.270074.

[65] J. Sun, J. Ellerbroek, and J. Hoekstra, “Modeling aircraft performance parameters with open ADS-B data,” *12th Seminar Papers*, 2017.

[66] G. Gui, F. Liu, J. Sun, J. Yang, Z. Zhou, and D. Zhao, “Flight delay prediction based on aviation big data and machine learning,” *IEEE Trans Veh Technol*, vol. 69, no. 1, pp. 140–150, Jan. 2020, doi: 10.1109/TVT.2019.2954094.

[67] X. Wang, J. Liu, T. Qiu, C. Mu, C. Chen, and P. Zhou, “A Real-Time Collision Prediction Mechanism with Deep Learning for Intelligent Transportation System,” *IEEE Trans Veh Technol*, vol. 69, no. 9, pp. 9497–9508, Sep. 2020, doi: 10.1109/TVT.2020.3003933.

[68] R. Alligier and D. Gianazza, “Learning aircraft operational factors to improve aircraft climb prediction: A large scale multi-airport study,” *Transp Res Part C Emerg Technol*, vol. 96, pp. 72–95, Nov. 2018, doi: 10.1016/J.TRC.2018.08.012.

[69] S. T. Barratt, M. J. Kochenderfer, and S. P. Boyd, “Learning Probabilistic Trajectory Models of Aircraft in Terminal Airspace from Position Data,” *IEEE Transactions on Intelligent Transportation Systems*, vol. 20, no. 9, pp. 3536–3545, Sep. 2019, doi: 10.1109/TITS.2018.2877572.

[70] M. Xue, “Uav trajectory modeling using neural networks.” 2017.

[71] L. Ma and S. Tian, “A Hybrid CNN-LSTM Model for Aircraft 4D Trajectory Prediction,” *IEEE Access*, vol. 8, pp. 134668–134680, 2020, doi: 10.1109/ACCESS.2020.3010963.

[72] R. Casado and A. Bermúdez, “Neural Network-Based Aircraft Conflict Prediction in Final Approach Maneuvers,” *Electronics 2020, Vol. 9, Page 1708*, vol. 9, no. 10, p. 1708, Oct. 2020, doi: 10.3390/ELECTRONICS9101708.

[73] S. J. Pan and Q. Yang, “A survey on transfer learning,” *IEEE Trans Knowl Data Eng*, vol. 22, no. 10, pp. 1345–1359, 2010, doi: 10.1109/TKDE.2009.191.

[74] F. L. da Silva and A. H. Reali Costa, “A Survey on Transfer Learning for Multiagent Reinforcement Learning Systems,” *Journal of Artificial Intelligence Research*, vol. 64, pp. 645–703, Mar. 2019, doi: 10.1613/JAIR.1.11396.

[75] W. Dai, B. Pang, and K. H. Low, “Conflict-free four-dimensional path planning for urban air mobility considering airspace occupancy,” *Aerosp Sci Technol*, vol. 119, p. 107154, Dec. 2021, doi: 10.1016/J.AST.2021.107154.

[76] Y. Lin, J. wei Zhang, and H. Liu, “Deep learning based short-term air traffic flow prediction considering temporal–spatial correlation,” *Aerosp Sci Technol*, vol. 93, p. 105113, Oct. 2019, doi: 10.1016/J.AST.2019.04.021.

[77] C. Conte, G. de Alteriis, R. S. lo Moriello, D. Accardo, and G. Rufino, "Drone Trajectory Segmentation for Real-Time and Adaptive Time-Of-Flight Prediction," *Drones 2021, Vol. 5, Page 62*, vol. 5, no. 3, p. 62, Jul. 2021, doi: 10.3390/DRONES5030062.

[78] "DJI Mavic 2 Enterprise." https://www.dji.com/it/mavic-2-enterprise (accessed Sep. 22, 2022).

[79] "UgCS." https://www.ugcs.com/. (accessed Sep. 22, 2022).

[80] "EUR-Lex - 32020R0639 - EN - EUR-Lex." https://eur-lex.europa.eu/legal-content/EN/TXT/?uri=CELEX%3A32020R0639 (accessed Sep. 22, 2022).

[81] A. B. Chatfield, "Fundamentals Of High Accuracy Inertial Navigation," *Fundamentals Of High Accuracy Inertial Navigation*, Jan. 1997, doi: 10.2514/4.866463.

[82] C. Conte, D. Accardo, and G. Rufino, "Trajectory flight-time prediction based on machine learning for unmanned traffic management," *AIAA/IEEE Digital Avionics Systems Conference - Proceedings*, vol. 2020-October, Oct. 2020, doi: 10.1109/DASC50938.2020.9256513.

[83] "ICAO - Global TBO Concept ." https://www.icao.int/airnavigation/tbo/Pages/Why-Global-TBO-Concept.aspx (accessed Sep. 22, 2022).

[84] S. Mondoloni and N. Rozen, "Aircraft trajectory prediction and synchronization for air traffic management applications," *Progress in Aerospace Sciences*, vol. 119, p. 100640, Nov. 2020, doi: 10.1016/J.PAEROSCI.2020.100640.

[85] I. Goodfellow, Y. Bengio, and A. Courville, *Deep Learning*. 2016.

[86] H. Hassan *et al.*, "A Machine Learning Approach to Achieving Energy Efficiency in Relay-Assisted LTE-A Downlink System," *Sensors 2019, Vol. 19, Page 3461*, vol. 19, no. 16, p. 3461, Aug. 2019, doi: 10.3390/S19163461.

[87] M. Kayri, "Predictive Abilities of Bayesian Regularization and Levenberg–Marquardt Algorithms in Artificial Neural Networks: A Comparative Empirical

Study on Social Data,” *Mathematical and Computational Applications 2016, Vol. 21, Page 20*, vol. 21, no. 2, p. 20, May 2016, doi: 10.3390/MCA21020020.

[88] A. Gowida, T. Moussa, S. Elkatatny, and A. Ali, “A Hybrid Artificial Intelligence Model to Predict the Elastic Behavior of Sandstone Rocks,” *Sustainability 2019, Vol. 11, Page 5283*, vol. 11, no. 19, p. 5283, Sep. 2019, doi: 10.3390/SU11195283.

[89] L. G. Garbett, “Admiral Sir Francis Beaufort and the Beaufort Scales of wind and weather,” *Quarterly Journal of the Royal Meteorological Society*, vol. 52, no. 218, pp. 161–172, Apr. 1926, doi: 10.1002/QJ.49705221807.

[90] D. de Dominicis, C. Conte, F. Mattei, G. Rufino, and D. Accardo, “Trajectory Prediction and Conflict Detection for Unmanned Traffic Management: a Performance Comparison of Machine-Learning-Based Approaches,” in *Metrology for AeroSpace (MEtroAeroSpace)*, Aug. 2022, pp. 633–638. doi: 10.1109/METROAEROSPACE54187.2022.9855940.

[91] M. A. Hannan *et al.*, “Toward Enhanced State of Charge Estimation of Lithium-ion Batteries Using Optimized Machine Learning Techniques,” *Scientific Reports 2020 10:1*, vol. 10, no. 1, pp. 1–15, Mar. 2020, doi: 10.1038/s41598-020-61464-7.

[92] M. Danko, J. Adamec, M. Taraba, and P. Drgona, “Overview of batteries State of Charge estimation methods,” *Transportation Research Procedia*, vol. 40, pp. 186–192, Jan. 2019, doi: 10.1016/J.TRPRO.2019.07.029.

[93] W. Zhou, Y. Zheng, Z. Pan, and Q. Lu, “Review on the Battery Model and SOC Estimation Method,” *Processes 2021, Vol. 9, Page 1685*, vol. 9, no. 9, p. 1685, Sep. 2021, doi: 10.3390/PR9091685.

[94] W.-Y. Chang, “The State of Charge Estimating Methods for Battery: A Review,” *ISRN Applied Mathematics*, vol. 2013, pp. 1–7, Jul. 2013, doi: 10.1155/2013/953792.

[95] B. Bole, M. Daigle, and G. Gorospe, “Online Prediction of Battery Discharge and Estimation of Parasitic Loads for an Electric Aircraft,” *PHM Society European Conference*, vol. 2, no. 1, 2014, doi: 10.36001/PHME.2014.V2I1.1535.

[96] X. Wang, J. Li, B. C. Shia, Y. W. Kao, C. W. Ho, and M. C. Chen, "A Novel Prediction Process of the Remaining Useful Life of Electric Vehicle Battery Using Real-World Data," *Processes 2021, Vol. 9, Page 2174*, vol. 9, no. 12, p. 2174, Dec. 2021, doi: 10.3390/PR9122174.

[97] L. Chen, J. An, H. Wang, M. Zhang, and H. Pan, "Remaining useful life prediction for lithium-ion battery by combining an improved particle filter with sliding-window gray model," *Energy Reports*, vol. 6, pp. 2086–2093, Nov. 2020, doi: 10.1016/J.EGYR.2020.07.026.

[98] S. S. Mansouri, P. Karvelis, G. Georgoulas, and G. Nikolakopoulos, "Remaining Useful Battery Life Prediction for UAVs based on Machine Learning," *IFAC-PapersOnLine*, vol. 50, no. 1, pp. 4727–4732, Jul. 2017, doi: 10.1016/J.IFACOL.2017.08.863.

[99] W. Cheng, Z. Yi, J. Liang, Y. Song, and D. Liu, "An SOC and SOP Joint Estimation Method of Lithium-ion Batteries in Unmanned Aerial Vehicles," *International Conference on Sensing, Measurement and Data Analytics in the Era of Artificial Intelligence, ICSMD 2020 - Proceedings*, pp. 247–252, Oct. 2020, doi: 10.1109/ICSMD50554.2020.9261659.

[100] C. Che, H. Wang, Q. Fu, and X. Ni, "Combining multiple deep learning algorithms for prognostic and health management of aircraft," *Aerosp Sci Technol*, vol. 94, p. 105423, Nov. 2019, doi: 10.1016/J.AST.2019.105423.

[101] C. Conte, G. Rufino, G. de Alteriis, V. Bottino, and D. Accardo, "A Data-Driven Learning Method for Online Prediction of Drone Battery Discharge," *Unpublished*.

[102] "Kestrel 5500 Weather Meter." https://kestrelmeters.com/products/kestrel-5500-weather-meter?utm_campaign=cs_w&utm_source=it-kestrelmeters.glopalstore.com&utm_medium=wi_proxy&utm_content=it_IT&utm_term=b&gl_currency=USD&gl_language=en (accessed Sep. 28, 2022).

[103] S. C. Chapra and R. P. Canale, *Numerical methods for engineers*. 2021.

[104] "Improve Shallow Neural Network Generalization and Avoid Overfitting - MATLAB & Simulink - MathWorks Italia." https://it.mathworks.com/help/deeplearning/ug/improve-neural-network-generalization-and-avoid-overfitting.html (accessed Sep. 28, 2022).

[105] J. Kim, S. Kim, J. Jeong, H. Kim, J. S. Park, and T. Kim, "CBDN: Cloud-Based Drone Navigation for Efficient Battery Charging in Drone Networks," *IEEE Transactions on Intelligent Transportation Systems*, vol. 20, no. 11, pp. 4174–4191, Nov. 2019, doi: 10.1109/TITS.2018.2883058.

[106] A. Troudi, S. A. Addouche, S. Dellagi, and A. el Mhamedi, "Sizing of the Drone Delivery Fleet Considering Energy Autonomy," *Sustainability 2018, Vol. 10, Page 3344*, vol. 10, no. 9, p. 3344, Sep. 2018, doi: 10.3390/SU10093344.

[107] C. W. Hawryshyn, "Polarization Vision in Fish," *Am Sci*, 1992.

[108] S. Heinze, "Polarized-light processing in insect brains: Recent insights from the desert locust, the monarch butterfly, the cricket, and the fruit fly," *Polarized Light and Polarization Vision in Animal Sciences, Second Edition*, vol. 2, pp. 61–111, Jan. 2014, doi: 10.1007/978-3-642-54718-8_4/FIGURES/12.

[109] S. M. Reppert, H. Zhu, and R. H. White, "Polarized light helps monarch butterflies navigate," *Curr Biol*, vol. 14, no. 2, pp. 155–158, Jan. 2004, doi: 10.1016/J.CUB.2003.12.034.

[110] M. Sarkar, D. S. S. Bello, C. van Hoof, and A. Theuwissen, "Integrated polarization analyzing cmos image sensor for autonomus navigation using polarized light," *2010 IEEE International Conference on Intelligent Systems, IS 2010 - Proceedings*, pp. 224–229, 2010, doi: 10.1109/IS.2010.5548344.

[111] C. Fan, X. Hu, X. He, L. Zhang, and J. Lian, "Integrated Polarized Skylight Sensor and MIMU with a Metric Map for Urban Ground Navigation," *IEEE Sens J*, vol. 18, no. 4, pp. 1714–1722, Feb. 2018, doi: 10.1109/JSEN.2017.2786404.

[112] C. Fan, X. Hu, J. Lian, L. Zhang, and X. He, "Design and Calibration of a Novel Camera-Based Bio-Inspired Polarization Navigation Sensor," *IEEE Sens J*, vol. 16, no. 10, pp. 3640–3648, May 2016, doi: 10.1109/JSEN.2016.2533628.

[113] H. Zhao *et al.*, “Polarization patterns under different sky conditions and a navigation method based on the symmetry of the AOP map of skylight,” *Opt Express*, vol. 26, no. 22, p. 28589, Oct. 2018, doi: 10.1364/OE.26.028589.

[114] T. Ma *et al.*, “An Evaluation of Skylight Polarization Patterns for Navigation,” *Sensors (Basel)*, vol. 15, no. 3, p. 5895, Mar. 2015, doi: 10.3390/S150305895.

[115] C. Conte, G. de Alteriis, F. DePandi, R. S. lo Moriello, G. Rufino, and D. Accardo, “Integration of a Sun light Polarization Camera and Latest-Generation Inertial Sensors to Support High Integrity Navigation,” in *2021 28th Saint Petersburg International Conference on Integrated Navigation Systems (ICINS)*, 2021, pp. 1–8. doi: 10.23919/ICINS43216.2021.9470796.

[116] H. Liang, H. Bai, N. Liu, and X. Sui, “Polarization Navigation Simulation System and Skylight Compass Method Design Based upon Moment of Inertia,” *Math Probl Eng*, vol. 2020, 2020, doi: 10.1155/2020/4081269.

[117] “STEVAL-STLKT01V1 - SensorTile development kit - STMicroelectronics.” https://www.st.com/content/st_com/en/products/evaluation-tools/solution-evaluation-tools/sensor-solution-eval-boards/steval-stlkt01v1.html (accessed Sep. 22, 2022).

[118] T. M. Aycock, A. Lompado, and B. M. Wheeler, “Using Atmospheric Polarization Patterns for Azimuth Sensing,” *SPIE*, vol. 9085, p. 90850B, Jun. 2014, doi: 10.1117/12.2054107.

[119] M. Rastgoo, C. Demonceaux, R. Seulin, and O. Morel, “Attitude Estimation from Polarimetric Cameras,” *IEEE International Conference on Intelligent Robots and Systems*, pp. 8397–8403, Dec. 2018, doi: 10.1109/IROS.2018.8593575.

[120] M. Blanco-Muriel, D. C. Alarcón-Padilla, T. López-Moratalla, and M. Lara-Coira, “Computing the solar vector,” *Solar Energy*, vol. 70, no. 5, pp. 431–441, Jan. 2001, doi: 10.1016/S0038-092X(00)00156-0.

[121] “NOAA - Magnetic Declination.” https://www.ngdc.noaa.gov/geomag/declination.shtml (accessed Sep. 22, 2022).

[122] P. Alken *et al.*, “International Geomagnetic Reference Field: the thirteenth generation,” *Earth, Planets and Space*, vol. 73, no. 1, pp. 1–25, Dec. 2021, doi: 10.1186/S40623-020-01288-X/FIGURES/5.

[123] Z. Qadir, F. Ullah, H. S. Munawar, and F. Al-Turjman, “Addressing disasters in smart cities through UAVs path planning and 5G communications: A systematic review,” *Comput Commun*, vol. 168, pp. 114–135, Feb. 2021, doi: 10.1016/J.COMCOM.2021.01.003.

[124] B. Galkin, J. Kibiłda, and L. A. DaSilva, “A Stochastic Model for UAV Networks Positioned Above Demand Hotspots in Urban Environments,” *IEEE Trans Veh Technol*, vol. 68, no. 7, pp. 6985–6996, Jul. 2019, doi: 10.1109/TVT.2019.2916429.

[125] L. Szarka and I. Harmati, “Swarm based drone umbrellas to counter missiles,” *2020 23rd IEEE International Symposium on Measurement and Control in Robotics, ISMCR 2020*, Oct. 2020, doi: 10.1109/ISMCR51255.2020.9263747.

[126] “Progetto-Emergenza-Sanitaria-COVID-19.” https://www.cesma.unina.it/progetti/progetto-emergenza-sanitaria-covid-19.html (accessed Sep. 22, 2022).

[127] K. B. Laksham, “Unmanned aerial vehicle (drones) in public health: A SWOT analysis,” *J Family Med Prim Care*, vol. 8, no. 2, p. 342, 2019, doi: 10.4103/JFMPC.JFMPC_413_18.

[128] M. Khosravi, S. Enayati, H. Saeedi, and H. Pishro-Nik, “Multi-Purpose Drones for Coverage and Transport Applications,” *IEEE Trans Wirel Commun*, vol. 20, no. 6, pp. 3974–3987, Jun. 2021, doi: 10.1109/TWC.2021.3054748.

[129] M. A. Ruiz Estrada, “The Uses of Drones in Case of Massive Epidemics Contagious Diseases Relief Humanitarian Aid: Wuhan-COVID-19 Crisis,” *SSRN Electronic Journal*, Feb. 2020, doi: 10.2139/SSRN.3546547.

[130] G. de Alteriis, V. Bottino, C. Conte, G. Rufino, R. S. lo Moriello, and D. Accardo, “Service for Airborne Fundamental Equipment Delivery by Remotely Operated Platforms,” *6th International Forum on Research and Technology for Society and*

*Industry, RTSI 2021 - Proceedings*, pp. 376–381, 2021, doi: 10.1109/RTSI50628.2021.9597320.

[131] A. Al-Naji, A. G. Perera, and J. Chahl, “Remote monitoring of cardiorespiratory signals from a hovering unmanned aerial vehicle,” *Biomed Eng Online*, vol. 16, no. 1, pp. 1–20, Aug. 2017, doi: 10.1186/S12938-017-0395-Y/FIGURES/15.

[132] A. Rahman, Y. Ishii, and V. Lubecke, “UAV-Radar System for Vital Sign Monitoring,” *The Applied Computational Electromagnetics Society Journal (ACES)*, vol. 33, no. 02, pp. 208–211, 2021.

[133] R. Huang, W. Su, S. Zhang, and W. Qin, “Remote Measurement of Vital Signs for Unmanned Search and Rescue Vehicles,” *2020 5th International Conference on Control and Robotics Engineering, ICCRE 2020*, pp. 164–168, Apr. 2020, doi: 10.1109/ICCRE49379.2020.9096468.

[134] D. Schneider, “The delivery drones are coming,” *IEEE Spectr*, vol. 57, no. 1, pp. 28–29, Jan. 2020, doi: 10.1109/MSPEC.2020.8946304.

[135] E. Frachtenberg, “Practical Drone Delivery,” *Computer (Long Beach Calif)*, vol. 52, no. 12, pp. 53–57, Dec. 2019, doi: 10.1109/MC.2019.2942290.

[136] T. K. Amukele, L. J. Sokoll, D. Pepper, D. P. Howard, and J. Street, “Can Unmanned Aerial Systems (Drones) Be Used for the Routine Transport of Chemistry, Hematology, and Coagulation Laboratory Specimens?,” *PLoS One*, vol. 10, no. 7, Jul. 2015, doi: 10.1371/JOURNAL.PONE.0134020.

[137] X. Q. Zhang *et al.*, “Effects of Spray Parameters of Drone on the Droplet Deposition in Sugarcane Canopy,” *Sugar Tech*, vol. 22, no. 4, pp. 583–588, Aug. 2020, doi: 10.1007/S12355-019-00792-Z/TABLES/6.

[138] H. G. Jorge, L. M. G. de Santos, N. F. Álvarez, J. M. Sánchez, and F. N. Medina, “Operational Study of Drone Spraying Application for the Disinfection of Surfaces against the COVID-19 Pandemic,” *Drones 2021, Vol. 5, Page 18*, vol. 5, no. 1, p. 18, Mar. 2021, doi: 10.3390/DRONES5010018.

[139] A. Zaarane, I. Slimani, W. al Okaishi, I. Atouf, and A. Hamdoun, “Distance measurement system for autonomous vehicles using stereo camera,” *Array*, vol. 5, p. 100016, Mar. 2020, doi: 10.1016/J.ARRAY.2020.100016.

[140] H. H. Ali and F. M. Abed, “The impact of UAV flight planning parameters on topographic mapping quality control,” *IOP Conf Ser Mater Sci Eng*, vol. 518, no. 2, p. 022018, May 2019, doi: 10.1088/1757-899X/518/2/022018.

[141] I. C. F. S. Condotta, T. M. Brown-Brandl, S. K. Pitla, J. P. Stinn, and K. O. Silva-Miranda, “Evaluation of low-cost depth cameras for agricultural applications,” *Comput Electron Agric*, vol. 173, p. 105394, Jun. 2020, doi: 10.1016/J.COMPAG.2020.105394.

[142] M. Garbey, N. Sun, A. Merla, and I. Pavlidis, “Contact-free measurement of cardiac pulse based on the analysis of thermal imagery,” *IEEE Trans Biomed Eng*, vol. 54, no. 8, pp. 1418–1426, Aug. 2007, doi: 10.1109/TBME.2007.891930.

[143] J. Fei and I. Pavlidis, “Thermistor at a distance: unobtrusive measurement of breathing,” *IEEE Trans Biomed Eng*, vol. 57, no. 4, pp. 988–998, Apr. 2010, doi: 10.1109/TBME.2009.2032415.

[144] D. Castaneda, A. Esparza, M. Ghamari, C. Soltanpur, and H. Nazeran, “A review on wearable photoplethysmography sensors and their potential future applications in health care,” *Int J Biosens Bioelectron*, vol. 4, no. 4, p. 195, 2018, doi: 10.15406/IJBSBE.2018.04.00125.

[145] M. Elgendi *et al.*, “The use of photoplethysmography for assessing hypertension,” *npj Digital Medicine 2019 2:1*, vol. 2, no. 1, pp. 1–11, Jun. 2019, doi: 10.1038/s41746-019-0136-7.

[146] M. Lewandowska, J. Rumiński, T. Kocejko, and J. Nowak, “Measuring pulse rate with a webcam — A non-contact method for evaluating cardiac activity,” in *2011 Federated Conference on Computer Science and Information Systems (FedCSIS)*, 2011, pp. 405–410.

[147] Y. Sun and N. Thakor, “Photoplethysmography revisited: from contact to noncontact, from point to imaging,” *IEEE Trans Biomed Eng*, vol. 63, no. 3, p. 463, Mar. 2016, doi: 10.1109/TBME.2015.2476337.

[148] M. Kumar, A. Veeraraghavan, and A. Sabharwal, “DistancePPG: Robust non-contact vital signs monitoring using a camera,” *Biomed Opt Express*, vol. 6, no. 5, p. 1565, May 2015, doi: 10.1364/BOE.6.001565.

[149] X. Fan, Q. Ye, X. Yang, and S. das Choudhury, “Robust blood pressure estimation using an RGB camera,” *J Ambient Intell Humaniz Comput*, vol. 11, no. 11, pp. 4329–4336, Nov. 2020, doi: 10.1007/S12652-018-1026-6/TABLES/3.

[150] J. Lee, M. Kim, H. K. Park, and I. Y. Kim, “Motion Artifact Reduction in Wearable Photoplethysmography Based on Multi-Channel Sensors with Multiple Wavelengths,” *Sensors (Basel)*, vol. 20, no. 5, Mar. 2020, doi: 10.3390/S20051493.

[151] G. Zhang *et al.*, “A Noninvasive Blood Glucose Monitoring System Based on Smartphone PPG Signal Processing and Machine Learning,” *IEEE Trans Industr Inform*, vol. 16, no. 11, pp. 7209–7218, Nov. 2020, doi: 10.1109/TII.2020.2975222.

[152] A. A. Kamshilin, I. S. Sidorov, L. Babayan, M. A. Volynsky, R. Giniatullin, and O. v. Mamontov, “Accurate measurement of the pulse wave delay with imaging photoplethysmography,” *Biomed Opt Express*, vol. 7, no. 12, p. 5138, Dec. 2016, doi: 10.1364/BOE.7.005138.

[153] S. Sanyal and K. K. Nundy, “Algorithms for Monitoring Heart Rate and Respiratory Rate From the Video of a User’s Face,” *IEEE J Transl Eng Health Med*, vol. 6, Apr. 2018, doi: 10.1109/JTEHM.2018.2818687.

[154] M. Rong and K. Li, “A Blood Pressure Prediction Method Based on Imaging Photoplethysmography in combination with Machine Learning,” *Biomed Signal Process Control*, vol. 64, p. 102328, Feb. 2021, doi: 10.1016/J.BSPC.2020.102328.

[155] J. Luo, J. Zhen, P. Zhou, W. Chen, and Y. Guo, “An iPPG-Based Device for Pervasive Monitoring of Multi-Dimensional Cardiovascular Hemodynamics,” *Sensors (Basel)*, vol. 21, no. 3, pp. 1–14, Feb. 2021, doi: 10.3390/S21030872.

[156] B. P. Yan *et al.*, “High-Throughput, Contact-Free Detection of Atrial Fibrillation From Video With Deep Learning,” *JAMA Cardiol*, vol. 5, no. 1, pp. 105–107, Jan. 2020, doi: 10.1001/JAMACARDIO.2019.4004.

[157] S. Elzeiny and M. Qaraqe, “Stress Classification Using Photoplethysmogram-Based Spatial and Frequency Domain Images,” *Sensors 2020, Vol. 20, Page 5312*, vol. 20, no. 18, p. 5312, Sep. 2020, doi: 10.3390/S20185312.

[158] M. Kebe, R. Gadhafi, B. Mohammad, M. Sanduleanu, H. Saleh, and M. Al-qutayri, “Human Vital Signs Detection Methods and Potential Using Radars: A Review,” *Sensors 2020, Vol. 20, Page 1454*, vol. 20, no. 5, p. 1454, Mar. 2020, doi: 10.3390/S20051454.

[159] F. Yang, Z. He, Y. Fu, L. Li, K. Jiang, and F. Xie, “Noncontact Detection of Respiration Rate Based on Forward Scatter Radar,” *Sensors 2019, Vol. 19, Page 4778*, vol. 19, no. 21, p. 4778, Nov. 2019, doi: 10.3390/S19214778.

[160] M. Leib, W. Menzel, B. Schleicher, and H. Schumacher, “Vital signs monitoring with a UWB radar based on a correlation receiver,” in *Proceedings of the Fourth European Conference on Antennas and Propagation*, 2010, pp. 1–5.

[161] M. Nosrati, S. Shahsavari, and N. Tavassolian, “Multi-target vital-signs monitoring using a dual-beam hybrid doppler radar,” *IMBioc 2018 - 2018 IEEE/MTT-S International Microwave Biomedical Conference*, pp. 58–60, Aug. 2018, doi: 10.1109/IMBIOC.2018.8428942.

[162] T. Zhangi, G. Valerio, J. Sarrazin, and D. Istrate, “Wavelet-based analysis of 60 GHz Doppler radar for non-stationary vital sign monitoring,” *2017 11th European Conference on Antennas and Propagation, EUCAP 2017*, pp. 1876–1877, May 2017, doi: 10.23919/EUCAP.2017.7928689.

[163] Harikesh, S. S. Chauhan, A. Basu, M. P. Abegaonkar, and S. K. Koul, “Through the Wall Human Subject Localization and Respiration Rate Detection Using

Multichannel Doppler Radar,” *IEEE Sens J*, vol. 21, no. 2, pp. 1510–1518, Jan. 2021, doi: 10.1109/JSEN.2020.3016755.

[164] Y. Chung, S. Oh, J. Lee, D. Park, H. H. Chang, and S. Kim, “Automatic Detection and Recognition of Pig Wasting Diseases Using Sound Data in Audio Surveillance Systems,” *Sensors (Basel)*, vol. 13, no. 10, p. 12929, Sep. 2013, doi: 10.3390/S131012929.

[165] S. Matos, S. S. Birring, I. D. Pavord, and D. H. Evans, “Detection of cough signals in continuous audio recordings using hidden Markov models,” *IEEE Trans Biomed Eng*, vol. 53, no. 6, pp. 1078–1083, Jun. 2006, doi: 10.1109/TBME.2006.873548.

[166] F. al Hossain, A. A. Lover, G. A. Corey, N. G. Reich, and T. Rahman, “FluSense,” *Proc ACM Interact Mob Wearable Ubiquitous Technol*, vol. 4, no. 1, p. 28, Mar. 2020, doi: 10.1145/3381014.

[167] “AudioSet.” https://research.google.com/audioset/ (accessed Sep. 23, 2022).

[168] A. Kumar, K. Sharma, H. Singh, S. G. Naugriya, S. S. Gill, and R. Buyya, “A drone-based networked system and methods for combating coronavirus disease (COVID-19) pandemic,” *Future Generation Computer Systems*, vol. 115, pp. 1–19, Feb. 2021, doi: 10.1016/J.FUTURE.2020.08.046.

[169] C. Conte *et al.*, “Performance analysis for human crowd monitoring to control COVID-19 disease by drone surveillance,” *2021 IEEE International Workshop on Metrology for AeroSpace, MetroAeroSpace 2021 - Proceedings*, pp. 31–36, Jun. 2021, doi: 10.1109/METROAEROSPACE51421.2021.9511671.

[170] “Perdix Fact Sheet.” https://dod.defense.gov/Portals/1/Documents/pubs/Perdix%20Fact%20Sheet.pdf?ver=2017-01-09-101520-643 (accessed Sep. 22, 2022).

[171] “Gremlins.” https://www.dynetics.com/_files/fact-sheets/pdf/K170437_Gremlins-Fact-Sheetv2.pdf (accessed Sep. 22, 2022).

[172] “BriteCloud DRFM (Digital RF Memory) countermeasure | Leonardo - Elettronica.” https://electronics.leonardo.com/it/products/britecloud-3 (accessed Sep. 22, 2022).

[173] “MALD Decoy | Raytheon Missiles & Defense.” https://www.raytheonmissilesanddefense.com/what-we-do/naval-warfare/advanced-strike-weapons/mald-decoy (accessed Sep. 22, 2022).

[174] “Air | DEFENDTEX.” https://www.defendtex.com/uav/ (accessed Sep. 22, 2022).

[175] C. Conte, S. V. Supplizi, G. de Alteriis, A. Mele, G. Rufino, and D. Accardo, “Using Drone Swarms as Countermeasure of Radar Detection,” *AIAA Science and Technology Forum and Exposition, AIAA SciTech Forum 2022*, 2022, doi: 10.2514/6.2022-0855.

[176] “Radar Evaluation Kits for various Front Ends - Silicon Radar GmbH.” https://siliconradar.com/evalkits/#sirad-easy (accessed Sep. 22, 2022).